INAUGURAL DISSERTATION

submitted to the

Combined Faculty of Natural Sciences and Mathematics

of the

Ruperto Carola University Heidelberg, Germany

for the degree of

Doctor of Natural Sciences

Presented by

M.Sc. **José Carlos dos Santos**

born in Jaguaquara-Bahia, Brazil

Date of oral examination: 20.12.2019

Development of inhibitors of the prostate specific membrane antigen (PSMA) for imaging and endoradiotherapy

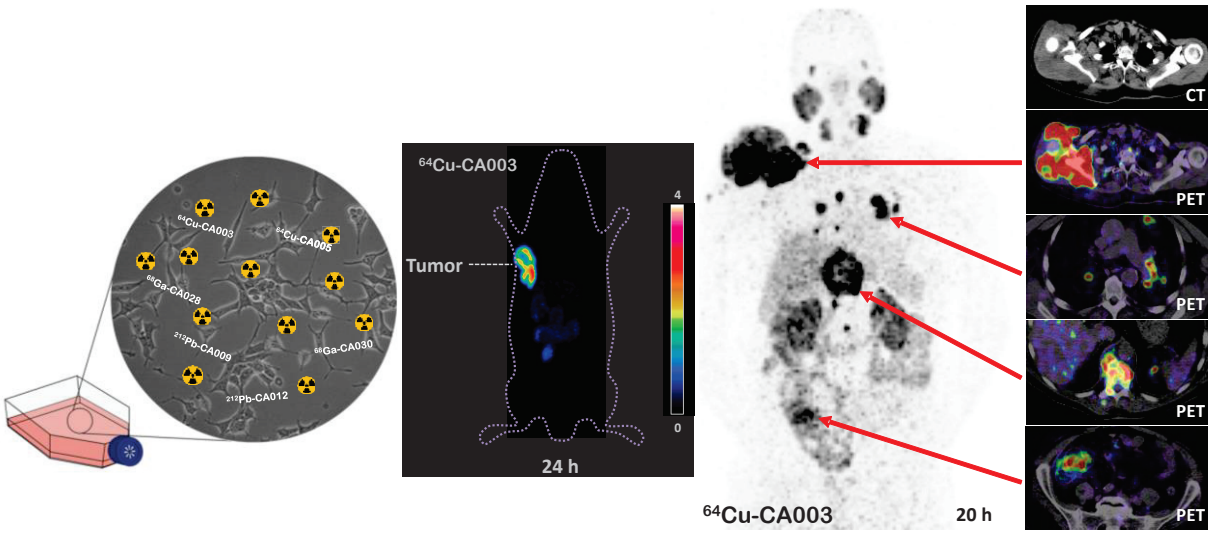

Referees:

Prof. Dr. Walter Mier

Prof. Dr. Gert Fricker

This dissertation is dedicated to Wolfgang Haunss, my German father… For his immense love that dwells in me…

Author: M. Sc. José Carlos dos Santos
Supervisor: Prof. Dr. Walter Mier
Institution: Heidelberg University/ Heidelberg University Hospital

Development of inhibitors of the prostate specific membrane antigen (PSMA) for imaging and endoradiotherapy

ABSTRACT

The prostate-specific membrane antigen (PSMA) has proven to be a promising target for diagnostic and therapeutic purposes. Although this biological target is well-recognized for prostate cancer, the expression of PSMA is not only restricted to prostate cancer. It is also expressed in many tumor types derived from the endothelial cells of tumor blood vessels. This thesis explores the development of inhibitors for specific targeting of PSMA. These inhibitors are small molecules that contain the Glu-NH-CO-NH-Lys moiety as binding motif, which was already shown to bind to PSMA with high affinity. The novel synthesized compounds were designed using PSMA-617 as reference. PSMA-617, bearing the linker moieties 2-naphthyl-L-alanine and 4-(aminomethyl) cyclohexanecarboxylic acid still the standard structure with respect to pharmacokinetics and internalization efficiency. Improvement of the linker moieties connected to alternative chelating agents to form stable complexes with copper radio-isotopes, in particular the theranostic pair ^{64}Cu and ^{67}Cu was one aim of the project. ^{64}Cu represents an alternative in case where short-term PET imaging is not possible and it also allows the dosimetry of therapeutic ^{67}Cu as an alternative to ^{177}Lu. In the second part of this thesis, PSMA ligands were developed for labelling with lead radio-isotopes; for this study, the radio-isotope ^{203}Pb was used as an imaging agent to obtain an approximation for the dosimetry with ^{212}Pb, a radionuclide that represents an *in vivo* alpha generator. In the last part of the project, a series of PSMA ligands that comprise a benzyl group in the chelator moiety was developed to further optimize the clinically established radiopharmaceutical PSMA-617. These compounds were evaluated *in vitro* in the PSMA expressing cell line, C4-2 and *in vivo* in tumor bearing mice. Among the compounds evaluated, CA003, CA012, CA028 and CA030 were the most promising ones, as demonstrated by their high PSMA-specific cellular uptake and low kidney uptake. The performance of the novel compounds was assessed in first patient studies resulting in clear visualization of the cancer and metastatic lesions with high contrast.

Keywords: prostate-specific membrane antigen (PSMA), prostate cancer, PSMA-inhibitors, PET imaging, endo-radiotherapy.

Autor: M.Sc. José Carlos dos Santos
Betreuer: Prof. Dr. Walter Mier
Institution: Universität Heidelberg/ Universitätsklinikum Heidelberg

Entwicklung von Inhibitoren des Prostata-spezifischen Membran-Antigens (PSMA) für die Bildgebung und Endoradiotherapie

ZUSAMMENFASSUNG

Das Prostata-spezifische Membran-Antigen (PSMA) hat sich als vielversprechendes Ziel für diagnostische und therapeutische Anwendungen gezeigt. Obwohl dieses biologische Zielmolekül bei Prostatakrebs gut erforscht ist, wird PSMA nicht allein von Prostatatumoren exprimiert. Es wird ebenfalls in mehreren Tumortypen der Endothelzellen der Tumorgefäße exprimiert. In dieser Dissertation wurde die Entwicklung von zielgerichteten Inhibitoren von PSMA untersucht. Diese Inhibitoren sind kleine Moleküle, die Glu-NH-CO-NH-Lys Einheit als Bindungsmotif haben, welches bereits eine hohe Bindungsaffinität an PSMA gezeigt hat. Für die neuentwickelten synthetisierten Verbindungen gilt PSMA-617 als Referenz. PSMA-617, welches die Linker 2-Naphthyl-L-Alanin und 4-(Aminomethyl)cyclohexancarbonsäure trägt, wird weiterhin als Standardreferenz im Hinblick auf Pharmakokinetik und zelluläre Aufnahme angesehen. Ein erstes Ziel dieser Arbeit war die Verbesserung der Linker Einheit, die an neue Chelatoren gekoppelt werden sollten, um einen stabilen Komplex mit Kupfer-Radioisotopen zu bilden, insbesondere mit dem theranostischen Paar ^{64}Cu und ^{67}Cu. ^{64}Cu kann als Alternative eingesetzt werden, falls PET-Bildgebung aufgrund von kurzer Halbwertszeit nicht möglich ist. Daneben ermöglicht es die Dosimetrie von therapeutischem ^{67}Cu als Alternative zu ^{177}Lu. Im zweiten Teil dieser Dissertation wurden PSMA-Liganden zur Markierung mit verschiedenen Blei-Radioisotopen entwickelt. In dieser Studie wurde das Radioisotop ^{203}Pb bildgebend prospektiv eingesetzt, um eine Annäherung an die Dosimetrie von ^{212}Pb zu erreichen, welches als *in vivo* Alpha Generator dient. Im letzten Teil des Projekts wurde eine Serie von PSMA Liganden zur Optimierung des klinisch etablierten Radiopharmazeutikums PSMA-617 entwickelt, die eine Benzyl-Gruppe in der Chelator Einheit enthalten. Diese neuentwickelten Liganden wurden *in vitro* in der PSMA-exprimierenden Zelllinie C4-2 getestet und *in vivo* im Maus-Modell. Von den untersuchten Verbindungen wurden CA003, CA012, CA028 und CA030 als die erfolgversprechendsten ausgewählt. Sie zeigten eine hohe PSMA-spezifische Anreicherung und eine niedrige Anreicherungsrate in der Niere. Diese Verbindungen wurden in ersten klinischen Studien getestet, und führten zu einer deutlichen Darstellung der Tumor-Läsionen mit hohem Kontrast.

Keywords: Prostata-spezifisches Membran-Antigen (PSMA), Prostatakrebs, PSMA-Inhibitoren, PET-Bildgebung, Endoradiotherapie

TABLE OF CONTENTS

LIST OF FIGURES

LIST OF TABLES

1. INTRODUCTION

1.1. Cancer

As the second leading cause of death worldwide, cancer has become a major medical challenge for current drug research in the modern world. It is reported that approximately 1 in 6 deaths are due to cancer, a total of 9.6 million deaths in 2018 alone *(1)*. Moreover, the cases of cancer are forecast to reach 22 million per year worldwide by 2032, which indicates a drastic increase of the incidence of cancer over the last 13 years *(2)*.

Cancer, which is also referred to as malignancy, malignant tumor or neoplasm, is a general term used for a large group of diseases with an uncontrolled cellular division, that can potentially proliferate to other organs by metastasizing, a process that is frequently responsible for the disease to become lethal *(3)*. The most frequently diagnosed forms of cancer are cancers of the lung, breast, colon, prostate, skin and stomach *(1)*.

Cancer cells are developed in a process in which healthy cells transform from a pre-cancerous lesion to a neoplasm, resulting in cancer. Either a genetic disposition or the impact of external influences, lead to these consecutive alterations which can generally be condensed into the three following subgroups: chemical carcinogens as for example constituents in cigarette smoke, the main group of mycotoxins: aflatoxin, the chemical element arsenic, asbestos; physical carcinogens, e.g. ultraviolet light (UV) and ionizing radiation and biological carcinogens. These biological carcinogens can be provoked by viral infections like Hepatitis, HIV and some forms of HPV or by parasites like helmiths or bacteria such as *Helicobacter pylori.* Ageing is besides these carcinogens another important factor for the development of cancer. The probability to develop of cancer rises dramatically with age. Presumably risks for specific cancers increase with age, due to non-repaired genetic damages among other factors *(3)*.

The Greek physician Hippocrates, the so-called “Father of Medicine” is credited with the origin of the word cancer. He coined the terms carcinos and carcinoma, which contain the Greek word for crab, most likely because cancerous tumors have similarities in their shape with a crab. Galen, another Greek physician, used “oncos” (meaning: swelling) to specify malignant tumors. Although the crab analogy is still used to describe neoplasm, Galen’s term is reflected in the expression oncology and oncologists, the doctor who specializes in cancer *(4)*.

1.2. Prostate cancer

Prostate cancer (PCa), also called adenocarcinoma, is the second most frequently diagnosed type of malignant tumors, followed by the malignant neoplasm of the skin *(5)*. The terminology adenocarcinoma stems from “adeno” which means, “relate to a gland” and carcinoma: “originated in the epithelial cell”.

An estimated 1,735,350 new cases of cancer were reported in the United States in the 2018, from this total, an estimated 164,690 (equivalent to 19%) were new cases of prostate cancer. For the year 2018 an estimated 9 percent of deaths among men were caused by prostate cancer *(5)*. That same year, prostate cancer was also the most commonly diagnosed cancer in European men, showing a high mortality *(6)*. Bray *et al, 2018* in global cancer statistics showed that prostate cancer comes second among the most common types of cancer and is worldwide the fifth leading cause of death among males. *(2)* (**Figure 1**).

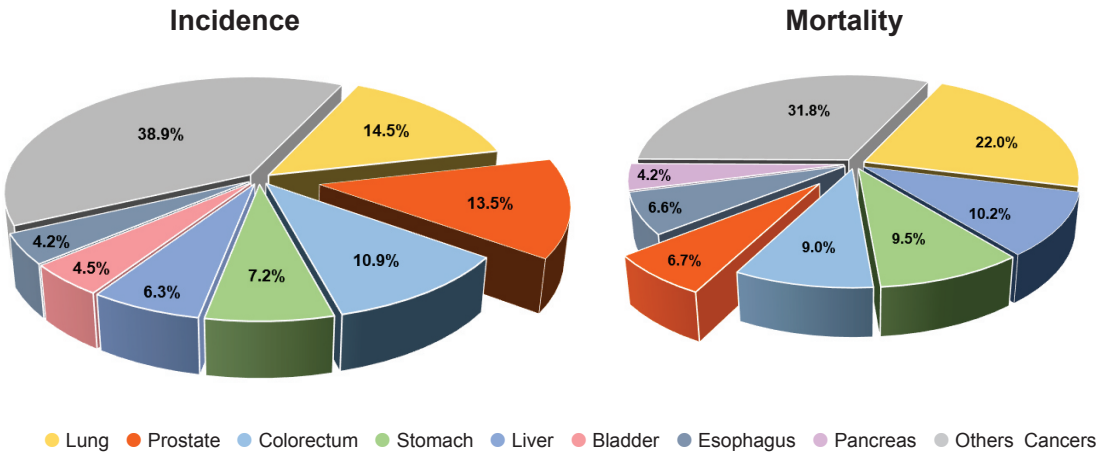

Figure 1: Incidence and death for the most common cancers in the world, for males in 2018. The highlighted part of the chart shows the proportion of the total number of incidence and mortality. Adapted from Bray, F., et al. Global cancer statistics 2018.

With respect to human anatomy, the prostate has a conical shape and the approximate size of a chestnut. In the male genital tract the prostate is a main gland, situated in the pelvic cavity under the urinary bladder in front of the rectum; thus an increase in the size of this organ can be detected by palpation *(7, 8)*. Additionally, the Skene´s paraurethral gland in females was reported to be similar to the male prostate gland, which is of clinical interest *(9)*. This gland was renamed as female prostate in 2002 *(10)*.

Immuno-histochemical studies show that this gland expresses the human protein 1. This evidence supports the existence of a gland in females analogous to the prostate of males *(11-13)*.

Though the causes of prostate cancer are still entirely unclear, many studies evidence the role of androgen hormones in prostate neoplasia. It is known that prostate tissue is androgen-dependent, and the malignancy of prostate cancer is also androgen-dependent *(14)*. There are many factors that play an important role as a risk factors for developing prostate cancer, such as: age (the risk rises beyond age 50), race (e.g. African-American are more vulnerable than white American men), chronic viral infections, exposure to cigarette smoke, hereditary prostate cancer (family history). The risk in American men is associated with genetic polymorphism in the enzymes that synthesize and metabolize androgenic hormones *(15)*. Furthermore, factors such as diet, environmental agents, occupation and lifestyle contribute to the development of this neoplasia *(16)*. A balanced diet with antioxidants, like beta-carotene vitamin E, vitamin C, and lycopene reduce the risk of prostate cancer *(17)*.

In the initial phase a prostate tumor usually does not cause any symptoms. In many cases, the prostate tumor development is not very fast; when the first symptoms appear, they are similar to benign prostatic hyperplasia (BPH) (**Figure 2**) *(18)*.

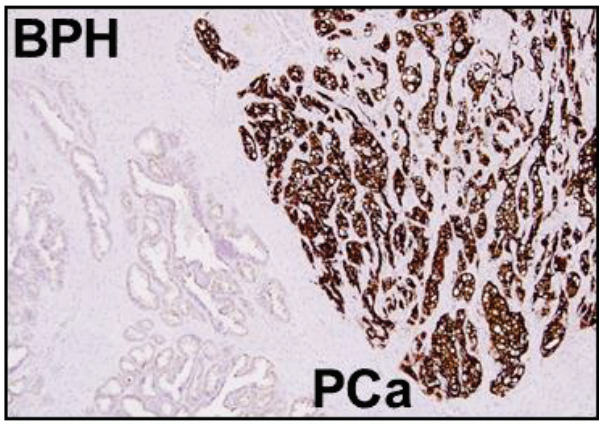

Figure 2: Immunohistochemical staining with anti-PSMA antibody showing the difference between prostatic hyperplasia (BPH) and prostate cancer tissue (PCa). Due to the high upregulation of PSMA expression, the screening reveals a strong staining in glandular epithelia of the neoplasm. Courtesy of Dr. Neil Bander, New York Presbyterian Hospital.

The benign prostate hyperplasia or benign hypertrophy is a non-cancerous condition characterized by enlargement of the prostate gland. The compression of the urethra by the tumor manifests in several symptoms, including increased urination, also in the night (nocturia), weak stream, no bladder control, hematuria, issues in urinary tract infections

and ejaculation *(19)*. Symptoms of BHP are manifested in 25% of men aged around 55 years. The treatment is recommendable only in severe cases. However, few cases of aggressive prostate tumor in younger men might occur and have been reported. This tumor can metastasize very quickly through the lymphatic system or bloodstream into the seminal vesicles, lymph nodes, lung and bone *(20)*.

Currently, there are three relevant methods for detecting prostate cancer in the early stages. The first and still the most common method used is for screening the prostate gland for neoplasm or hyperplasia is digital rectal examination (DRE). Other screening methods are prostate-specific antigen (PSA) and trans-rectal ultrasonography (TRUS). TRUS is a method that allows the creation of an image of the prostate gland by using sound waves *(21)*.

PSA is produced by the prostatic epithelial cells *(22)*. The level of PSA in serum is a sensitive marker used as a screening test for prostate cancer *(23)*. This biomarker can be used for monitoring tumor growth and response to therapy *(24-27)*. The level of PSA considered normal in serum is controversial. Previously, a PSA level of up to 4.0 ng/mL was considered normal, and any amount higher than this lead to a biopsy recommendation *(28)*. However, recent research shows patients with PSA levels below 4.0 ng/mL who have developed prostate cancer, as well as patients with higher levels of PSA who did not develop malignant tumors *(29)*.

In addition to other relevant methods for screening Prostate Cancer, MRI (magnetic resonance imaging) might help the diagnostic procedures and direct the guide-targeted biopsy to measure the aggressiveness of the tumor *(30, 31)*. The limitations and challenge of this method lead to the emergence of new diagnostic tools.

PET-CT (Positron emission tomography-computed tomography) is a tool that combines metabolic activity and morphologic examination. The use of this technique has significantly increased in recent years *(32-34)*.

^{18}F-FDG (Fludeoxyglucose-^{18}F) PET is the most commonly used tracer in radio oncology. This tracer is not suitable for PCa screening. Only aggressive and less-differentiated or undifferentiated neoplasms have a high affinity for FDG *(35, 36)*. Because of this limitation, choline derivatives such as ^{18}F-fluorocholine or ^{11}C-choline have become a better alternative as PET tracers for prostate cancer *(37)*. However, due to the limitations of these radiotracers, there is an urgent need for the development of new tracers that are target-specific. For this reason, the ^{68}Ga-PSMA-11 *(38)* was developed and has been highlighted in clinical use as one of the most promising

radiotracers for detecting PCa. In addition to specifically targeting PSMA, the theranostic agent PSMA-617 *(39)* and PSMA-I&T *(40)* were developed. The ^{18}F-labeled tracers most relevant to PSMA are ^{18}F-DCFBC *(41)*, ^{18}F-DCFPyL *(42)* and ^{18}F-PSMA-1007 *(43)*. By using radiopharmaceutical radiolabeled with short-lived isotopes ^{18}F and ^{68}Ga, successful molecular imaging was achieved. In this dissertation, this potential is exploit with long-lived isotopes such as ^{64}Cu, were used to enhance the use of PSMA-617.

To evaluate if the cancer cells migrated to other parts of the body, a histopathological examination of the biopsy pattern is essential. The TNM system is used for classification of the solid tumor, T stands for tumor and describes the size of primary tumor, N stands for lymph nodes and M for metastasis. This system is commonly used to determine the stage of PCa; and in consequence the treatment procedure. In the TNM system, five items are relevant: primary tumor extension, migration of the cancer cells to lymph nodes, metastasis, PSA level and the grade group, in combination with the Gleason score *(44)*.

1.3. Principal characteristics of PSMA

Prostate-Specific Membrane Antigen (PSMA) was first reported in 1998 by Gregorakis *et al.* as a new marker for prostate cancer *(45)* and was found in Lymph Node Carcinoma of the Prostate (LNCaP), a cell line derived from a supraclavicular lymph node from a 50-year-old caucasian man with hormone refractory prostate cancer *(46)*. This marker has been widely demonstrated as an excellent target for diagnostic and therapeutic applications in PCa. PSMA, also called glutamate carboxypeptidase II (GCPII) (EC 3.4.17.21), *N*-acetyl-*α*-linked acidic dipeptidase I [Naaladase (NLD) I] or folate hydrolase is a type II transmembrane glycoprotein with 750 amino acids and a weight of around 100 kDa *(47)*. This enzyme possesses a large extracellular part (44-750 amino acids) and a C-terminus with 2 zinc ions. The N-terminus is located in the intracellular domain *(48)*. The extracellular part of the enzyme is essential for its catalytic activity; this part is consists of apical (117-351 aa), protease (57-116 aa and 352-590 aa) and the C-terminal domain or the dimerization domain (591-750 aa) and allows the recognition of the substrate or ligand *(49, 50)*. The short N-terminus located in the cytoplasm is connected to membrane scaffold proteins, such as clathrin, clathrin adaptor protein 2, filamin A (FLNa) and caveolin-1 *(51-55)*. This part regulates the endocytosis of the GCPII-bound substrates GCPII-bound substrates.

PSMA or GCPII possesses similarities to transferrin receptor (Tfr), a considerable 54% homology with Tfr and 60% with Tfr2 *(56, 57)*. Transferrin and PSMA undergo clathrin-mediated endocytosis, but with the difference that, PSMA is characterized by a binuclear zinc site and an arginine patch in its catalytic center *(58)*.

To achieve a better understanding of the role of PSMA in carcinoma, a study of gene mapping was performed. It was demonstrated that PSMA gene is mapped to the short arm of the chromosome 11 *(59)*. PSMA is expressed in various tissues beyond the prostate in the kidneys *(60)*, liver *(61)*, salivary glands *(62)*, ovaries *(63)*, small intestine *(62)*, and central and peripheral nervous system *(64)*. For this reason, this enzyme received different names. Until now, the function of PSMA in PCa is not understood in great detail; however, it is demonstrated that the tumor progression is correlated with the level of expressed PSMA *(65)*. In prostate cancer cells PSMA is expressed 8 to 12 times higher than in healthy prostate cells. The expression of PSMA in prostate cancer is up to 10^6 PSMA molecules per cancer cell *(66)*. Studies show that an increase in PSMA expression is correlated to a higher Gleason score, which may legitimize the role of this biomarker in the aggressiveness or invasiveness of PCa *(60, 67)*. Another factor that plays a relevant role in the aggressiveness or invasiveness is the glycosylation profile of PSMA. This glycosylation has demonstrated large variation in different prostate cells lines *(49, 68)*.

PSMA is expressed in the brush border of proximal jejunum in the small intestine, and hydrolyses poly-γ-L-glutamylated folates and actively transports the mono-glutamylated folates into the blood stream (Figure 3) *(64, 67, 69, 70)*. PSMA metabolizes the neurotransmitter NAAG (N-acetyl-L-aspartyl-L-glutamate) in the brain, resulting in N-acetyl-L-aspartate and L-glutamate *(71, 72)* (Figure 3). In this context, PSMA/GCPII may be used as a target, not only for PCa, but for therapeutic and diagnostic purposes in neurological disorders as well.

The physiological function of PSMA in the other organs is still unclear und requires further investigation. However, it is reported that PSMA has a role in the metabolism of signaling molecules that are relevant for the function and architecture of the prostate gland *(73)*. Further investigation is still needed for the elucidation of these molecules and their function.

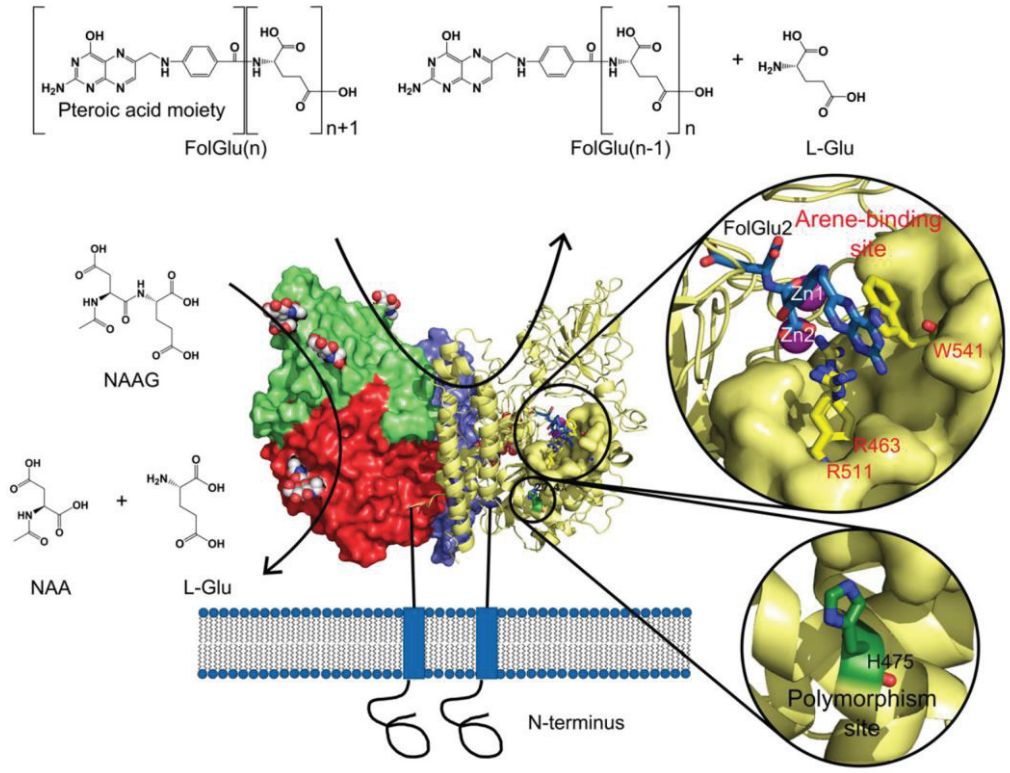

Figure 3: General view of glutamate carboxypeptidase II GCPII topology: active site (arene binding site) and natural substrates NAAG and folyl-poly-γ-L-glutamates (FolGlun) with their respective dissociation *(69)*. *Picture used with authorization of FEBS Journal order through Copyright Clearance Center's RightsLink® service number 4617120365361, order date on June 27, 2019.

Since in the last few years, PSMA expression has been reported, not only in PCa, but also in other neoplasms, such as kidney carcinoma, bladder, gastric and colorectal cancer, and the newly formed vessels of various solid tumors, the term PSMA, as "prostate-specific" must be reconsidered *(74-78)*.

1.4. PSMA targeting ligands

PSMA was first targeted with the monoclonal antibody (mAb) 7E11-C5 developed by Dr. Horoszewicz named ProstaScint® (Cytogen, Princeton, NJ) *(79)*. ProstaScint® is a radiolabeled monoclonal and also termed Indium (^{111}In) capromab pendetide. It has been approved by the FDA (Food Drug and Administration) since 1996. ProstaScint® is used as a prostate imaging agent to identify metastatic lesions of PCa *(80-83)*. 7E11-C5 is complexed with ^{111}In through the chelator and spacer arm CYT-356 *(83)*. Studies reveal that ProstaScint recognizes an intracellular epitope of PSMA *(84)*. *Ex vivo* experiments with subcutaneous LNCaP cell model revealed high tumoral uptake at a ratio of 3:1 in

comparison with muscle. This result led to progress in the clinical trials and approval by the FDA *(83)*. However, limitations of ^{111}In-capromab pendetide, though rare, include such adverse effects as *(85)* pooling of antibodies and decreased sensitivity of antibodies used in the scan because of cytoplasmic location of the epitope *(86)* requiring a highly qualified radiologist to be able to interpret ^{111}In-capromab pendetide scans. These limitations of SPECT imaging must be considered *(87)*.

In an attempt to overcome the limitations of ProstaScint®, the mAb J591 was developed, with the main feature of targeting the extracellular domain of PSMA, however, like the majority of full-length mAbs, this antibody showed a long residence time in the blood and thus a slow accumulation in tumors. This characteristic makes it favorable for diagnostic use, which requires prolonged imaging even days after injection *(88)*. Full length mAbs are not commonly used for radionuclide therapy because of their high haemato-toxicity *(89)*. Another selective inhibitor for PSMA is PMPA (2-(Phosphonomethyl)-pentandioic acid). However, limitations such as poor brain penetration warranted further optimization of PMPA.

The continuous improvement of diagnostics and therapy led to the use of small molecules *(43, 90-93)*, PSMA-targeted prodrugs *(94)* and nanoparticles *(95, 96)*, different generations of antibodies *(97-99)* or antibody fragments that have biological activity (minibodies) *(100)* and aptamer conjugates *(101)*.

1.5. Fundamental of nuclear medicine

1.5.1. Positron emission tomography

Positron emission tomography (PET) is a common tool used in nuclear medicine for functional molecular imaging of biological processes. It may be understood as a camera that is able to photograph specific objects in the span of a few seconds to several minutes. These cameras image high-energy gamma-rays resulting from the destruction of electrons by the positrons. Positrons are positively-charged electrons, also called anti-electrons, emitted from β^+ emitter's nuclei, which have a proton in excess. The positron collides with the nearest electron and they annihilate each other, producing high-energy gamma-rays (511keV) at an angle of approximately 180 degrees Figure 4 *(102, 103)*. The PET system possesses multiple detectors that captures the gamma rays, which are simultaneously registered and then reconstructed to produce images with high-

resolution. Bismuth germanate, lutetium, and lutetium-yttrium or gadolinium oxyorthosilicate (104) can be highlighted as among the most effective PET detectors.

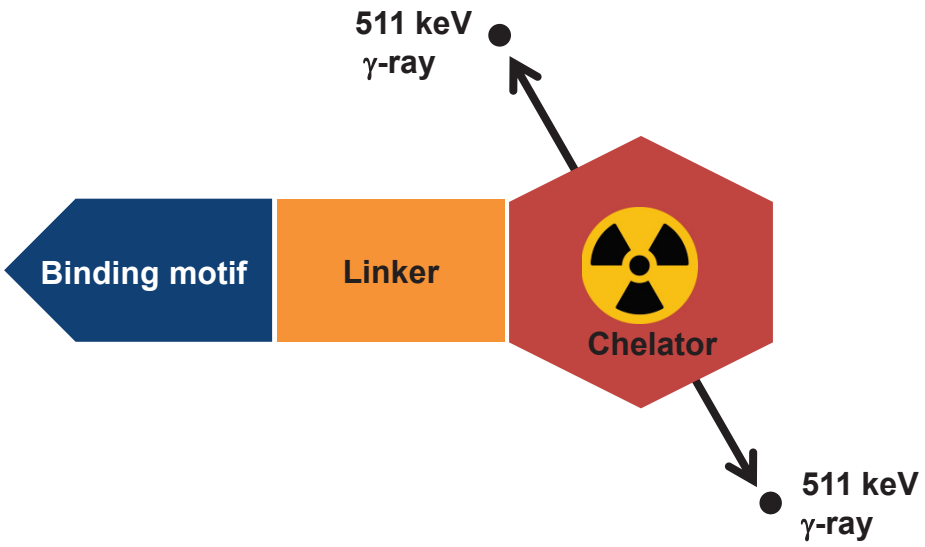

Figure 4: Principles of positron emission tomography (PET) based on the concept of targeted therapy. The positron annihilates with an electron and produces two gamma rays (511 keV) that are 180° apart, which can be detected by PET scanner.

The most common positron-emitting radionuclides used for PET imaging are ^{11}C, ^{18}F and ^{68}Ga. Most of the radionuclides used for PET have a relatively short half-life, meaning the radio synthesis must take place as quickly as possible. To overcome this problem, new radionuclides with longer half-life are necessary. In the last few years, the use of, ^{15}O, ^{13}N ^{62}Cu, ^{64}Cu, ^{124}I, ^{76}Br and ^{82}Rb, ^{89}Zr have shown great advantages *(103, 105-107)*. Most of them are produced in the cyclotron *(108)*, although some of them can be produced with a generator, such as ^{68}Ga and ^{82}Rb. Nowadays for PET imaging, the radiotracer 2-deoxy-2-(^{18}F)fluoro-D-glucose (FDG) is most frequently used, particularly in oncology, cardiology and neurology. FDG was introduced by Di Chiro and others in 1980s based on the hypothesis that the tumor consumes a higher rate of glucose. In fact, it was shown that the degree of malignancy of the cerebral neoplasm was correlated with the uptake of FDG *(109, 110)*.

Although PET scans are still costly, the use of this technique is rapidly increasing nowadays, particularly in oncology. PET imaging can be used in the early phase of the disease, as well as for treatment monitoring. In recent years, the use of small animal PET imaging in rodents and primates for has facilitated the development of new radiotracers for use in humans *(111)*. Furthermore, the combination of PET with computed tomography (CT), called PET/CT created a tool with the ability to localize functional abnormalities in addition to the anatomical information.

1.5.2. Single-photon emission computed tomography

Single-photon emission computed tomography (SPECT) is a tomographic imaging technique using gamma-emitting isotopes, which has the function of delineating physiological processes. The emitted radiation is, unlike in PET, directly measured *(112, 113)*. In order to produce images with high resolution, a common SPECT system must contain a gamma camera with at least one thallium-doped sodium iodide (NaI (Tl)), which revolves around the long axis of the patient´s body *(114)*. The quality of the image is also improved with an increase of detected gamma rays. Most gamma-rays are absorbed by the collimator; just the gamma-rays with the compatible angle and localization are detected *(115, 116)*. The radionuclides most frequently used for SPECT are ^{99m}Tc, ^{67}Ga, ^{111}In, ^{123}I and ^{201}Tl. It is noteworthy that these radionuclides possess a longer half-life than those used for PET. The majority of SPECT diagnostics, approximately 70%, are performed with ^{99m}Tc-radiolabelled compounds *(113)*. Due to its optimal half-life of 6.0 h and the emission of a single photon with an energy of 141 keV technetium-99m has become widely used. Moreover, the cost-effectiveness due to the availability of the ^{99m}Tc through the ^{99}Mo/^{99m}Tc generator system is what gives this specific radionuclide its great advantage *(117)*. However, the SPECT image has lower resolution and does not allow a blood flow estimation *(118, 119)*. SPECT is mostly used for myocardial, skeletal and brain imaging *(120-122)* and has recently gained emphasis in tumor imaging *(121, 123)*.

1.5.3. Endoradiotherapy

Radiation has different designations depending on how it is used in radiation therapy, such as: brachytherapy (sealed source radiation therapy), external beam radiation therapy (EBRT or XRT, tele-therapy) and systemic radioisotope therapy (RIT, endo-radiotherapy). The endo-radiotherapy is performed by using an internal radiation source for the treatment of numerous diseases, such cancer, among others *(124, 125)*. Since the end of the 19th century, it has become known that ionization radiation leads to cellular death. Studies revealed that radiation damages DNA in its structure and repair processes, causing DNA double strand breaks, which lead to apoptosis, necrosis, senescence and abnormal mitosis *(126-128)*.

Chemotherapy is the most commonly used method for tumor treatment in cases where the patient cannot undergo surgery or radiation therapy. This is due to the high availability of chemotherapeutic agents used for various neoplasms. In addition, the

requirements of hospital infrastructure are much lower in the use of chemotherapy. The use of chemotherapeutic agents requires good health conditions on the part of the patient because of the large amount of side effects it causes. In this context, the use of endo-radiotherapy presents several advantages; namely: it requires a very low amount of the targeting compound and produces fewer side effects. The “crossfire effect” might be considered; in this phenomenon, the emitted particles can interact with neighbouring cells, which is advantageous for treatment of neoplasm with heterogeneous receptors or for tumors with lower vascularization *(129)*. Another important phenomenon that provokes cellular death is the radiation-induced bystander effect. This phenomenon is based on the signal effect that irradiated cells transmit to their non-irradiated neighboring cells. The most relevant factors responsible for causing the radiation-induced bystander effect include expression changes of some genes involved in inflammation pathways, immune system factors, epigenetic factors and free radicals *(130, 131)*.

The choice of the radionuclide must be meticulous. Factors such as features of the emission of the radionuclide, its half-life, methods of production and biological/chemical characteristics should be taken into consideration. Of particular relevance is the decay mode of the radioisotope and the radiation range emitted that have to match the geometry, size and location of the tumor *(132)*.

Among the therapeutic radionuclides, beta emitters are widely used since they have a variety of ranges in tissues. In **Table 1** the radionuclides with a short range (less than 1,000 μm) are listed. In **Table 2** the medium range (1,000-2,000 μm) are shown, and the long range (tissue range greater than 2,000 μm) are in **Table 3**. The combination of beta minus and gamma emitters (β^-/γ) is not common; this combination is mostly used for therapy monitoring. The most commonly used beta emitter radionuclides in nuclear medicine are: ^{32}P, ^{153}Sm, ^{131}I, ^{90}Y and ^{177}Lu. Although ^{131}I is commonly used for therapy, it is a strong gamma emitter *(132-134)*.

Table 1: β^--emitting radionuclide for endoradiotherapy with short-range

Radionuclide	Half-life [d]	Energy β^-_{mean} [keV]	Production*	Purpose
^{47}Sc	3.4	162	R	oncology
^{67}Cu	2.6	141	C	oncology
^{105}Rh	1.5	152	R	bone disorders
^{131}I	8.0	182	R	thyroid disorders
^{161}Tb	6.9	154	R	bone disorders
^{169}Er	9.3	101	R	oncology
^{177}Lu	6.7	133	R	oncology
^{199}Au	3.1	82	R	oncology

* C = cyclotron, R = reactor

Table 2: β^--emitting radionuclides for endoradiotherapy with medium-range

Radionuclide	Half-life [d]	Energy β^-_{mean} [keV]	Production*	Purpose
^{77}As	1.6	228	R	oncology
^{109}Pd	0.5	361	C	oncology
^{111}Ag	7.5	360	R	synovectomy
^{149}Pm	2.2	364	R	oncology
^{153}Sm	1.9	229	R	oncology
^{159}Gd	0.8	311	R	bone disorders
^{186}Re	3.8	362	R	oncology
^{198}Au	2.7	315	C	oncology

* C = cyclotron, R = reactor

Table 3: β^--emitting radionuclides for endoradiotherapy with long-range

Radionuclide	Half-life [d]	Energy β^-_{mean} [keV]	Production*	Purpose
^{32}P	14	695	R	hematology
^{89}Sr	50.5	580	R	oncology
^{90}Y	2.7	935	R	oncology
^{142}Pr	0.8	809	R	oncology
^{165}Dy	0.1	451	R	bone disorders
^{166}Ho	1.1	666	R	oncology
^{188}Re	0.7	764	R	cardiology

*R = reactor

In recent years, the use of internally-targeted therapy with alpha emitters has rapidly increased. Due to favorable characteristics such as high linear energy transfer (LET) of circa 100 keV/µm and a short tissue range of 14-90 µm, accompanied by a high energy of 5-9 MeV, alpha therapy has demonstrated its ability to bring high amounts of energy to the targeted cells. This feature leads to a drastic increase in cytotoxicity. The effect on cell cycle arrest is stronger than with gamma-rays *(135)*. Furthermore, the high cell response that is linked to alpha therapy is independent of cell proliferation, oxygenation and dose rate *(136, 137)*. Recent studies showed that therapy with alpha emitters can overcome resistance to beta-emitters *(138)*. Reinforcing the relevance of alpha therapy, new studies releveled that alpha therapy induces immunogenic death *(139)*. It was demonstrated that alpha-therapy is a promising tool for treating metastatic cancer *(123, 140, 141)*.

The most commonly used radionuclides emitting alpha rays in nuclear medicine are: ^{225}Ac, ^{149}Tb, ^{227}Th, ^{211}At, ^{212}Bi, ^{213}Bi and as indirect alpha emitter ^{212}Pb (**Table 4**). The demand for alpha emitter-based radionuclide therapy with suitable half-life and characteristics for clinical use is still high.

Table 4: α-Emitting radionuclides suited for endoradiotherapy

Radionuclide	Half-life [d]	Energy α_{mean} [MeV]	Production*	Purpose
^{149}Tb	4.2 h	3.97	C	oncology
^{211}At	7.2 h	5.87	C	oncology
^{212}Bi	60.6 min	6.05	G	oncology
^{213}Bi	45.6 min	5.84	R	oncology
^{225}Ac	9.9 d	5.75	C	oncology
^{212}Pb	10.6 h	573.8 20#	G	oncology
^{223}Ra	11.4 d	5.78	G	oncology
^{227}Th	18.7 d	5.9	G	oncology

* C = cyclotron, R = reactor, G = generator, # = energy β^-_{mean} [keV]

In comparison with other currently used therapies, the endo-radiotherapy presents a significant advantage for the development of targeted therapy. The accumulation of the tracer in its target, can be monitored by SPECT and PET, which might significantly reduce the side effects.

1.5.4. Theranostics

Theranostic is understood as a linkage between diagnosis and therapy. The meaning of this word comes from the Greek *therapeuein,* "to treat medically," and gnosis, which signifies knowledge. The goal of using theranostics is to find the appropriate therapy for the correct patient at the right time *(142, 143)*. In recent years, personalized medicine is becoming increasingly common, which enables more effective treatment, especially in the field of oncology.

There are many peptide receptors that are expressed in various cancer subtypes, e.g., somatostatin receptor type 2, PSMA and CXC chemokine type 4 *(144, 145)*. The use of peptides as a theranostic vectors is due to the advantages that they present, such as ease of production, low immunogenicity, fast targeting and clearance. The first studies with theranostics using various radioisotopes of iodine for diagnosis and treatment of thyroid cancers showed how effective theranostics are *(146-150)*.

Further ligands were developed as theranostics, to the somatostatin receptor, for example, which is overexpressed on the surface of various neuroendocrine tumors *(151, 152)*. The somatostatin derivatives such as [DOTA^0,Tyr^3]-octreotide (DOTATOC) and [DOTA^0,Tyr^3]-octreotate (DOTATATE) should be highlighted. Both traces are pioneers for endoradiotherapy recently approved by FDA. The tracer DOTATATE is named Lutathera and DOTATOC SomaKit TOC *(153, 154)*. They can be radio-labelled with ^{68}Ga *(155, 156)* for imaging and with ^{90}Y or ^{177}Lu for therapy *(157, 158)*. A critical disadvantage of peptide-based radiotracers is their high kidney uptake; however, optimization of the design can overcome this limitation and improve the pharmacokinetics. One concrete example is the use of ^{86}Y-labelled DOTATOC/DOTATATE, which showed low renal uptake, consequently avoiding nephrotoxicity *(159, 160)*.

Recently, PSMA-617 by Benešová *et al.* has proven to be a suitable theranostic for prostate cancer. This theranostic radioligand showed a high tumor uptake, fast background clearance and kidney excretion. PSMA-617 may be radiolabeled with ^{68}Ga and ^{44}Sc for diagnosis (PET imaging) or with ^{90}Y and ^{177}Lu for endoradiotherapy, and additionally with ^{225}Ac or ^{213}Bi for alpha therapy *(39, 161-165)*.

1.6. Clinical relevant radionuclides

1.6.1. Gallium radioisotopes

Since the late 1940's, gallium radionuclide was used in nuclear medicine, at first, to study osteogenic activity and its phases. Further studies with ^{68}Ga and ^{67}Ga revealed the efficiency of these radioisotopes as tracers to identify tumors *(166)*.

The emission of radioisotopes is correlated with mass; radioisotopes with masses above 69 have a tendency to emit β^-, whereas radioisotopes with masses below 69 have a tendency to undergo β^+ decay. Gallium radioisotopes with masses below 69 decay into stable zinc isotopes, whereas radioisotopes with masses higher than 69 decay into germanium isotopes *(167, 168)*.

The most relevant gallium radioisotopes used in nuclear medicine are presented in **Table 5**. Among these, the radioisotopes ^{66}Ga, ^{67}Ga and in particular ^{68}Ga are the most commercially relevant. In the last few years, the use of agents labelled with ^{68}Ga ($t_{1/2}$ = 67.9 min, β^+ (89%)/ Electron Capture (EC) (11%)), for PET imaging have significantly increased as a good alternative to ^{18}F. However, the radioisotopes ^{66}Ga ($t_{1/2}$ = 9.49 h, β^+)

and ^{67}Ga ($t_{1/2}$ = 3.3 d, EC) have longer half-lives, which favors tumor-monitoring or detection of inflammatory disease *(168-171)*.

Table 5: Important radioisotopes of gallium

Isotope	Half-life	Decay mode(s)	Daughter isotope	application
^{66}Ga	9.5 h	β^+	^{66}Zn	PET
^{67}Ga	3.3 d	EC	^{67}Zn	SPECT
^{68}Ga	67.9 min	β^+(89%)/EC (11%)	^{68}Zn	PET
^{70}Ga	21.1 min	β^-(99.6%)/EC (0.4%)	^{70}Ge, ^{70}Zn	SPECT
^{72}Ga	14.1 h	β^-	^{72}Ge	SPECT

Gallium 67

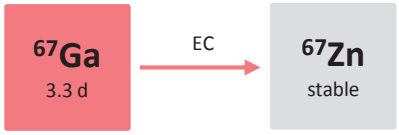

Figure 5: Decay schema of ^{67}Ga. Adapted from Karlsruhe Nuclide Chart.

The radionuclide ^{67}Ga has many characteristics which lend themselves to wide uses in nuclear medicine. ^{67}Ga is produced in an accelerator by proton irradiation of ^{67}Zn target or produced in a cyclotron obtainable in a carrier-free state. This radionuclide has a half-life of 3.26 d and decays via electron capture (EC) to stable radioisotope ^{67}Zn accompanied by the emission of four main gamma rays at 93 keV (38%), 184 keV (24%), 296 keV (16%) and 388 keV (7%) (**Figure 5**). These corresponding gamma emissions are detectable, not only with commercially available rectilinear scanners, but also with scintillation cameras *(166)*. This radionuclide is an efficient Auger β^- emitter which enables its use as a therapeutic radionuclide *(172)*.

Gallium 67 can be produced by irradiation of zinc targets with protons with an energy 20 MeV or with 23 MeV particle alpha in a cyclotron [^{64}Zn (α,p) ^{67}Ga, $^{67}Zn(p,n)^{67}Ga$ and $^{68}Zn(p,2n)^{67}Ga$)] *(173-175)*.

^{67}Ga can be complexed with citric acid to produce gallium citrate, also referred to as gallium scan, which can be used as SPECT imaging for diagnosis of inflammatory lesions or monitoring of neoplasms *(170, 176, 177)*.

Gallium 68

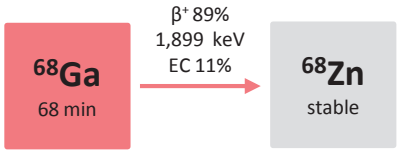

Figure 6: Decay schema of ^{68}Ga. Adapted from Karlsruhe Nuclide Chart.

Gallium-68 ($t_{1/2}$ = 68 min) emitts β^+ (89%) with a maximum energy of 1,899 keV suitable for PET. Additionally, it decays by EC (11%) to stable ^{68}Zn *(172)* and its decay by electron capture with concomitant γ-emission enables the use of ^{68}Ga for SPECT imaging **Figure 6**.

Currently, ^{68}Ga has been demonstrated to be an alternative to ^{18}F. Among other arguments the ease of production is a relevant point. Gallium-68 can be produced by a ^{68}Ge/^{68}Ga generator or by a cyclotron *(178-181)*. The generator-based ^{68}Ga has ^{68}Ge ($t_{1/2}$ = 271 d and 100% EC decay) as a parent isotope. ^{68}Ge is produced by the accelerator from the target Ga_2O_3 through the reaction ^{69}Ga (p,2n) ^{68}Ge *(182, 183)*. Furthermore, ^{68}Ga can also be obtained from a cyclotron by a ^{68}Zn (p,n)^{68}Ga reaction *(180)*.

The development of ^{68}Ga-PET imaging in the last years is a positive indicator that will allow the use of new ligands to target molecules in the clinical practice. The quality of PET imaging is obviously much higher than SPECT. The ^{68}Ge/^{68}Ga is a long term generator which can be used for a period of more than twelve months, which is advantageous. In addition, an on-site cyclotron is not necessary *(184-186)*.

The energy emitted by ^{68}Ga (maximum energy of 1.9 MeV) is higher than ^{18}F (maximum energy of 0.63 MeV); however, the spatial resolution obtained by ^{68}Ga is lower than ^{18}F *(187)*, though a scanner detector with a resolution of 3 mm showed a high quality of images for both radionuclides *(188)*.

The cation $^{68}Ga^{3+}$ can be complexed with ligands that contain oxygen and nitrogen as a donor, which allows the development of a kit *(189)*. Many radiotracers labelled with ^{68}Ga were published in the last year and show that this radionuclide is very relevant for PET

imaging of many tumors and their respective metastases. Among all ^{68}Ga-based radiotracers, ^{68}Ga-DOTA-TATE that contains tyrosine^{3}-octreotate and the agent chelator DOTA (1,4,7,10-tetraazacyclododecane-1,4,7,10-tetraacetic acid), approved by the US Food and Drug Administration (FDA), should be highlighted *(190)*. In addition, DOTATOC and DOTANOC analogous to DOTATATE are also labeled with ^{68}Ga and can bind to somatostatin receptors with high affinity; their potential was assessed to be effective in patients with neuroendocrine tumor *(191, 192)*.

1.6.2. Scandium radioisotopes

The radionuclide ^{44}Sc was proposed in 2010 as an alternative to gallium 68 for PET imaging in nuclear medicine *(193, 194)*.

Many radiotracers labelled with scandium radioisotopes produced from ^{44}Ti/^{44}Sc *(195-197)* generator, neutron irradiated Ti *(198, 199)*, and cyclotron produced ^{44m}Sc/^{44}Sc *(200, 201)*, ^{nat}Sc *(202)*, ^{46}Sc *(203)*, and ^{47}Sc *(204-207)* were published in the last year and demonstrate the relevance of radionuclide for PET imaging of metastatic tumors and as a radiopharmaceutical.

Some of the most common scandium radioisotopes are given in **Table 6**. As showed in this table calcium isotopes are the primary decay products of radioisotopes with atomic weights below 45, whereas for radioisotopes with weights higher than 45, the primary decay products are titanium isotopes *(168)*. The theranostic pair ^{44}Sc/^{47}Sc can be used as an alternative to ^{68}Ga/^{177}Lu, which are not very useful, because of differing chemistry and consequently different biodistribution data. Recent studies showed that the theranostic pair ^{44}Sc/^{47}Sc is much better than ^{68}Ga/^{177}Lu *(165)*. Scandium radionuclides can be easily complexed with the chelator DOTA. The stability constant of the scandium-DOTA complex is higher compared to ^{68}Ga or ^{177}Lu *(208)*.

Table 6: Important scandium radioisotopes

Isotope	Half-life	Decay mode(s)	Daughter isotope	application
^{43}Sc	3.9 h	β^+	^{43}Ca	PET
^{44}Sc	4.0 d	β^+	^{44}Ca	PET
^{47}Sc	3.3 d	β^-	^{47}Ti	SPECT
^{48}Sc	43.7 h	β^-	^{48}Ti	SPECT
^{49}Sc	57.2 h	β^-	^{49}Ti	SPECT

Scandium-44

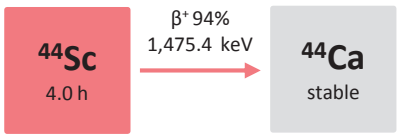

Figure 7: Decay schema of ^{44}Sc. Adapted from Karlsruhe Nuclide Chart.

Due to its particular characteristics, such as its decay by β^+ emission ($E_{max,\ \beta+}$ = 1,475.4 keV, intensity 94.3%) to the stable isotope ^{44}Ca ($t_{1/2}$ = 3.97 h) **Figure 7**, the radioisotope ^{44}Sc is highly attractive for clinical PET imaging *(168)*.

^{44}Sc can be produced from a ^{44}Ti/^{44}Sc generator. The half-life of the parent radionuclide ^{44}Ti is 60.4 years *(197)*. ^{44}Ti is produced by a ^{45}Sc (p,2n)^{44}Ti reaction *(209)*.

The half-life of 4 days enables a transport of ^{44}Sc-labelled radiopharmaceutical to hospitals that are quite far away from the production site. However, the quite high gamma emission must be taken into consideration.

Due to its favorable half-life^{44}Sc can be used as an alternative to ^{18}F and ^{68}Ga, which is of great interest for tumor monitoring *(195)*.

Scandium-47

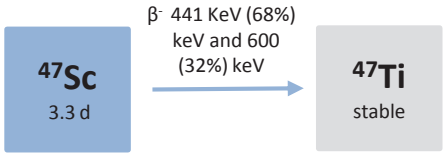

Figure 8: Decay schema of ^{47}Sc. Adapted from Karlsruhe Nuclide Chart.

As an alternative to ^{177}Lu ($t_{1/2}$ =6.65 d and E_{max,β^-} = 497 keV, intensity 94.3%) ^{47}Sc can be used which also emits the β^- ($t_{1/2}$ = 3.35 d) with 441 keV (68% intensity) and 600 keV (32% intensity) *(203)* **Figure 8**. Due to its unique characteristics, ^{47}Sc has been proposed for use in therapy. Like ^{99m}Tc, it possesses gamma emission ideal for SPECT *(205)*. Due to chemical similarities to ^{90}Y, radiopharmaceuticals developed to complex ^{90}Y can be also complexed with ^{47}Sc.

The production and application of ^{47}Sc is still not as extensively investigated as that of ^{44}Sc. ^{47}Sc can be produced by a nuclear reactor with high neutron irradiation (En $>$ 1 MeV). The reaction ^{46}Ca (n,γ) ^{47}Ca $\rightarrow$ ^{47}Sc is performed to produce ^{47}Sc with a high degree of purity, which is an advantage over the production via the route ^{47}Ti, which leads to poor quantities and impurities of the product *(210)*. In addition, the ^{47}Sc can also be produced from a photonuclear reaction ^{48}Ti (γ,p) ^{47}Sc *(211)*.

1.6.3. Lutetium-177

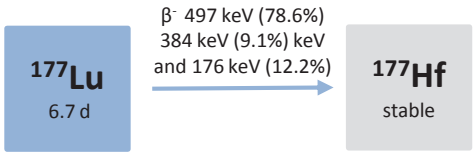

Figure 9: Decay schema of ^{177}Lu. Adapted from Karlsruhe Nuclide Chart.

Among all radioisotopes of lutetium, ^{177}Lu ($t_{1/2}$ = 6.7 days) is the most relevant in therapeutic applications. ^{177}Lu is a short-range beta emitter with E_{max} of 497 keV (78%), 384 keV (9.1%) and 176 keV (12.2%), which makes it promising for targeted radiotherapy (**Figure 9**) ^{177}Lu is also an emitter of γ photons of 113 keV (6.4%) and 208 keV (11%); therefore, it can be used for imaging with gamma scintigraphy cameras *(212)*.

Because of its long half-life of 6,7 days, ^{177}Lu can be used to label antibodies and is also well-suited for transport to hospitals that are distant from the nuclear reactor *(88, 213, 214)*.

DOTA and DTPA (diethylene-triamine-pentaacetic acid) form stable complex with Lutetium-177. A series of radiopharmaceuticals labelled with ^{177}Lu was evaluated over the course the last years *(215-217)*.

By neutron bombardment with high flux reactors and isotopically enriched ^{176}Lu (71%) Lutetium-177 can be obtained. Specific activities of circa 740 GBq mg^{-1} can be gained *(218)*. However, Lebedev *et al.*, 2000 showed that the production of 177-Lutetium with no-carrier-added is possible *(219)*. This production occurs according to the reaction ^{176}Yb (n,γ)^{177}Yb. The product ytterbium-177 decays by β^- emission to ^{177}Lu.

1.6.4. Copper radioisotopes

Copper plays an important role in many biological processes such as structural shaping, electron transfer and catalysis *(220)*. In order to take advantage of the chemical and biological features of copper, the application of copper radioisotopes has significantly risen in nuclear medicine in recent years *(221-223)*. Among them, ^{60}Cu, ^{61}Cu, ^{62}Cu and ^{64}Cu can be highlighted for diagnostic purposes and ^{67}Cu for therapeutic purposes. The most significant copper radioisotopes in nuclear medicine are listed in **Table 7**.

Table 7: Important copper radioisotopes

Isotope	Half-life	Decay mode(s)	Daughter isotope	application
^{60}Cu	23.7 min	β^+ (92.6%), EC (7.4 %)	^{60}Ni	PET
^{61}Cu	3.3 h	β^+ (61.4%), EC (38.6 %)	^{61}Ni	PET
^{62}Cu	9.7 min	β^+ (98 %), EC (2 %)	^{62}Ni	PET
^{64}Cu	12.7 h	β^+ (18 %), EC (44 %),β^- (38%), γ (0.5%)	^{64}Ni/^{64}Zn	PET
^{67}Cu	61.8 h	β^-	^{67}Zn	SPECT

Copper radioisotopes undergo β^+ decay in particular radioisotopes with masses below 63, while radioisotopes with masses above 65 decay typically by β^-. Because of its versatility, copper-64 is one of the most used isotope; it decays by β^+, EC and β^-. The theranostic pair ^{64}Cu/^{67}Cu was successfully evaluated *(224, 225)*.

The choice of the chelator for labelling the peptide or antibody is challenging because of the low stability of copper radiolabeled compounds. Loss of copper from the chelator *in vivo* may occur *(226)*.

Cu can be released from the chelator *in vivo* by different mechanisms. Enzymes can reduce copper (II) to copper (I); consequently, the ligands undergo de-metallation and metabolic degradation *(227)*.

The chelator 1,4,8,11-tetraazacyclotetradecane-N,N',N'',N'''-tetraacetic acid (TETA) was developed in order to complex copper radioisotopes with peptides or antibodies *(33, 228)*. Based upon TETA the ethylene “crossbridge” cyclam derivative (CB-2ETA) was developed as an alternative and was shown to complex copper radioisotopes with high kinetic stability and was less susceptible to trans-chelation *in vivo (229, 230)*.

Copper-64

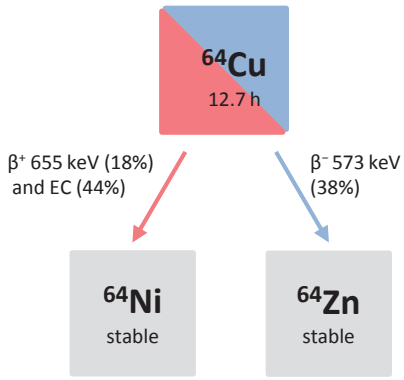

Figure 10: Decay schema of ^{64}Cu. Adapted from Karlsruhe Nuclide Chart.

Because of its unique characteristics, ^{64}Cu is the most versatile copper radioisotope. This radionuclide with a half-life of 12.7 hours combines β^+ (18%) emission (E_{max} = 655 keV) to ^{64}Ni, β^- (38%) and β^- emission (E_{max} = 573 keV), to ^{64}Zn. Through electron capture (EC) (44%) combined with auger electrons emission ,0.5% γ radiation/internal conversion (IC), ^{64}Cu decays to ^{64}Ni **Figure 10**.

Because of its half-life of 12.7 hours, which is comparable for the *in vivo* kinetics of a series of molecules, such as small molecules or antibodies, ^{64}Cu is appropriate for use in radiopharmaceutical synthesis. Thus, these characteristics make ^{64}Cu appropriate for PET imaging and for therapeutic purposes. The theranostic pair ^{64}Cu/^{67}Cu can be successfully used once PET imaging is used as part of the quantitatively-planned targeted radiotherapy and enable an effective evaluation of the radiation dosimetry *(231, 232)*.

Traditionally, ^{64}Cu has been produced by a nuclear reactor as carrier-added neutron activation through the reaction ^{63}Cu(n,γ) ^{64}Cu or under no-carrier-added conditions with fast neutrons via reaction ^{64}Zn(p,n)^{64}Cu. An alternative to this approach is a biochemical cyclotron by irradiation of such nickel or zinc targets as the ^{64}Ni(p,n)^{64}Cu, which use charged protons *(233, 234)*.

Copper-67

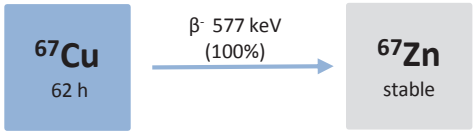

Figure 11: Decay schema of ^{67}Cu. Adapted from Karlsruhe Nuclide Chart.

^{67}Cu ($t_{1/2}$ = 62 h) is the longest-lived radionuclide of copper. This radionuclide is characterized by 100% β^- emission (E_{max} = 577 keV) to ^{67}Zn and by one of its three metastable radio-isomers **Figure 11**. Because of the transitions of the metastable radioisomers resulting in gamma rays with energies of 185 keV (48%), 93 keV (16%), 91 keV (7%), ^{67}Cu is appropriate for SPECT imaging *(235)*. The moderately long half-life, the complete β^- emission, and manageable and easy radiolabelling, make ^{67}Cu ideal as a ligand with molecular carriers such as peptides or antibodies *(223, 236)*. However, its use is limited due to the fact that its production involves a high-energy accelerator.

In comparison with ^{177}Lu, ^{67}Cu has a more suitable half-life that favors optimized repeated dosing for the patients, only a few days of hospitalization and reduced costs of waste management.

Through the reaction in the nuclear reactor ^{67}Zn(n,p)^{67}Cu, copper-67 can be obtained in quantities relevant for the nuclear medicine application *(237)*. ^{67}Cu can also be produced in a proton accelerator via the reaction ^{64}Ni(α,p)^{67}Cu *(238)*.

1.7. Target Alpha Therapy

The search for new alpha-emitter radionuclides has intensified in the last year. The use of alpha-emitter radionuclides combined with the targeted therapy approach has been shown to be a promising tool for the treatment of cancer. This development can be highlighted by the approval of radium-223 (^{223}Ra) dichloride (Xofigo®) by the FDA as a radiopharmaceutical for the treatment of bone metastasized prostate cancer. Xofigo® was the first α-emitter to be approved by the FDA *(239)*.

The increased interest in alpha radionuclides is due to high cytotoxicity resulting from their high linear energy transfer (LET) and short path length, which is approximately 50 - 100 μm. In contrast to alpha emitters, beta emitters have long ranges, which lead to radiation exposure of physiological tissue. Additionally, the low–LETof beta emitter can be inefficient in killing tumor cells. **Figure 12** shows the difference between alpha and beta particles.

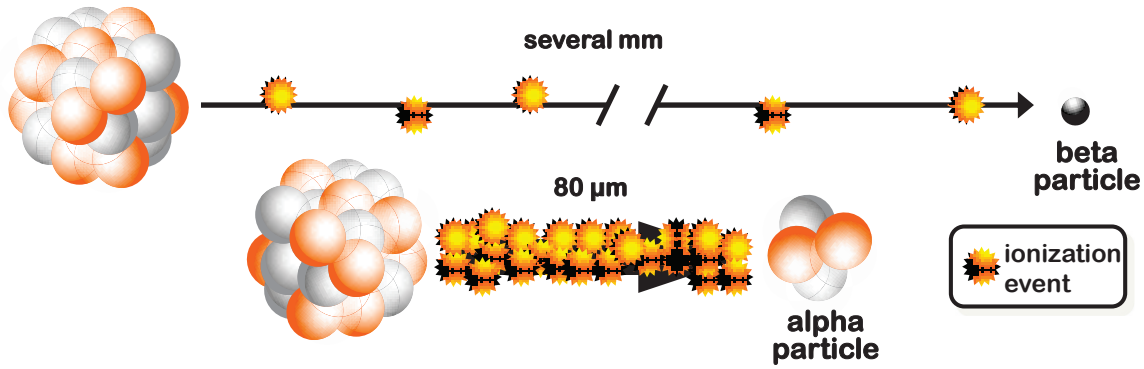

Figure 12: Path length and ionization of alpha- and beta-emitters.

It has been proven that one single decay event of an alpha emitter can kill a single cancer cell (240, 241). This emitted α particle ionizes the nucleus of cells, which breaks the DNA double-strand, ultimately causing cell death. Cell death is a result of the high relative biological effectiveness (RBE) of the alpha particle (242). It is reported that α-particles can overcome resistances provoked by β emitters (138). Furthermore, alpha radiation can induce immunogenic cell death of the cancer cell. This approach strengthened the interest in alpha radiation in nuclear medicine (139). This phenomenon, the so-called abscopal effect (**Figure 13**), can be activated by the death of malignant tumor cells by ^{212}Pb irradiation of C4-2, a subline of the PSMA-positive cell line LNCaP

(human lymph node carcinoma of the prostate), animal tumor model. The dead cells release danger-associated molecular proteins (DAMPs) e.g. heat shock protein 70 (HSP70) and high mobility group box 1 (HMGB1) leading to an activation of dendritic cells (DCs). The activated DCs are responsible for expressing costimulatory agents, such as cluster of differentiation 40 (CD40) and cluster of differentiation 86 (CD86) which activate the cytotoxic T- cells which are specific to the tumor antigens. These T- cells are spread through the body and are able to eliminate small clusters of tumor cells at distant parts of the body *(243, 244)*.

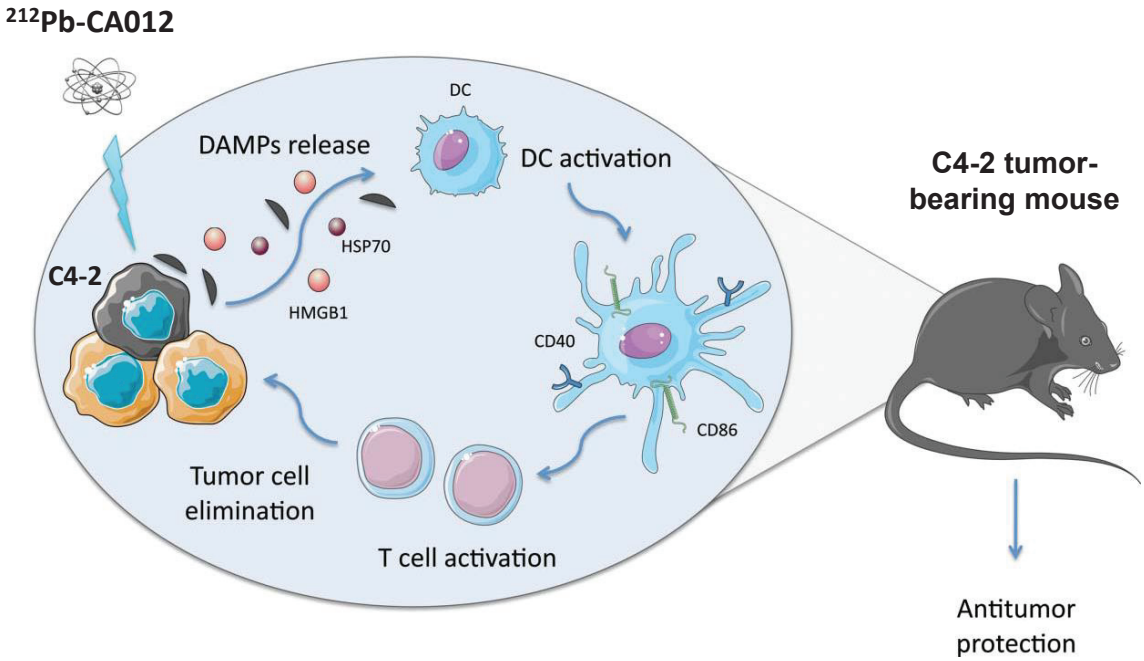

Figure 13: Schematic illustration of ^{212}Pb-CA012 *in vivo* simulation by using ^{212}Pb as an inductor of immunogenic cell death. Adapted from Gorin, J. B., *et al*. 2014 (132). Figure modified with permission of Dr. Joëlle Gaschet, Institut de Recherche en Santé de l'Université de Nantes, France.

Among the alpha-emitting radionuclides, actininum-225 (^{225}Ac), bismuth-213 (^{213}Bi), and more recently, lead-212 (^{212}Pb) and astatine-211 (^{211}At) are the most relevant in nuclear medicine today.

Actinium-225

Figure 14: Decay schema of ^{225}Ac. Adapted from Karlsruhe Nuclide Chart.

One big challenge in the advancement of using the alpha emitter ^{225}Ac is the availability of this radionuclide. The Nuclear Science Advisory Committee (NSACI) identified ^{225}Ac as a top research priority in 2008 and also in 2015 *(245)*. In 2011 the International Atomic Energy Association (IAEA) gave high priority to the accelerator production of ^{225}Ac *(246)*.

Actinium 225 ($t_{1/2}$ = 10 d) decays by alpha emission via ^{221}Fr ($t_{1/2}$ = 4.8 min, ^{217}At ($t_{1/2}$ = 32.3 ms) and ^{213}Bi ($t_{1/2}$ = 47 min) (**Figure 14**). All three daughter radionuclides are alpha emitters. ^{225}Ac can be gained from the natural decay of ^{233}U or from accelerator-based methods *(247-249)*.

It has been proven that therapeutics containing ^{225}Ac targeted ligands are approximately 1000 times more potent than ^{213}Bi-targeted therapy *(250)*. In spite of ^{225}Ac being more potent than other alpha emitters, the problem of free daughter radioisotopes circulating in the blood after its decay has not been solved. Also, the question of the ability of chelation chemistry to sequester the free radionuclide has still not been answered *(251, 252)*.

To exploit the therapeutic potential of actinium-225, ^{225}Ac-Lintuzumab was developed for the treatment of Acute Myeloid Leukemia (AML) *(253)* and ^{225}Ac-PSMA-617 for the treatment of prostate cancer *(163, 254)*. In both radiopharmaceuticals, DOTA is used as a chelator to complex ^{225}Ac and forms a stable complex *in vivo*. The stability of the with

^{225}Ac complexed chelators: HEHA(1,4,7,10,13,16- hexaazacyclohexadecane-*N*,*N*,*N*′,*N*″,*N*‴,*N*⁗ hexaacetic acid), c-DOTA and PEPA(1,4,7,10,13-pentaazacyclopentadecane-*N*,*N*′,*N*″,*N*‴,*N*⁗ pentaacetic acid) was assessed *in vivo* and among these the ^{225}Ac-HEHA showed the highest stability *(251)*.

Bismuth-213

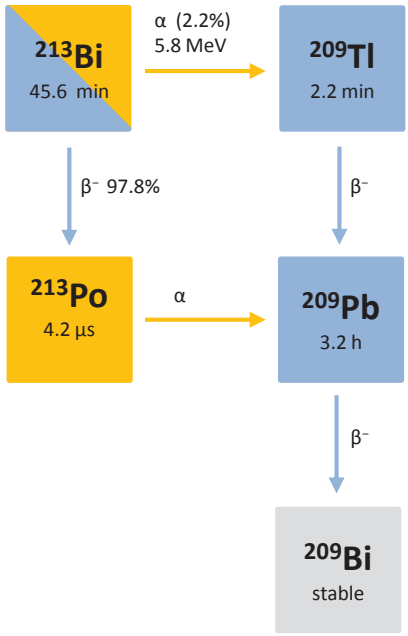

Figure 15: Decay schema of ^{213}Bi. Adapted from Karlsruhe Nuclide Chart

^{213}Bi ($t_{1/2}$ = 45.6 min) decays to ^{209}Tl ($t_{½}$ = 2.2 min, α 2%) and via ^{213}Po ($t_{½}$ = 4.2 µs, β 97.8%) to stable ^{209}Bi (**Figure 15**). Bismuth-213 is available from a generator which resembles ^{225}Ac. This generator contains a cation-exchange resin. This resin is used to avoid charring and decomposition of the resin caused by confined radiation flux *(255, 256)*.

With 440 keV photon emission, ^{213}Bi can be used to study in biodistribution and pharmacokinetic and dosimetry studies *(164, 257, 258)*. Right after the elution from the ^{225}Ac generator, ^{213}Bi can be used for labeling small molecules e.g. peptides and antibodies or vectors with an appropriate bifunctional chelator effectively complexing ^{213}Bi. Bifunctional chelators such as CHX-DTPA or DOTA are suitable as stable complex for ^{213}Bi *in vivo (241, 257).*

In *in vitro* experiments previously showed that ^{213}Bi, as an alpha emitter, can overcome resistance caused by beta emitters *(259)*. In addition, studies in patients with neuroendocrine tumors demonstrated that ^{213}Bi-DOTATOC can overcome resistances to the ^{90}Y/^{177}Lu-DOTATOC beta emitter *(138, 260)*.

Lead-212

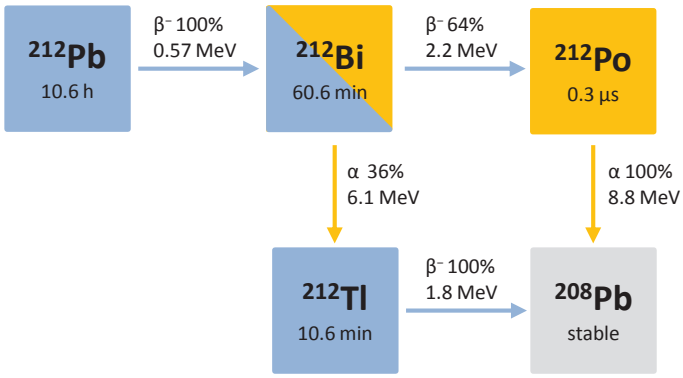

Figure 16: Decay schema of ^{212}Pb. Adapted from Karlsruhe Nuclide Chart

^{212}Pb ($t_{1/2}$ = 10.64 min) can be used as alternative to ordinary-emitting alpha radionuclides, because it lacks their shortcomings. Most α-emitting radionuclides possess half-lives which are either too short or too long; furthermore, chemical incompatibility in attaching the radio-nucleotides to the target molecules hindered their production and the low availability are great concern *(261)*. Because of its half-life, ^{212}Pb can be exploited for the development of new alpha-targeted radiopharmaceuticals. Lead-212 is an important part of the ^{228}Th decay chain. It decays by β^- emission to ^{212}Bi, a potent alpha emitter. The decay to ^{212}Bi illustrates an indirect way to gain ^{212}Bi ($t_{1/2}$ = 60.6 min), and the problem to handle a radionuclide with a short half-life can be overcome. The use of ^{212}Pb is a strategy of producing an *in vivo* generator of ^{212}Bi (**Figure 16**). This approach enables the use of ten times the dose per administered activity than if just ^{212}Bi were used. Additionally, small amounts of ^{212}Pb are needed in comparison with ^{212}Bi *(262)*.

Bifunctional chelators e.g. TCMC (2-(4-isothiocyanotobenzyl)-1, 4, 7, 10-tetraaza-1, 4, 7, 10-tetra-(2-carbamonyl methyl)-cyclododecane) or DOTA efficiently complex 212-Pb. However, studies reveal that DOTA is not stable with ^{212}Pb because 36% of ^{212}Bi is released from the chelator as consequence of the decays *(263)*, whereas experiments showed that the TCMC chelator formed a highly stable complex with ^{212}Pb *(264, 265)*.

The use of ^{212}Pb has been demonstrated to be efficient in radio-immuno-conjugates *(266, 267)* and small molecules *(123)*.

1.8. Purpose of the study

The prostate-specific membrane antigen (PSMA) has proven to be a promising target for diagnostic and therapeutic purposes. The expression of PSMA is not only restricted to the prostate gland but is also expressed in kidney, liver, salivary and lacrimal glands, mammary glands, and in many tumor types by the endothelial cells of tumor vessels *(74-78)*. Although the expression of PSMA in the above tissues is lower than in prostate tissue, studies revealed that these tumor types are extensively characterized with regard to PSMA. Even in the face of the progress achieved in diagnostics and the development of the ability of new radiopharmaceuticals to detect metastatic tumors, improvement is still urgent. Using small molecules for specific targeting is an import strategy; which offers many advantages, such as fast biomarker-specific binding, enhancing the staging of primary tumors and recurrence (hormone-refractory) followed by endo-radiotherapy with fewer side effects. It was shown that Glu-NH-CO-NH-Lys has a high affinity for binding to PSMA. PSMA-11 and PSMA-617 possess this binding motif and have proven to be highly effective for diagnostic and endo-radiotherapeutic purposes, respectively *(268, 269)*. PSMA-11 was developed by Eder *et al*, 2011 and PSMA-617 by Benešová *et al,* 2015; both studies were conducted in the Division of Radiopharmaceutical Chemistry at the DKFZ in collaboration with the Department of Nuclear Medicine of the University Hospital of Heidelberg. By using the ^{68}Ga-PSMA-11 containing the lipophilic chelator HBED-CC, imaging with high specificity and sensitivity of metastatic or recurrent prostate cancer was achieved. It was proven that PSMA-11 showed high specificity and sensitivity compared to ^{18}F-choline, which is used as the standard to detect PCa lesion *(270)*. PSMA-11 can be labelled with ^{68}Ga; however, it failed to form a stable chelate complex with most common radionuclides such as ^{90}Y, ^{177}Lu, ^{213}Bi and ^{225}Ac. In contrast, the theranostic agent PSMA-617 contains the chelator DOTA, that is routinely chosen if labeling with both diagnostic (e.g. ^{44}Sc, $^{67/68}$Ga, ^{111}In) and therapeutic radionuclides (e.g. ^{90}Y, ^{177}Lu) is intended *(271)*. Nevertheless, PSMA-617, bearing the linker moieties 2-naphthyl-L-alanine and 4-(aminomethyl)cyclohexanecarboxylic acid, is still the standard reference regarding pharmacokinetics and internalization *(39, 272)*. However, none of these ligands, neither PSMA-11 nor PSMA-617 form a stable complex with ^{64}Cu or ^{67}Cu. *In vitro* studies demonstrated that PSMA-617 can be labelled with ^{64}Cu with high yield (> 99%), but a poor *in vivo* stability with high liver uptake was reported *(273, 274)*. Furthermore, *in vitro* experiments showed that DOTA and 1,4,7,10-tetra-(2-carbamoyl methyl)-cyclododecane (TCMC) allow the formation of a stable chelate complex with lead(II), DOTA at pH >3.5 and TCMC at pH >2 *(264, 275, 276)*. The chelator TCMC offers characteristics that make it more suitable for forming a stable complex with Pb(II);

however, the lead ligand was not yet systematically assessed with PSMA as a target molecule.

Therefore, there is a need for further optimization of PSMA-617. For this purpose, derivatives of PSMA-617 with modified lipophilic properties were designed. Compounds containing aromatic building blocks were found to improve its properties; in particular, a benzyl residue placed within the lipophilic pocket of PSMA triggered cellular internalization and caused favorable pharmacokinetics by reducing the amount of tracer in the kidneys *(38, 277, 278)*.

The aim of this doctoral thesis was the development of novel PSMA ligands for imaging and therapy that build upon the compound developed by Martina Benešová (MB, January, 2016) which followed the studies of the successful PSMA-11 by Matthias Eder. In the first part of this dissertation the novel theranostics were designed to be labeled with the theranostic pair ^{64}Cu/^{67}Cu. ^{64}Cu is an alternative; if the short-term PET imaging is not possible and additionally allows the dosimetry of the tracers for the therapeutic ^{67}Cu. In second project of this thesis, PSMA ligands were developed for labelling with different lead radioisotopes; for this study, the radioisotope ^{203}Pb was used as an imaging analog to obtain an approximation of the dosimetry of ^{212}Pb that was used as an *in vivo* alpha generator. In the last project, a series of PSMA ligands that comprise a benzyl group in the chelator moiety was developed to further optimize the clinically established radiopharmaceutical PSMA-617.

2. MATERIALS AND METHODS

2.1. Chemicals and Solvents

All the solvents and chemicals that were used for this study were purchased from Macrocyclics or CheMatech (Dijon, France) Sigma-Aldrich (Taufkirchen, Germany), Iris Biotech (Marktredwitz, Germany), Merck KGaA (Darmstadt, Germany). They have been utilized without any further drying or purification.

The radionuclides were sourced from the following institutions: $^{64}CuCl_2$ in 0.1 M HCl were purchased from DSD Pharma or University Hospital of Eberhard Karls University Tübingen). The ^{203}Pb-cloride in 0.1 M HCl was ordered from Lantheus Medical Imaging, USA. ^{68}Ga was eluted from a ^{68}Ge/^{68}Ga generator (iThemba LABS). [^{177}Lu]$LuCl_3$ was obtained from (Isotope Technologies Garching).

2.2. Analytical methods for characterization

Reverse-phase high-performance liquid chromatography (RP-HPLC) analysis was performed using an Agilent 1100 system with a gradient (0-100% acetonitrile in 5 min; flowrate 2 mL/min) of 0.1% TFA in water and in acetonitrile on a Chromolith Performance RP-18e column (100 × 3 mm; Merck KGaA Darmstadt, Germany). The UV-absorbance was detected at 214 nm. In order to perform the HPLC-analysis of the radioactive compounds, an additional γ-detector was used.

For characterization of the products HPLC-MS was performed on an ESI mass spectrometer (Exactive, Thermo Fisher Scientific, Waltham, MA, USA) combined with an Agilent 1200 HPLC system with a Hypersil Gold C18 1.9 µm column (200 × 2.1 mm; 0-100% acetonitrile in 20 min; flowrate 200 µL/min).

For assessment of the radiolabeled compound, the analytical radio-HPLC with a Chromolith Performance RP-18e column (100×3mm; Merck; 0–100% acetonitrile in water containing 0.1% trifluoroacetic acid in 5 min; flowrate 2 mL/min) was used.

The purification of the compounds was performed on a LaPrep P110-System (Knauer, Berlin, Germany) and a Reprosil Pur 120 column (C18-aq 5 µm 250 × 25mm; Dr. Maisch, Ammerbuch-Entringen, Germany). The gradient (10 or 15 min; flowrate 20 mL/min) was modified for some compounds when necessary.

2.3. Synthesis of the chelator moieties for radiolabeling with copper nuclides

The specific chelator moieties for copper labeling were synthesized in high yields by previously published methods and analyzed by LC-MS:

The synthesis of the chelator 4-[(1,4,8,11-tetraazacyclotetradec-1-yl)-methyl] benzoic acid, a bifunctional macrocyclic cyclam analogue, was reported previously by Studer and Kaden *(279)* and 4-carboxymethyl-11-(1,3-dicarboxypropyl)-1,4,8,11-tetraazabicyclo[6.6.2]hexadecane-pentanedioic acid, a cross-bridged chelator, was described by Boswell *et al. (280).*

The synthesis of the chelator 1-(4-methylbenzoic)-1,4,7,10-tetraazacyclododecane-4,7,10-triacetic acid for compound CA027 and CA028 was described by Kielar *et al (281)*. The chelators *p*-SCN-Bn-TCMC (ligands CA008 and CA009), DO3AM (ligands CA011 and CA012), *p*-NCS-benzyl-DOTA-GA (ligand CA029) and *p*-SCN-Bn-DOTA (ligand CA030) were purchased from CheMatech and Macrocyclics respectively. Before coupling to the PSMA-ligands, the chelators were characterized by LC-MS.

2.4. Synthesis of the binding motif plus linker

The peptidomimetic glutamate-urea-lysine binding motif and the linker moiety were synthesized by solid-phase peptide chemistry as previously described by Eder *et al*. *(38)* and Benešová *et al*. *(39)*. This synthesis is summarized in **Figure 17.** The synthesis of PSMA-binding motif was started from 0.3 mmol 2-chlorotrityl resin (polymer-bound 100-200 mesh, extent of labeling: 1.2-1.6 mmol/g loading, 1 % cross-linked; Iris Biotech, Marktredwitz, Germany) was swollen in a 5 mL syringe with water-free dichloromethane (DCM) for 45 min. The swollen resin was washed with dry DCM, then 1.2 equivalent of Fmoc-Lys(Alloc)-OH and 4.0 equivalent of N-ethyldiisopropylamine (DIPEA) in 3 mL of water-free DCM was added.

The lysine-immobilized resin was washed three times with DCM followed by incubation fifty times for 5 min with a mixture of DCM, methanol (MeOH) and DIPEA in a ratio of 17:2:1 v/v/v to remove the resin that was not reacted with lysine. Fmoc deprotection was conducted with piperidine in DMF in a ratio of 1:1 v/v for 2 min and 5 min.

To generate the isocyanate of the glutamyl moiety, 3 equivalentes of H-Glu-(Ot-Bu)-Ot-Bu x HCl, **1** were dissolved in 200 mL of 3 mL DIPEA. This solution was added drop-

wise over 4 h to 1 mmol of trisphosgene dissolved in 10 ml DCM in a round-bottom flask on ice (*Caution*: *triphosgene is toxic and fatal if inhaled*). This reaction was stirred for 16 h. The resin-immobilized Alloc and t-Bu-protected Glu-ureido-Lys, **3** was filtered and washed three times with DCM.

In the next step the Alloc-group was removed by using 0.3 equivalent of tetrakis-(triphenyl)palladium (TPP palladium), 30 equivalent morpholine in 4 mL DCM for 2 hours in the dark by using aluminum foil, resulting in compound **4.** Then the resin was washed ten times with 2% DIPEA in DMF following washes with 15 mg/mL of sodium diethyldithiocarbamate trihydrate in DMF.

2.5. Coupling of Linker Area

The coupling of Fmoc-2-naphthyl-l-alanine was conducted to obtain **(5)**. Alternatively, trans-4-(Fmoc-aminomethyl)-cyclohexanecarboxylic acid was coupled to obtain **(6).** Depending on the resin used (0.1 mmol), it is necessary for 4 equivalents of Fmoc-carboxylic acid to be activated with 3.92 equivalents of HBTU (3-[Bis(dimethylamino)methyliumyl]-3H-benzotriazol-1-oxide hexafluorophosphate) in 4 equivalents of DIPEA dissolved in DMF. The mixture is agitated for 2 min then added to the resin and incubated for 1 h in order to obtain compound **(5)** or **(6)**. The Fmoc group was removed with 50% piperidine in DMF for 2 min and 5 min.

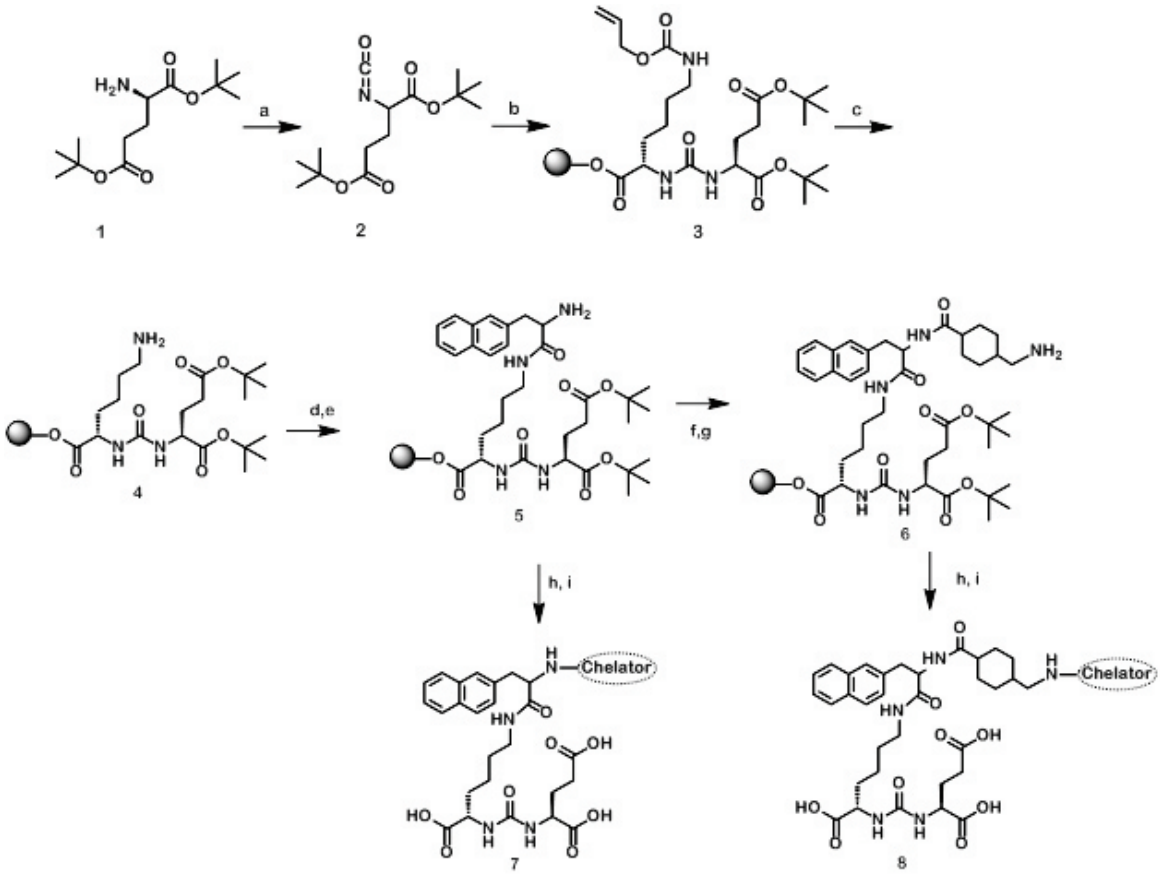

Figure 17: Reaction scheme for the synthesis of the novel PSMA ligands (a) triphosgene, diisopropylethylamine, CH2Cl2, 0 °C; (b) H-Lys(Alloc)-2CT-resin, CH2Cl2; (c) Pd[P(C6H5)3]4, morpholine, CH2Cl2; (d) Fmoc-2-Nal-OH, HBTU, diisopropylethylamine, DMF; (e) 50% piperidine, DMF; (f) trans-4-(Fmoc-aminomethyl)cyclohexanecarboxylic acid, Ethyl cyano(hydroxyimino)acetate, DIC, DMF; (g) 50% piperidine, DMF; (h) chelator, diisopropylethylamine, DMF; (i) 95% TFA, 2.5% H2O and 2.5% triisopropylsilane.

2.6. Coupling of the Chelator

2.6.1. Ligands for labeling with Copper Isotopes

Specification for CA001, CA002 and CA003

The product was obtained by incubating the peptide on the resin (compound **4**) with 1.5 equivalents of CTPA-NHS-ester (4-[(1,4,8,11-tetraazacyclotetradec-1-yl)-methyl] benzoic acid) and 10 equivalents of DIPEA in 500 µl of DMF. The compound was liberated from the solid support, 2-clorotrityl resin, with the incubation in 500 µl trifluoroacetic acid (TFA) with 12.5 µl triisopropylsilane (TIPS) and 12.5 µl water for over 60 min. 2 ml DCM were added and the solvent was removed under vacuum. 2 ml diethyl ether was added to the mixture, which was then centrifuged at 13,000 U/min. The supernatant was decanted. The mixture was washed again with diethyl ether and the precipitate was dried. The analysis was performed with an analytical HPLC and LC/MS.

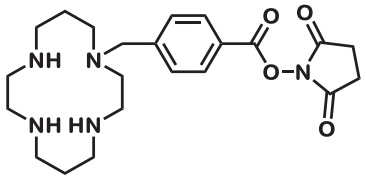

Figure 18: Chemical structure of the chelator CTPA-NHS-ester, the compound used in the synthesis of CA001, CA002 and CA003.

Specification for CA004 and CA005

The product was obtained by incubating the resin (compound **5**) with 1.5 equivalents of cross-bridged-TE2A chelator, 0.98 × $n_{chelator}$ HBTU and 10 equivalents of DIPEA in 500 µl of DMF. The compound was released from the resin as specified for the compounds CA001, CA002 and CA003. The compound was purified, and the final product was analyzed by HPLC and LC/MS.

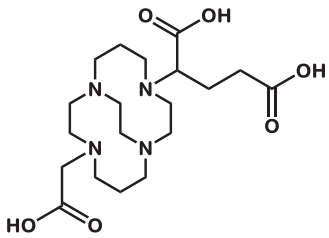

Figure 19: Chemical structure of the chelator 8-carboxymethyl-cross bridged-TE2A, the compound used in the synthesis of CA004, and CA005.

Specification for CA022

The product was obtained by incubating the resin (compound **6**) with 1.5 equivalents of cross-bridged-CTPA chelator and 10 equivalents of DIPEA in 500 µl of DMF. The compound was released from the resin as specified for the compounds CA001, CA002 and CA003. The compound was purified and the final product was analyzed by HPLC and LC/MS.

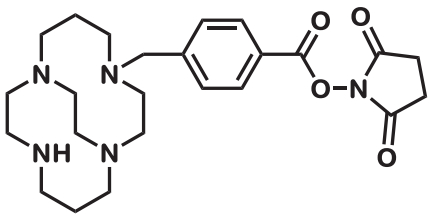

Figure 20: Chemical structure of the chelator cross-bridged-CTPA, the compound used in the synthesis of CA022

Specification CA023

The product was obtained by incubating the resin (compound **6**) with 1.5 equivalents of 8-carboxymethyl-CTPA chelator and 10 equivalents of DIPEA in 500 µl of DMF. The compound was released from the resin as specified for the compounds CA001, CA002 and CA003. The compound was purified and the final product was analyzed by HPLC and LC/MS.

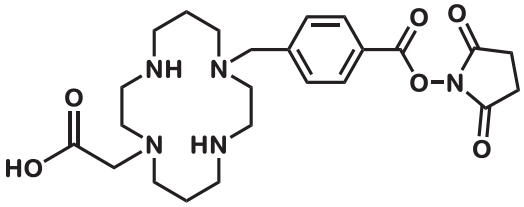

Figure 21: Chemical structure of the chelator 8-carboxymethyl-CTPA, the compound used in the synthesis of CA023.

Specification for CA024

The product was obtained by incubating the resin (compound **6**) with 1.5 equivalents of 8-carboxymethyl-cross-bridged-CTPA chelator and 10 equivalents of DIPEA in 500 µl of DMF. The compound was released from the resin as specified for the compounds CA001, CA002 and CA003. The compound was purified and the final product was analyzed by HPLC and LC/MS.

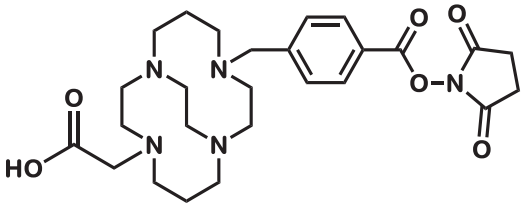

Figure 22: Chemical structure of the chelator 8-carboxymethyl-cross bridged-CTPA, the compound used in the synthesis of CA024.

Specification for CA025

The product was obtained by incubating the resin (compound **6**) with 1.5 equivalents of 8,11-*bis*(carboxymethyl)-CTPA chelator [CPTA = 4-[(1,4,8,11-tetraazacyclotetradec-1-yl)methyl]benzoic acid] and 10 equivalents of DIPEA in 500 µl of DMF. The compound was released from the resin as specified for the compounds CA001, CA002 and CA003. The compound was purified and the final product was analyzed by HPLC and LC/MS.

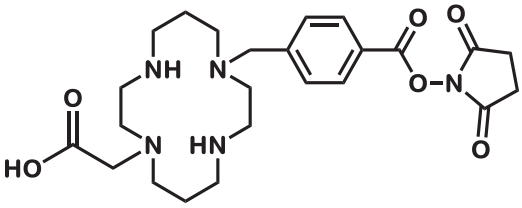

Figure 23: Chemical structure of the chelator 8,11- *bis*(carboxymethyl)-CTPA, the compound used in the synthesis of CA025.

Specification for CA026

The product was obtained by incubating the resin (compound **6**) with 1.5 equivalents of 8,11- *bis*(carboxymethyl)-CTPA chelator and 10 equivalents of DIPEA in 500 µl of DMF. The compound was released from the resin as specified for the compounds CA001, CA002 and CA003. The compound was purified and the final product was analyzed by HPLC and LC/MS.

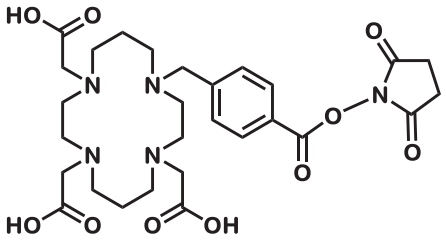

Figure 24: Chemical structure of the chelator 4, 8,11-tris(carboxymethyl)-CTPA, the compound used in the synthesis of CA026.

2.6.2. Ligands for radiolabeling with Lead-Isotopes

Specification for CA007, CA008 and CA009

The product was obtained by incubating the resin (compound **5**) with 1.5 equivalents of *p*-SCN-Bn-TCMC chelator [TCMC = 1,4,7,10-tetraaza-1,4,7,10-tetra(2-carbamoylmethyl)cyclododecane] and 10 equivalents of DIPEA in 500 µl of DMF. The compound was released from the resin as specified for the compounds CA001, CA002 and CA003. The compound was purified, and the final product was analyzed by HPLC and LC/MS.

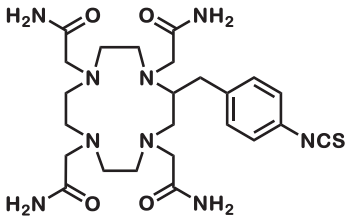

Figure 25: Chemical structure of the chelator *p*-SCN-Bn-TCMC, the compound used in the synthesis of CA007, and CA008, CA009.

Specification for CA010, CA011 and CA012

The product was obtained by incubating the resin (compound **5**) with 1.5 equivalents of 2-(4,7,10-tris(2-amino-2-oxoethyl)-1,4,7,10-tetraazacyclododecan-1-yl)acetic acid, the monocarboxylate derivative of the chelator 1,4,7,10-tetraazacyclododecane-1,4,7,10-tetraacetamide (DO3AM), 0.98 × $n_{chelator}$ HBTU and 10 equivalents of DIPEA in 500 µl of DMF. The compound was released from the resin as specified for the compounds CA001, CA002 and CA003. The compound was purified and the final product was analyzed by HPLC and LC/MS.

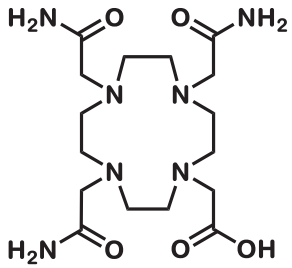

Figure 26: Chemical structure of the chelator 2-(4,7,10-tris(2-amino-2-oxoethyl)-1,4,7,10-tetraazacyclododecan-1-yl)acetic acid, the monocarboxylate derivative of the chelator 1,4,7,10-tetraazacyclododecane-1,4,7,10-tetraacetamide (DO3AM), the compound used in the synthesis of CA010, CA011 and CA012.

2.7. Chelator Spacer Moieties Enhancing the Pharmacokinetics of PSMA-617

Specification for CA027 and CA028

The product was obtained by incubating the resin (compound **4**) with 1.5 equivalents of *p*-NHS-Bn-DOTA chelator and 10 equivalents of DIPEA in 500 µl of DMF.

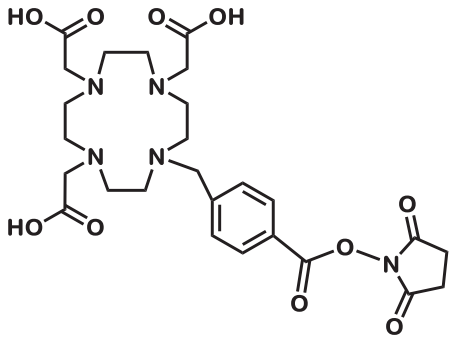

Figure 27: Chemical structure of the chelator *p*-NHS ester-Bn-DOTA, used for the synthesis of CA027 and CA028

The product was obtained by incubating the resin (compound **6**) with 1.5 equivalents of *p*-NHS-Bn-DOTA chelator and 10 equivalents of DIPEA in 500 µl of DMF. The compound was released from the resin as specified for the compounds CA001, CA002

and CA003. The compound was purified and the final product was analyzed by HPLC and LC/MS.

Specification for CA029

The product was obtained by incubating the resin (compound **6**) with 1.5 equivalents of *p*-SCN-Bn-DOTA chelator and 10 equivalents of DIPEA in 500 µl of DMF. The compound was released from the resin as specified for the compounds CA001, CA002 and CA003. The compound was purified and the final product was analyzed by HPLC and LC/MS.

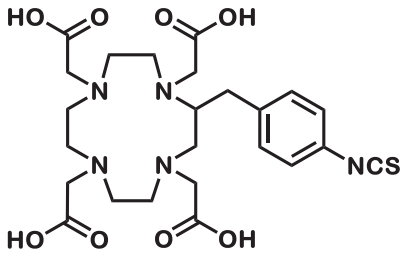

Figure 28: Chemical structure of the chelator *p*-SCN-Bn-DOTA, the compound used in the synthesis of CA029.

Specification for CA030

The product was obtained by incubating the resin (compound **6**) with 1.5 equivalents of *p*-NCS-benzyl-DOTA-GA chelator and 10 equivalents of DIPEA in 500 µl of DMF. The compound was released from the resin as specified for the compounds CA001, CA002 and CA003. The compound was purified and the final product was analyzed by HPLC and LC/MS.

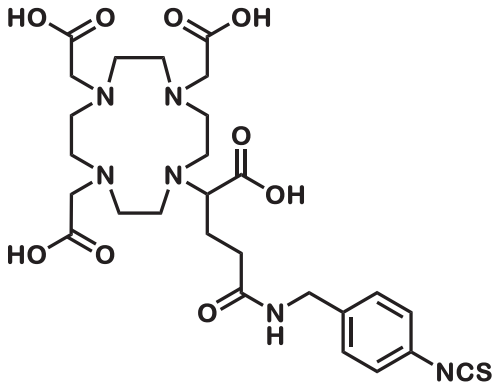

Figure 29: Chemical structure of the chelator p-NCS-benzyl-DOTA-GA, the compound used in the synthesis of CA030.

2.8. Radiochemical Synthesis

2.8.1. Radiolabeling of ^{64}Cu-PSMA Derivatives

The conjugates specific for radiolabeling with copper (1 mM in water, 5 µL, 5 nmol) were added to a mixture of 400 µL of sodium acetate buffer (0.4 M in water, pH 5.0), 10 µL of ascorbic acid (20% in water), and 282 µL of $^{64}CuCl_2$ (DSD Pharma) in 0.1 M HCl (200 MBq). The mixture was heated at 95 °C for 5 min. The checked pH of the labeling solution for all compounds was between 4 and 5. The labeling was controlled by radio-HPLC (0–100% acetonitrile in 5 min, monolithic column), with a flow rate of 2 mL/min.

2.8.2. Radiolabeling of ^{203}Pb-PSMA Derivatives

For ^{203}Pb-labeling, eighty nmol of the compounds (1 mM in water, 80 µl, 80 nmol) was mixed with 400 µl sodium acetate buffer (0.4 M in water, pH 5.0), 10 µl ascorbic acid (20% in water) and 140 µl ^{203}Pb-chloride solution in 0.04 M HCl with specific activity approx. 102.6 TBq/g (Lantheus Medical Imaging, USA). Afterwards the mixture was heated at 95 °C for 5 min. The radiolabeled compounds were checked by radio-HPLC.

2.8.3. Radiolabeling of the ^{68}Ga/^{177}Lu-PSMA-617 Derivatives

^{68}Ga-Labeling

^{68}Ga was eluted from a ^{68}Ge/^{68}Ga generator (iThemba LABS). To a mixture of 320 µL sodium acetate buffer (0.4 M in water, pH 4–5), 10 µL ascorbic acid (20% in water) and 400 MBq ^{68}Ga in 0.6 M HCl, 20 nmol of the conjugates (1 mM in DMSO) were added with a final pH between 3.6 and 4.2. After heating at 95 °C for 5 min, the labeling was controlled by radio-HPLC (0–100% ACN in 5 min, Monolith column, Merck), with a flow rate of 2 mL/min.

^{177}Lu-Labeling

Approximately 20 MBq [^{177}Lu]$LuCl_3$ (Isotope Technologies Garching) was initially mixed with 200 µL of 0.4 M sodium acetate buffer (pH = 5). 40 µL of the solution were mixed with 2 µL of a 1 mM solution of the conjugates (in 10% DMSO in water) and 2 µL of a 20% (w/w) solution of ascorbic acid (in water) and heated to 95 °C for 10 min. The pH of

the labeling solution was approximately 5.0. The labeling was checked by radio-HPLC as described above.

2.9. Serum stability of the radiolabeling compounds

2.9.1. Stability of the ^{64}Cu-labeled compounds

The stability of the compounds radiolabeled with ^{64}Cu was determined by instant thin-layer chromatography (ITLC) and HPLC analysis. A 50 *μ*L (20 MBq) volume of the ^{64}Cu-labeled ligands was added to 200 μL of human serum (Sigma-Aldrich) and incubated at 37 °C for different time points (0, 2, 24, 48, and 72 h). Strips of ITLC silica-gel glass microfiber chromatography paper (0.5 × 5 cm; Agilent Technologies) were used. A 0.5 *μ*L volume of the radiolabeled complex in serum was applied to each strip at 1 cm from the bottom (origin), and the solvent (1% sodium-ethylenediaminetetraacetic acid, pH 4) was allowed to rise to 5 cm from the bottom of the strip to the front. Finally, each strip was cut into 8 pieces, and each piece was measured in a gamma-counter. For HPLC analysis, an equal volume of acetonitrile was added to the samples to precipitate the serum proteins. Subsequently, the samples were centrifuged for 10 min at 13,000 rpm, the pellet and supernatant were separated, and the relative activity was measured. The results are expressed as a percentage. In addition, an aliquot of the supernatant was analyzed by radio-HPLC (0%–100% acetonitrile in 5 min, monolithic column) with a flow rate of 2 mL/min.

2.10. Stability of the ^{203}Pb-labeled compounds

The stability of the compounds radiolabeled with ^{203}Pb was evaluated in 300 μL human serum (Sigma-Aldrich) at 37 °C up to 72 h. The serum was precipitated by the addition of 2 parts acetonitrile, centrifuged for 5 min at 13,000 rpm (2 times) and the supernatant was analyzed by radio-HPLC (0-100% acetonitrile in 5 min, monolith column).

2.10.1. Stability of the ^{68}Ga/^{177}Lu- labeled compounds

The serum stability was assessed by instant thin layer chromatography (ITLC) and HPLC after the radiolabeling of the compounds took place. 50 μL (20 MBq) of the ^{177}Lu-labeled ligands were combined with 200 μL of human serum (Sigma-Aldrich) and incubated at 37

°C. At different time-points (0, 2 h, 24 h, 48 h and 72 h) 0.5 µL was applied onto an iTLC-SG-glass microfiber chromatography paper strip (5 x 0.5 cm; Agilent Technologies) at a distance of 1 cm from the bottom. The strip was placed upright into a vial containing 120 µL of sodium citrate buffer (0.5 M, pH = 5.0). The buffer was allowed to rise to the top before each strip was cut into 8 equally-sized pieces and measured in a gamma-counter. For HPLC analysis, an equal volume of acetonitrile was added to the samples to precipitate the serum proteins. Subsequently, the samples were centrifuged for 10 min at 13,000 rpm, the pellet and supernatant were separated, and their relative activity (%) was determined. In addition, an aliquot of the supernatant was analyzed by radio-HPLC (0–100% ACN in 5 min, Monolith column, Merck), with a flow rate of 2 mL/min.

2.11. *In vitro* Experiments

By using the PSMA-positive C4-2 cell line, a subline of the LNCaP (human lymph node carcinoma of the prostate) cell line (CRL-3314; American Type Culture Collection) the competitive assay was conducted. The cells were cultivated in RPMI 1640 (PAN Biotech) medium supplemented with 10% fetal calf serum and stable glutamine (PAN Biotech). Cells were grown at 37° C in humidified air equilibrated with 5% CO_2.

2.11.1. Competitive cell binding assay

At first, a MultiScreen$_{HTS}$-DV filter plate was coated at room temperature with 100 µL PBS (phosphate-buffered saline) containing 1% BSA (bovine serum albumin) per well for 30 min. Afterwards the PBS/BSA solution was removed and 1×10^5 C4-2 cells were added in Opti-MEM to each well. The inhibitory potency of the synthesized compounds was determined using 0.75 nM of ^{68}Ga-labeled PSMA-HBED-CC dimer (^{68}Ga-PSMA-10) *(282)* as a standard. All non-labeled compounds were dissolved in Opti-MEM at the following concentrations: 0, 0.5, 1, 2.5, 5, 10, 25, 50, 100, 500, 1,000 and 5,000 nM. This mixture was incubated at 37° C for 45 min. Afterwards, the cells were washed twice with PBS on a multiscreen vacuum manifold (Millipore, Billerica, MA) and the cell-bound radioactivity was measured with a gamma counter (Packard Cobra II, GMI, Minnesota, USA). The 50% inhibitory concentration (IC_{50}) was calculated using a nonlinear regression algorithm (Graph Pad Prism 5.01 software). The experiments were performed in quadruplicate.

2.11.2. Determination of internalization ratio

To evaluate the internalization of the PSMA ligands, two 24-well plates were coated with 0.1% poly-L-lysine in PBS for 20 min at room temperature and then washed once with PBS. Then, 1 mL RPMI medium containing 10^6 C4-2 cells was added to each well and incubated overnight before the experiment. The conditions during the experiment for each compound were: 37° C and 4° C, incubation with and without receptor blocking with 2-(phosphonomethyl)pentanedioic acid (2-PMPA, Axxora) at a final concentration of 500 µM. Afterwards, the cells in each well were incubated with 250 µL of a 30 nM solution of the radiolabeled compounds. The plates were incubated for 45 min in a water bath at 37° C or on ice at 4° C. Subsequently, the cells were washed 3 times with 1 mL of ice-cold PBS and incubated with 0.5 mL glycine (50 mM) in HCl pH 2.8 for 5 min. After an additional washing step with 1 mL of ice-cold PBS, the cells were lysed with 0.5 ml of 0.3 M NaOH, collected and the radioactivity measured with a gamma-counter Packard Cobra II for 1 min and calculated as % of applied activity (%IA) per 10^6 C4-2 cells. The internalization assay was performed in duplicate or triplicate and data were expressed as means ± whose p values <0.05 were considered statistically significant.

The specific cell surface binding and specific uptake into the cell lysate were additionally calculated by subtracting the non-specific cell surface binding and the non-specific lysate fraction, and the result was also expressed as %IA/10^6 C4-2 cells.

2.12. *In vivo* Characterization

The *in vivo* experiments were carried out in accordance with the laws of the German Federal Republic. For PET imaging and biodistribution studies, male nude mice (Balb/c *nu/nu* mice) (19–23 g) were obtained from Charles River at 4–5 weeks of age and kept under specific-pathogen-free conditions for 1 week prior to the study. The mice were housed with a 12-hour/12-hour light/dark cycle and had free access to water and food. The mice were anesthetized with 2% sevoflurane and inoculated subcutaneously on the right trunk with 5 × 10^7 C4-2 cells in 50% Matrigel in Opti-MEM I (1 ×) medium. Organ distribution studies were performed, when the size of the tumor was approximately 1 cm^3.

2.12.1. Stability in Blood of ^{64}Cu-labeled CA003

The stability of ^{64}Cu-labeled CA003 *in vivo* was assessed by ITLC and HPLC. Male BALB/c nude mice without tumor (*n* = 3) were injected via the tail vein with ^{64}Cu-CA003 (3.6 MBq; 0.26 nmol, dissolved in a total volume of approximately 100 µL of 0.9% saline) and 800 µL blood was harvested 10 min post injection. After the blood sample was centrifuged for 10 min at 13,000 rpm the supernatant and pellet were separated. Subsequently the relative activity was measured. In order to assess the stability of the radiolabeled compound in the serum ITLC was performed. Furthermore, an aliquot of the supernatant was analyzed by radio-HPLC (0–100% ACN in 5 min, Monolith column), with a flow rate of 2 mL/min after the addition of an equal volume of acetonitrile and removal of the proteins by centrifugation.

2.12.2. *In vivo* Fate of ^{64}Cu-labeled CA003 and ^{64}Cu-Cloride

The metabolism *in vivo* was assessed by radio-HPLC analysis. For this study, female Swiss mice (*n* = 3) without tumor were injected via the tail vein with ^{64}Cu-chloride (10 MBq in approximately 100 µL of 0.9% saline) or ^{64}Cu-CA003 (9 MBq, 0.30 nmol in approximately 100 µL of 0.9% saline). PET imaging was performed 10 min post injection and subsequently blood, the liver and the kidneys were harvested. These tissues were rinsed with precooled saline, blotted dry and treated with 2 mL of 0.1 M NH_4OAc/EtOH (35:65). The tissues were homogenized using an Ultra-Turrax T8 (IKA Labortechnik, Germany). The samples were centrifuged for 10 min at 13,000 rpm (4° C). Subsequently, the pellet and supernatant were separated and the relative activity was measured. The results are expressed as percent. Additionally, an aliquot of supernatant was prepared for HPLC measurement by precipitation of the proteins with acetonitrile. The sample was analyzed by radio-HPLC (0–100% acetonitrile in 5 min, Monolith column), with a flow rate of 2 mL/min. Fractions were collected every ten seconds over the whole course of the chromatography and the relative activity of the samples was measured in a gamma-counter to reconstruct a chromatogram.

2.12.3. Dynamic and Static PET Scans

For small-animal PET imaging with various ^{64}Cu-labeled PSMA ligands, 0.2 nmol, 10 MBq of approximately 100 µL in 0.9% saline the radiolabeled compound were injected into a C4-2 tumor bearing mouse. For PSMA-ligands derivatives of PSMA-617

radiolabelled with ^{68}Ga (0.5 nmol, 20 MBq in approximately 100 µL 0.9% saline) were injected also into C4-2 tumor bearing mice. The dynamic PET was recorded in a small animal PET scanner (Siemens Inveon D-PET, Malvern, PA USA). The SUV values were obtained from conventional (non-dynamic) PET images. The formula for the SUV was:

$$\mathrm{SUV} = \frac{activity\ in\ ROI\ \left(\frac{Bq}{ml}\right) \times\ animal\ weight\ (g)}{injected\ dose\ (Bq)}$$

The volumes-of-interest (VOIs) were obtained by manual delineation of the appropriate whole tissue (heart, kidneys, bladder, tumor - with an approximate volume of 100–500 *µ*L) - or parts of the tissue liver and muscle). The images were reconstructed based on the procedure: OSEM 3D/SP MAP with 16 subsets, 2 iterations and an image x-y size: 256, image z size: 161. The data were not modified with a post processing filter. The software used to analyze images and TACs was Inveon™ Acquisition Workplace (IAW) from Siemens IRW 4.1. Dynamic PET scans were performed 0–60 min post injection, and images were reconstructed in three time frames of 20 min (0–20 min, 20–40 min and 40–60 min) for visual display. For some compounds that showed long retention later time points (2 h, 4 h, 20 h, 45/48 h) were included. After 1 h a static PET scan was generated. In order to compare the different radiotracers, the mean SUVs were plotted over time.

2.12.4. Scintigraphic Imaging of the ^{203}Pb-labeled compounds

For in vivo planar scintigraphy imaging of ^{203}Pb-labeled compounds the mice were anesthetized with 2% sevoflurane. For each ^{203}Pb-ligand 0.1 nmol (1.0 MBq) was injected into the tail vein. By using a Gamma Imager SCT (Biospace Lab, Paris, France) with a parallel collimator (35 mm/1.8 mm/0.2 mm) a series of scintigraphy imaging were scanned after 10 min, 1 h, 4 h, 24 h post-injection.

2.12.5. Biodistribution studies in mice

Based on the results of the PET imaging CA003, the most promising compound among all ligands radiolabeled with copper, was used for biodistribution study in C4-2 tumor bearing mice. 0.025 nmol of the ^{64}Cu-labeled compound (1 MBq per mouse in approximately 100 *µ*L of 0.9% saline) was administered by tail vein injection. At the time points: 10 min, 1 h, 4 h, 24 h and 72 h the organs were dissected and weighed and the activity was measured.

After evaluation of scintigraphic imaging of the ^{203}Pb-labeled compounds, compound CA012 was chosen for biodistribution studies. For this study 0.025 nmol (1 MBq) of labeled compound per mouse was administered by injection into the tail vein. After 10 min, 1 h, 4 h, and 24 h the mice were euthanized, the organs were dissected, weighed and activity was measured.

On the basis of the results of PSMA-617 derivatives, the most promising compounds ^{68}Ga-CA028 and ^{68}Ga-CA030 were chosen for biodistribution studies in C4-2 tumor-bearing mice. The ^{68}Ga radiolabeled compound (0.05 nmol, 20 MBq) was administered to the mice. Animals were sacrificed and organs were harvested at the following time-points: 20 min, 1 h, 2 h and 4 h post-injection by using a γ-counter (Packard Cobra Auto-gamma) the activity was measured. Experiments were performed in triplicate. The organ uptakes were calculated as percent of the injected dose per gram of tissue (% ID/g).

2.12.6. Biodistribution in human PET scan

The ^{64}Cu-CA003, ^{203}Pb-CA012, ^{68}Ga-CA028 and ^{68}Ga-CA030 were assessed in a first patient in accordance with Declaration of Helsinki paragraph-37 and to the laws of the German Federal Republic.

2.12.7. ^{64}Cu-CA003

The Imaging of ^{64}Cu-CA003 was performed as previously described by Afshar-Oromieh *et al (93)*. Images were obtained with ^{64}Cu-CA003, which was applied by intravenous injection (200 MBq and 5 nmol ligand). The diagnostic examination of ^{64}Cu-CA003 was conducted at 2 h and 20 h post injection whereas for ^{68}Ga-PSMA-617 used as reference the time points were 1 h and 3 h **(Figure 50 and Table 16)**. The activity distributions of the source organs were determined with the clinical standard software Syngo (Siemens), which was used to define the volume-of-interest (VOIs).

2.12.8. ^{203}Pb-CA012 Dosimetry and Extrapolation to ^{212}Pb-CA012

Two patients diagnosed with castration-resistant metastasized prostate cancer underwent planar whole-body scans (GE Hawkeye Millennium, 1” crystal, ME-collimator,

279 keV peak +/-10%, 8cm/min). The serial scans were performed at 0.4 h, 4 h, 18 h, 28 h and 42 h post-injection. The dosage of 258 and 310 MBq ^{203}Pb-CA012, respectively was administered. The images from the serial scans were analyzed with the QDOSE dosimetry software suite (ABX-CRO, Dresden). The following tissues were segmented: urinary bladder, salivary glands (both left and right of parotid and submandibular glands), liver, kidneys, several tumor lesions, spleen as well as a total-body region-of-interest (ROI). By using percentages of maximum thresholds (15-65%) depending on the organ the most suitable time-point were identified and propagated to all other time-points by performing an additional organ-based automatic rigid co-registration step. To determine time-activity-curves (TAC) for each organ, the tumors and the total body ROIs were used for each tissue. To calibrate the ROI-counts to injected activity (MBq) the first time-point (before voiding) of the uncorrected geometric mean images could be used. Of each patient 6 samples of venous blood were drawn. By using established model assumptions, red marrow TAC was determined (275, 276). QDOSE, automatically corrects all time-points for the physical decay of the source isotope using the replacement nuclide and is leaving only its biological clearance. All TACs derived from the 203Pb data were re-calculated. Then the physical decay of the replacement radionuclide was applied. The data was evaluated by bi-exponential curve fitting.

2.12.9. PSMA-PET/CT of ^{68}Ga-CA028 and ^{68}Ga-CA030

Diagnostic PSMA-PET/CT examinations were performed 1 h and 3 h after antecubital injection of 339 MBq / 20 nmol ^{68}Ga-CA028 or 295 MBq / 20 nmol ^{68}Ga-CA030 per patient, respectively. The method for assessing the biodistribution was performed as previously described by Afshar-Oromieh *et al*. *(93)*. The activity distributions of the source organs were determined with the clinical standard software Syngo (Siemens), which was used to define the VOIs in the PET images. This reference *(93)* was also used as a standard of reference for ^{68}Ga-PSMA-617 (Table 17).

3. RESULTS

3.1. Synthesis

The synthesis of the binding motif conjugated with the linkers 2-naphthyl-L-alanine or cyclohexanecarboxylic acid was followed by the coupling of various chelators. After cleavage from the resin and purification by HPLC, the conjugates were obtained in yields of approximately 40% at a purity of 95% as determined by HPLC. The chemical structures of the ligands of the 9 newly-developed copper-labeled PSMA ligands are shown in **Figure 30**. These novel compounds have PSMA-617 as a basic structure, however, with a stable chelator that ensures the labeling with copper radioisotopes. In **Figure 31** the structures of the synthesized and characterized compounds for labelling with lead radioisotopes are presented. In order to optimize the radiopharmaceutical PSMA-617, new compounds were designed and developed with this compound as a reference, see structure in **Figure 32**.

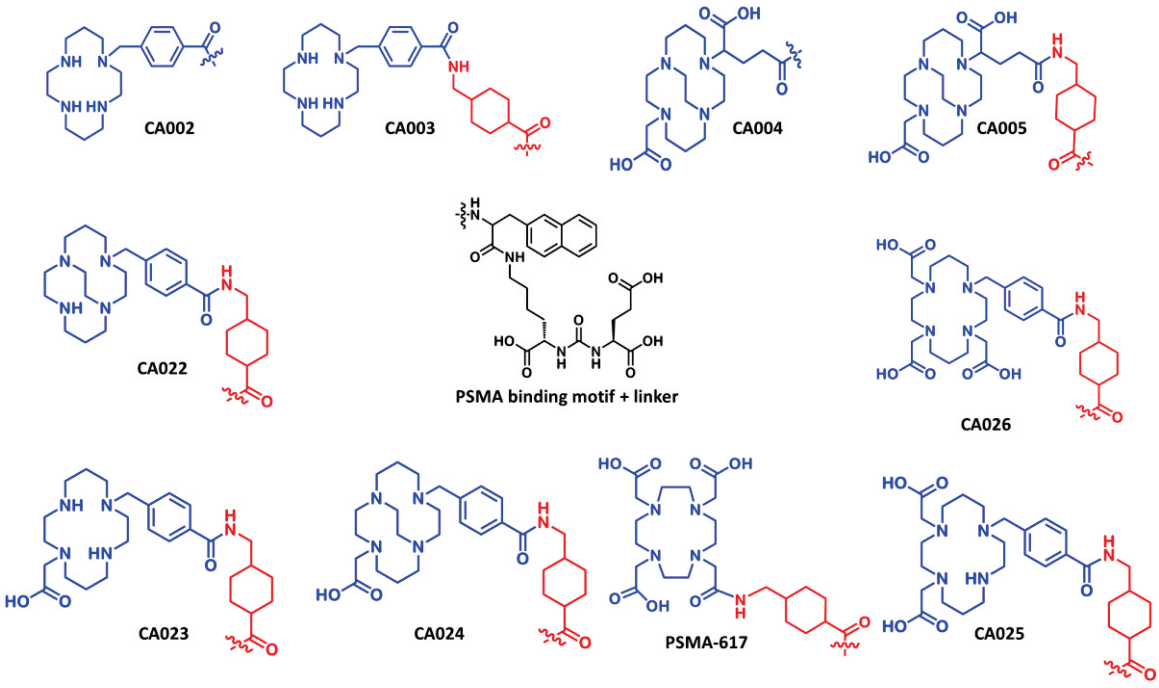

Figure 30: Chemical structures of the ligands suitable for copper labeling with the reference ligand PSMA-617.

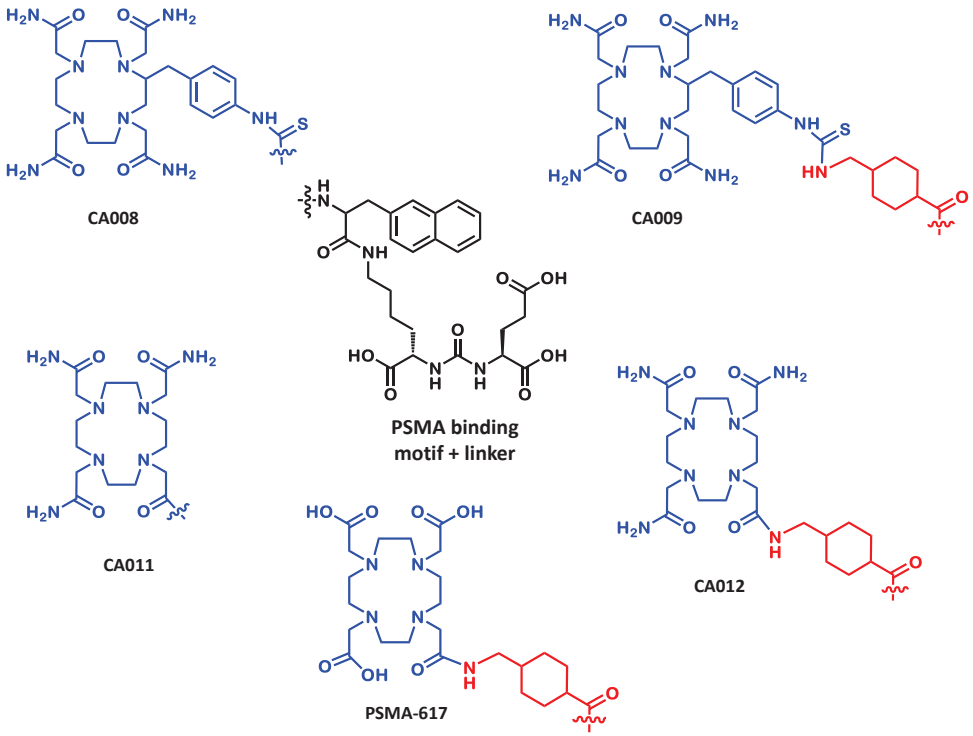

Figure 31: The synthesized compounds suitable for labeling with lead radioisotopes based on PSMA-617.

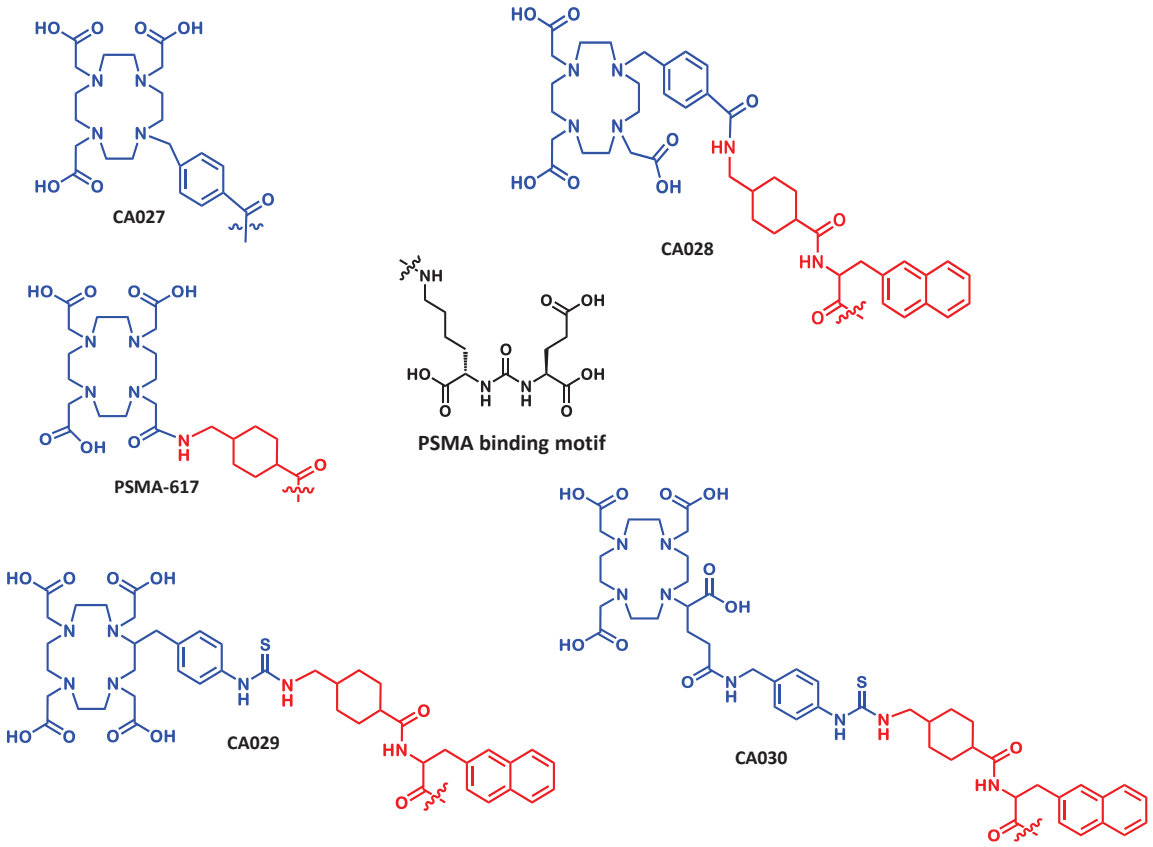

Figure 32: Chemical structures of the novel ligands based on the urea motif compared to the reference PSMA-617

The analytical data of the synthesis are summarized in **Table 8** for the compound labeled with copper radioisotopes**. Table 9** displays the data of the Pb-ligands and in **Table 10** the data from the analysis of the derivatives of PSMA-617 are presented. The results showed the HPLC retention time of the radiolabeled compounds and the mass spectrometry of nonlabeled ligands detected as $[M+H]^+$.

Table 8: Analytic Data of Copper Ligands

Compound	Molecular weight (g/mol)	[^{64}Cu-Ligand]-HPLC retention time (min)	m/z experimental**
CA002	832.45	2.39	833.42
CA003	971.55	2.37	972.51
CA004	912.46	2.38	913.60
CA005	1051.56	2.61	1052.53
CA022	997.56	2.71	998.53
CA023	1029.55	2.59	1030.53
CA024	1055.57	2.66	1056.54
CA025	1087.56	2.58	1088.53
CA026	1145.56	2.58	1146.53

*HPLC column Chromolith Performance RP-18e 100 × 3 mm, 0-100% acetonitrile in water + 0.1% trifluoroacetic acid; **Mass spectrometry of non-labeled ligands detected as $[M+H]^+$

Table 9: Analytic Data of Pb-Ligands

Compound	Molecular weight (g/mol)	[^{203}Pb-Ligand]-HPLC retention time (min)*	m/z (determined) **
CA008	1063.49	2.52	1064.49
CA009	1202.59	2.60	1203.59
CA011	899.45	2.16	900.45
CA012	1038.55	2.40	1039.55

*HPLC column Chromolith Performance RP-18e 100 × 3 mm, 0-100% acetonitrile in water + 0.1% trifluoroacetic acid; **Mass spectrometry of non-labeled ligands detected as $[M+H]^+$

Table 10: Analytic Data of the derivatives of PSMA-617

Compound	Molecular weight (g/mol)	[^{68}Ga-Ligand]-HPLC* retention time (min)	m/z** experimental
CA027	781.35	1.55	782.33
CA028	1117.53	2.37	1118.53
CA029	1206.52	2.60	1207.52
CA030	1277.56	2.61	1278.56

*HPLC column Chromolith Performance RP-18e 100 × 3 mm, 0-100% acetonitrile in water + 0.1% trifluoroacetic acid; **Mass spectrometry of non-labeled ligands detected as $[M+H]^+$

3.2. Radiolabeling

The radiolabeling of the 0.2 nmol ligands at 95° C with ^{64}Cu resulted in a labeling efficiency > 98% within 10 min. The specific activity of the ^{64}Cu-labeled compound was approximately 40 MBq/nmol. With the same protocol used for radiolabeling with ^{64}Cu, the compounds were also labeled successfully with ^{67}Cu. The ligands developed for labeling with ^{203}Pb were complexed within 5 min at 95° C and led to yields of more than 98%. The derivatives of PSMA-617 as well as the above radiolabeled compounds showed high labeling efficiency.

3.3. Serum Stability

The stability of the radiolabeled compounds was evaluated in human serum. The results of three main compounds are presented in **Figure 33**. The studied compounds were: CA003 - containing the chelator (4-[(1,4,8,11-tetraazacyclotetradec-1-yl)-methyl]benzoic acid (CTPA), CA005 - containing a cross-bridged chelator and PSMA 617 - containing an unmodified DOTA chelator. The compounds were radiolabeled with ^{64}Cu and incubated for up to 72 h in human serum. The stability was assessed by ITLC and HPLC. Up until 2 h incubation, ITLC demonstrated that all compounds dissociate to a degree of less than 2 ± 0.6%. After 24 h incubation only 6 ± 4% of 64Cu-CA003 and 3 ± 1% of ^{64}Cu-CA005 were found to be dissociated. In comparison, 64Cu-PSMA-617 showed 13 ± 3% of free ^{64}Cu activity.

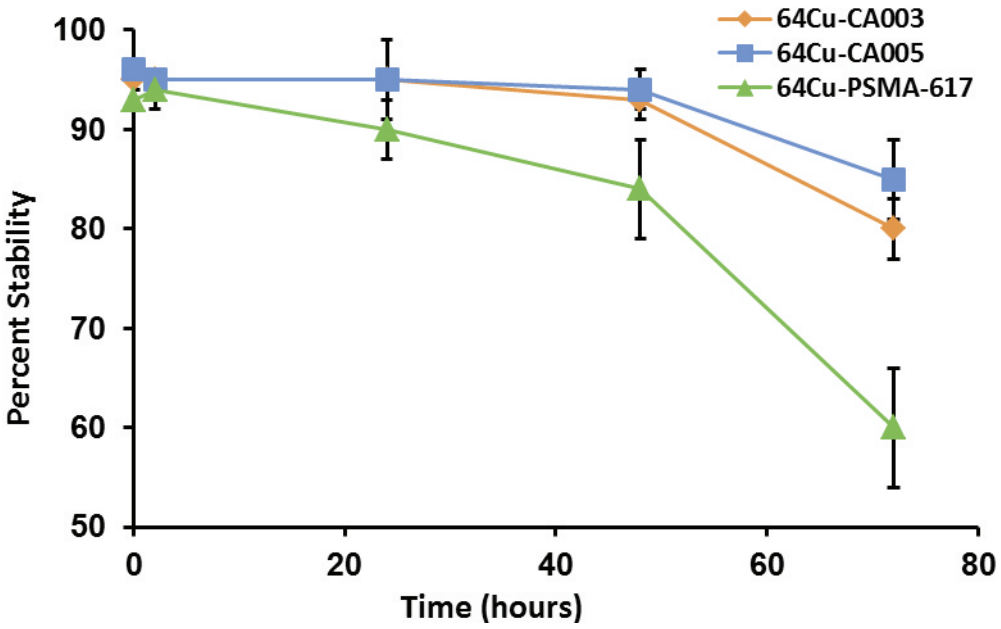

Figure 33: Serum stability of ^{64}Cu-CA003, ^{64}Cu-CA005 and ^{64}Cu-PSMA-617 at 37 °C over 72 h (mean ± SD, *n* = 4) as determined by radio-ITLC.

A study of long-term stability up to (72 h) revealed that 64Cu-CA005 (8 ± 4%) possesses stability comparable to ^{64}Cu-CA003 (11 ± 3%). At this point in time, 18 ± 6% of ^{64}Cu-PSMA-617 was found to be dissociated. After incubation for 2 h, activity measurement in the pellet **(**Figure 34**)** revealed that 19.0 ± 5.2% of ^{64}Cu-CA003, 12 ± 7.2% of ^{64}Cu-CA005 and 40 ± 7.5% of ^{64}Cu-PSMA-617 was precipitated with the protein fraction. The highest amount of activity was measured in the pellet of ^{64}Cu-PSMA-617 followed by ^{64}Cu-CA003, and less activity was found to be precipitated for ^{64}Cu-CA005.

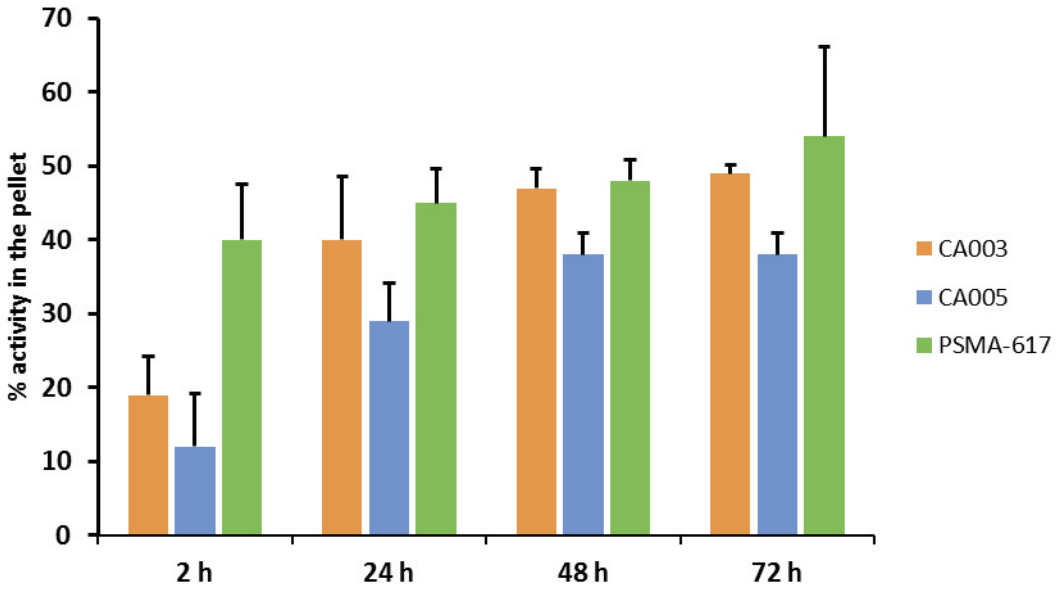

Figure 34: Serum stability of ^{64}Cu-CA003, ^{64}Cu-CA005 and ^{64}Cu-PSMA-617 at 37 °C over 72 h (mean ± SD, n = 4) as determined by activity measurement.

The ^{203}Pb-labeled PSMA-ligands demonstrated high stability in serum up to 72 h. The stability of the compounds radiolabeled with ^{68}Ga and ^{177}Lu was studied in human serum.

The stability of the derivatives of PSMA-617 was also assessed in human serum. The HPLC and radio-ITLC data indicated that the ^{68}Ga-labeled compounds did not show degradation after incubation for 2 h in human serum. In contrast to ^{177}Lu-CA029, ^{177}Lu-CA030 and the reference compound ^{177}Lu-PSMA-617 that showed no release of ^{177}Lu, analysis of ^{177}Lu-CA028 revealed 40% of free activity at this time point (**Figure 35**).

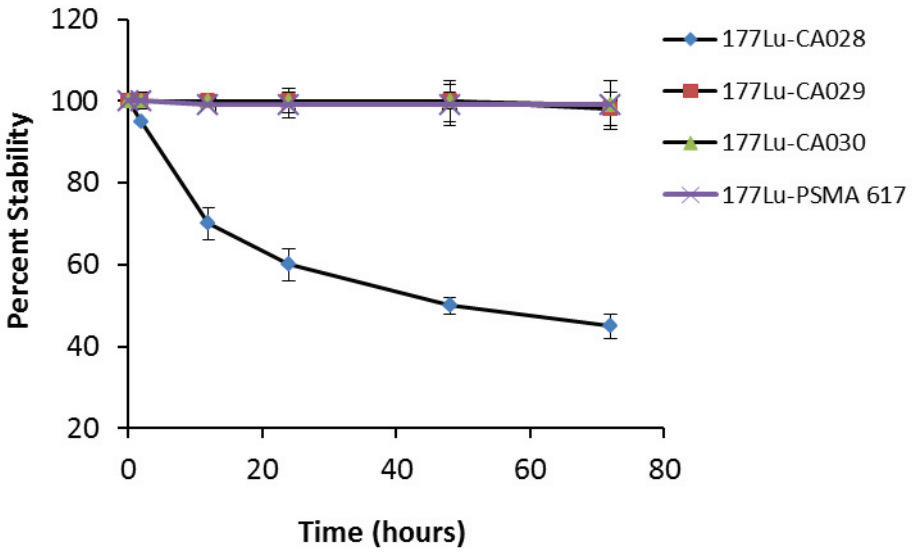

Figure 35: Serum stability of ^{177}Lu-CA028, ^{177}Lu-CA029, ^{177}Lu-CA030 in comparison with ^{177}Lu-PSMA-617 at 37 °C over 72 h (mean ± SD, *n* = 3) as determined by radio-ITLC.

3.4. Competitive Cell-Binding and Internalization ratios

For competitive cell-binding affinities (K*i*) studies, C4-2 cells, a subline of the PSMA-expressing cell line LNCaP, were used. All synthesized ligands revealed nanomolar binding affinities to PSMA. It is demonstrated in **Table 11** that CA003 revealed the highest affinity to PSMA, followed by CA005, CA002 and CA026. Moreover, the ^{64}Cu-labeled compounds showed specific binding to C4-2 cells. 34.63 ± 2.77% of ^{64}Cu-CA003, 18.63 ± 4.46% of ^{64}Cu-CA005 and 38.7 ± 6.69% of ^{64}Cu-CA022 were internalized (*n* = 3). 10^6 C4-2 cells were used for these experiments.

Table 11: PSMA Inhibition Potencies (Ki) and Specific Internalization Values of the novel developed ligands for copper labeling

Compound	K_i (nM)	Specific cell surface (% IA/10^6cells)	Specific lysate (% IA/10^6 cells)
CA002	1.9 ± 0.70	48 ± 3.9	16 ± 2.4
CA003	1.6 ± 0.52	94 ± 6.9	35 ± 2.8
CA004	15 ± 0.89	45 ± 3.4	13 ± 2.2
CA005	1.8 ± 0.65	41 ± 4.3	19 ± 4.5
CA022	12 ± 2.0	123 ± 22	39 ± 6.7
CA023	14 ± 2.0	103 ± 6.6	28 ± 8.7
CA024	21 ± 4.0	35 ± 5.8	8.6 ± 7.0
CA025	14 ± 1.7	68 ± 11	16 ± 8.0
CA026	4.4 ± 1.6	96 ± 16	24.5 ± 14
PSMA-617	2.3 ± 2.9	45 ± 3.6	15 ± 3.0

Data are mean ± SD (*n* = 3)

Despite their similar binding-affinities, ^{203}Pb-CA008 and ^{203}Pb-CA011 presented not significant internalization ratio. In contrast, the compounds ^{203}Pb-CA009 showed an internalization rate of up to 27.37 ± 2.37 and for ^{203}Pb-CA012, 15.63 ± 2.06 injected activity/10^5 C4-2 cells (*n* = 3) **(Table 12).**

Table 12: PSMA inhibition potencies (Ki) and specific Internalization

Compound	K*i* (nM)	Specific cell surface (% IA/10^6cells)	Specific lysate (%IA/10^6 cells)
CA008	28.83 ± 3.36	n.d.	n.d.
CA009	15.28 ± 3.12	106.53 ± 2.76	27.37 ± 2.37
CA011	28.07± 2.85	n.d.	n.d.
CA012	24.26± 3.74	132.14 ± 4.29	15.63 ± 2.06

Data are mean ± SD (*n* = 3), n.d. = not determined

As shown in **Table 13**, among all compounds presented in this table, CA030 revealed the highest affinity to PSMA, followed by CA029 and CA028. CA027, which contains none of the two linkers, had the lowest affinity to PSMA.

With the exception of ^{68}Ga-CA027, the novel compounds showed higher specific internalization in C4-2 cells than the reference; *e.g.* 53.78% ID/10^6 cells for CA030 vs. 15.6% ID/10^6 cells for PSMA-617 **(Table 13)**.

Table 13: PSMA inhibition potencies (Ki values) and Specific Internalization Values

Compound	K_i (nM)	Specific cell surface (%IA/10^{6}cells)	Specific lysate (%IA/10^6 cells)
CA027	33.82 ± 2.13	2.18 ± 0.50	1.70 ± 0.24
CA028	15.17 ± 6.11	94.12 ± 2.70	41.22 ± 2.72
CA029	11.04 ± 4.87	46.83 ± 3.07	44.26 ± 3.96
CA030	4.79 ± 1.31	43.46 ± 1.50	53.78 ± 5.45
PSMA-617	2.34 ± 2.94	45.18 ± 3.61	15.55 ± 3.07

Data are mean ± SD *(n* = 3)

3.5. *In vivo* Characterization of the copper radiolabeled compound

The *in vivo* stability of the copper radiolabeled compounds was assessed by ITLC and HPLC after a PET imaging **(Figure 38)** and blood harvested 10 min post injection.

ITLC analysis of the blood stability demonstrated that ^{64}Cu-CA003 undergo 3% of ^{64}Cu dissociation or 97 ± 2.3% of the intact tracer. Radio HPLC chromatograms likewise ^{64}Cu-CA003 (**Figure 36**) of the blood sample demonstrated the activity elutes at retention time of intact tracer which confirms the integrity of the copper complex. *In vivo* fate of ^{64}Cu-chloride or ^{64}Cu-CA003 studies was conducted and PET imaging of ^{64}Cu-chloride and ^{64}Cu-CA003 showed different pharmacokinetics **(**Figure 38**)**. Maximum intensity projection PET imaging of ^{64}Cu-chloride indicated lower blood circulation (1.3), high liver (2.7) and kidney uptake (3.4), whereas ^{64}Cu-CA003 demonstrated longer blood circulation (2.3), higher kidney (5.7) uptake and lower liver accumulation (1.0) than ^{64}Cu-chloride **(**Figure 38**)**. The integrity of the ^{64}Cu-CA003 was proven by radio HPLC chromatograms of tissue extracts of kidney, blood and liver tissue **(Figure 36)**. The chromatogram for ^{64}Cu-CA003 showed a different retention time of the tracer than free copper, ^{64}Cu-chloride **(Figure 37)**.

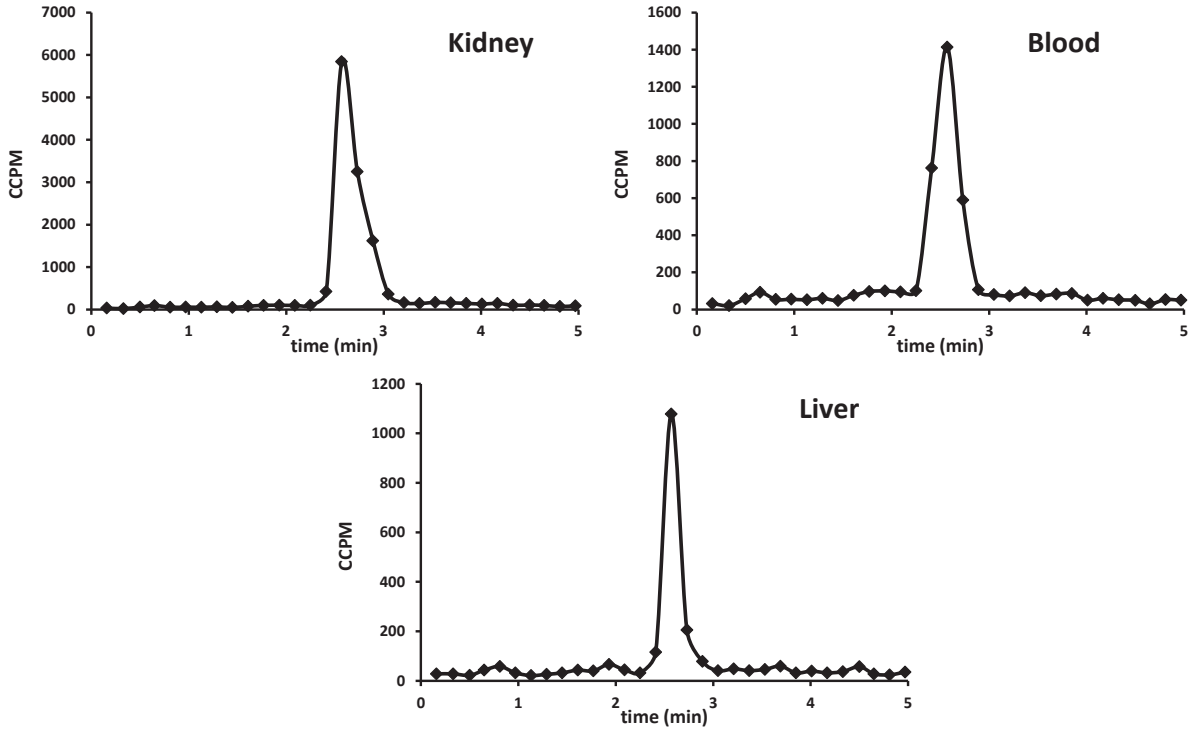

Figure 36: *In vivo* metabolite analysis of ^{64}Cu-CA003 in a BALB/c nude mouse (no tumor) at 10 min *p.i.* Radio-HPLC chromatograms of extracts from the kidney, the blood and the liver show that the activity elutes at the retention time of the intact tracer. This proves the integrity of the copper complex within the main distribution period.

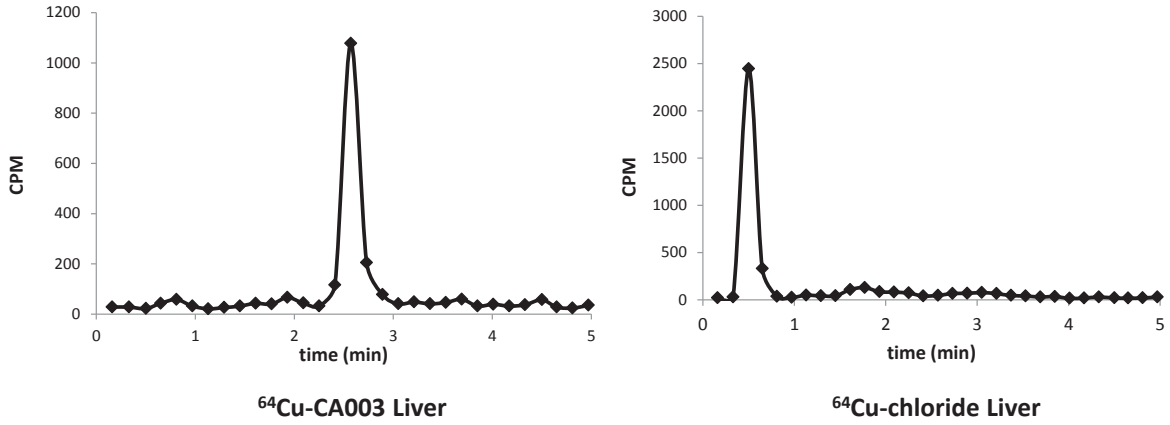

Figure 37: Radio-HPLC chromatograms of extracts of ^{64}Cu-CA003 in liver in comparison with of ^{64}Cu-chloride in the liver in a BALB/c nude mouse (no tumor) at 10 min p.i.

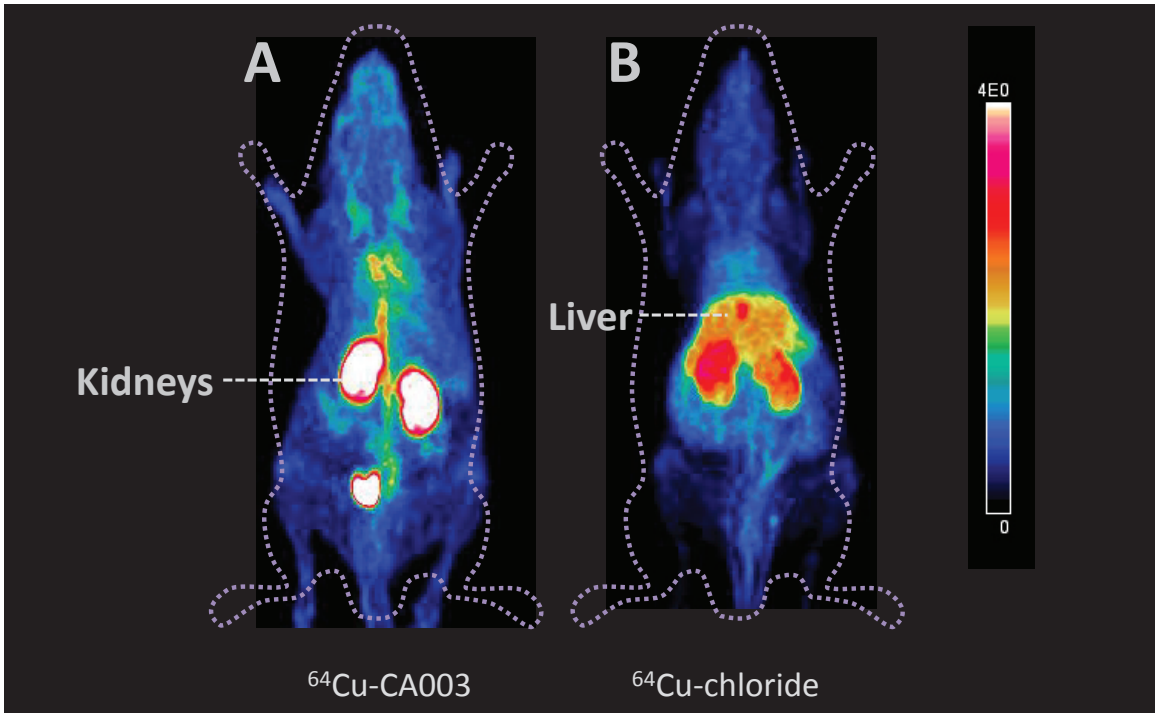

Figure 38: (A) PET image of 9 MBq (0.30 nmol) ^{64}Cu-CA003 10 min post injection in a female Swiss mouse. The maximum intensity projection (MIP) illustrates circulation in the blood and renal uptake. (B) PET image of a female Swiss mouse at 10 min p.i. of 10 MBq ^{64}Cu 10 min post injection. The maximum intensity projection (MIP) illustrates a strong uptake in the liver and the kidneys.

3.6. Small-Animal PET Imaging

3.6.1. PET Imaging of the copper radiolabeled compounds

PET scans of the radiolabeled ^{64}Cu ligands showed high tumor uptake and thus are consistent with the obtained result of binding affinity for PSMA and for internalization assay in PSMA positive cell line, C4-2 (**Figure 39**). Although the tracers, ^{64}Cu-CA002, ^{64}Cu-CA004, ^{64}Cu-CA023 and ^{64}Cu-CA025 revealed high tumoral uptake, the ^{64}Cu-CA003 demonstrated the highest tumor to background ratio and then chosen for further studies. The tracer ^{64}Cu-CA022 showed high liver uptake, this result was not expected. As expected ^{64}Cu-PSMA-617 used as reference demonstrated high liver uptake.

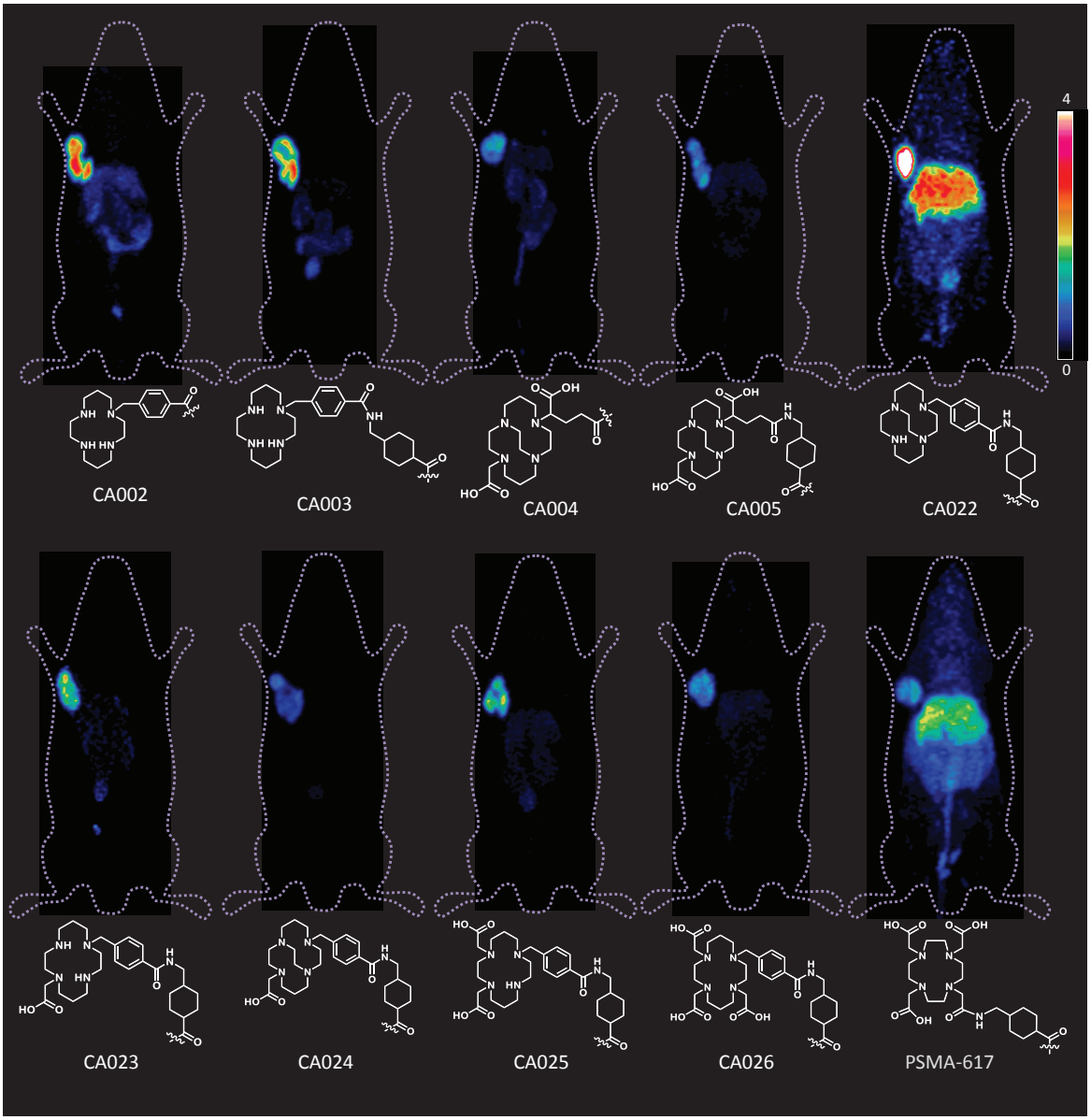

Figure 39: Whole-body small-animal PET scans as maximum intensity projections of ^{64}Cu-labelled compounds in BALB/c nu/nu C4-2 tumor bearing mice 24 h post injection via a tail vein. Tumor-targeting efficacy and pharmacokinetic properties were evaluated by injection of 0.2 nmol (approximately 10 MBq, 100 µL - as injected volume of 0.9% saline) of the labeled compounds. The color bar gives a link between the SUV and the color scale of the PET image with 0 = minimum and 4 = maximum.

Time activity curves generated from the dynamic PET imaging data, expressed as mean standardized uptake value, illustrated a tumor-to-muscle ratio of 10.5 and 3.0 for tumor-to-blood at 1 h post injection (**Figure 40**) for the tracer ^{64}Cu-CA003. PET imaging confirmed the strong accumulation of the ^{64}Cu-CA003 in the tumor, additionally showed high *in vivo* stability in comparison with other synthesized compounds for copper radioisotope. ^{64}Cu-PSMA-617 showed high accumulation in the liver, which denotes high instability *in vivo* (**Figure 41**). At 1 h post injection, the amount of radioactivity in the

background organ such as kidneys decreased whereas the tumor-to-background ratio increased. 24 h after injection, the PET scans demonstrated a very high tumor uptake, confirming the enrichment in the tumor (**Figure 41**). The high tumor accumulation was retained at later time points, i.e. at 24 h post injection.

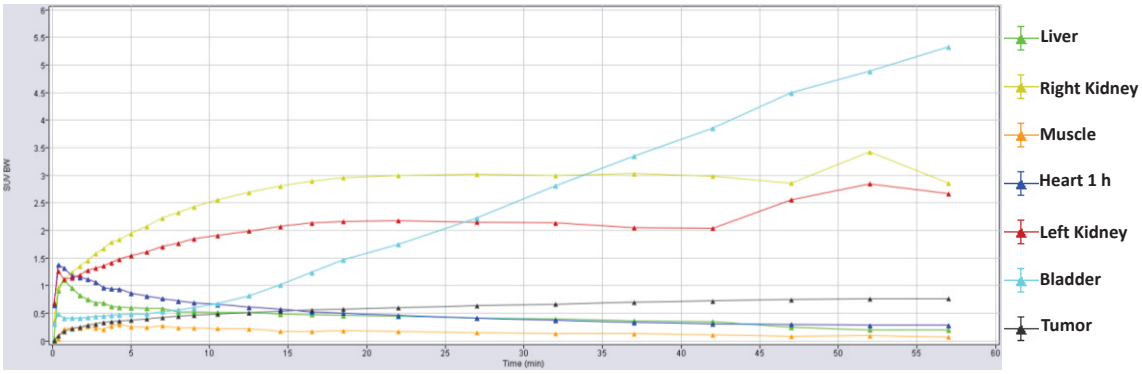

Figure 40: Time-activity curves for tumor and relevant organs up to 1 h post injection of 0.2 nmol (100 µL -as injected volume of 0.9% saline) of ^{64}Cu-CA003 in a BALB/c nu/nu mouse bearing a C4-2 tumor xenograft. Data are mean standardized uptake value based on body weight-values (SUVBW).

In order to prove the *in vivo* stability of the copper complexes of PSMA-CA003, ^{64}Cu-PSMA-CA003 was compared to ^{64}Cu-PSMA-617 as well as to ^{64}Cu-chloride (**Figure 41**). The pharmacokinetic characteristics of the compound were assessed in a small animal PET study in a C4-2 tumor xenograft. The results are shown in **Figure 41**. The time activity curves obtained from the dynamic PET for ^{64}Cu-CA003 showed a high tumor-to-liver ratio (4.0) at 1 h after injection, whereas for ^{64}Cu-PSMA-617 the tumor-to-liver ratio was 0.37. In order to prove the *in vivo* integrity of ^{64}Cu-CA003 in the tumor ^{64}Cu-chloride was injected in further C4-2 tumor bearing mice. PET imaging of both compounds was performed. After the PET imaging the organs were extracted**,** Figure 38 homogenized and analyzed by HPLC. The chromatogram results of the analysis of both compounds were compared **Figure 36** and **Figure 37**.

The pharmacokinetic effect observed for ^{64}Cu-chloride is different than that of ^{64}Cu-CA003. PET imaging of ^{64}Cu-chloride at maximum-intensity projections reveals an increasing tumor uptake up to 2 h after injection. In contrast to ^{64}Cu-CA003, ^{64}Cu-chloride showed a very high liver accumulation (**Figure 41**). The tumor-to-liver ratio at 2 h for ^{64}Cu-chloride was 0.38, whereas the tumor-to-liver ratio of ^{64}Cu-CA003 was 6.3.

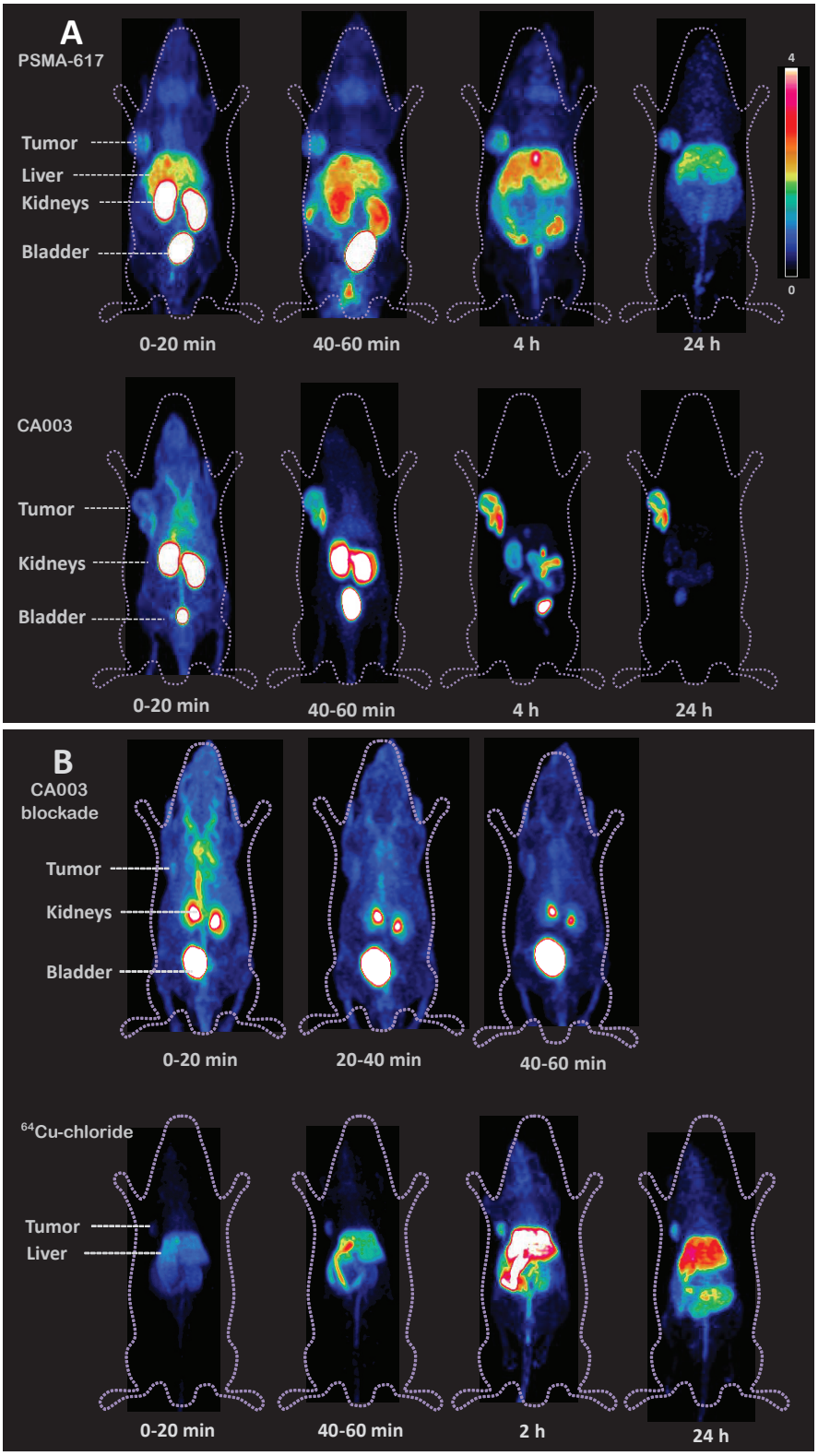

Figure 41: (A) Whole-body small-animal PET scans as maximum-intensity projections of BALB/c *nu/nu* mice bearing C4-2 tumor xenografts. PET imaging of ^{64}Cu-PSMA-617 (10 MBq, 0.2 nmol), ^{64}Cu-PSMA-CA003 (10 MBq, 0.2 nmol), (B): ^{64}Cu-PSMA-CA003 (5 MBq, 0.030 nmol) co-injected with an excess amount of non-labeled PSMA-617 (2 mg per kilogram of body weight) and ^{64}Cu-chloride (10 MBq). The color bar gives a link between the SUV and the color scale of the PET image with 0 = minimum and 4 = maximum.

To prove the specific binding of the best-performing compound, ^{64}Cu-CA003, the blockade experiment was performed **Figure 41B,** which was confirmed the specific binding of this tracer.

The result generated from SUV_{mean} of the PET Imaging of ^{64}Cu-CA003 and ^{64}Cu-PSMA-617 used as reference are expressed in **Figure 42**, emphasized the high tumoral uptake and low liver uptake in comparison with ^{64}Cu-PSMA-617, which showed lower tumor uptake and high liver uptake.

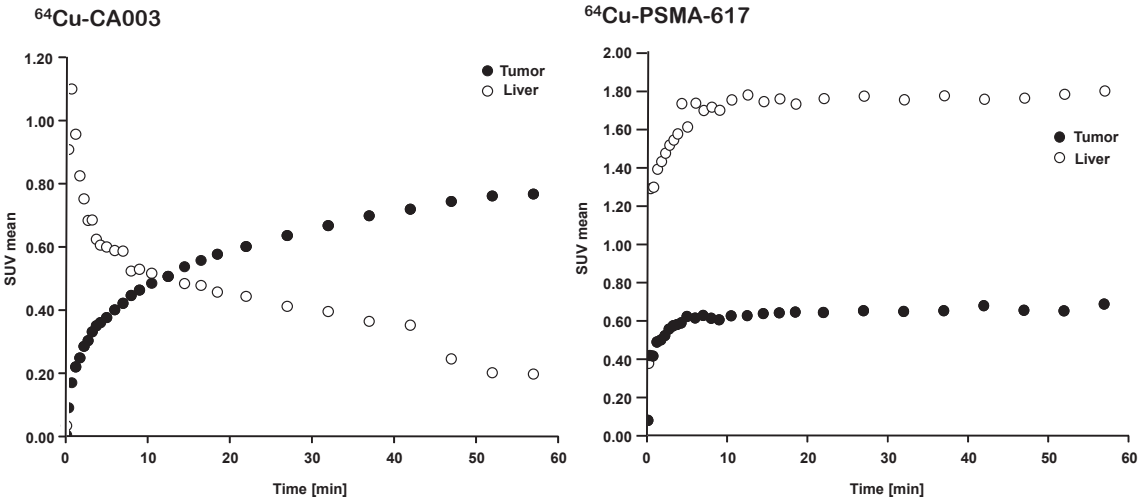

Figure 42: Time-activity curves of tumor and liver tissue for ^{64}Cu-CA003 (10 MBq, 0.2 nmol) and ^{64}Cu-PSMA-617 (10 MBq, 0.2 nmol) in BALB/c nu/nu mice bearing C4-2 tumor xenografts up to 1 h post injection. Data are mean standardized uptake values (SUVmean).

3.6.2. Planar Scintigraphic Imaging

The compounds CA008 and CA011 presented high inhibition potency. However, these compounds showed poor internalization ratio *in vitro* after radiolabeling with ^{203}Pb. In line with the result of the internalization assay, both ^{203}Pb-CA008 and ^{203}Pb-CA011 demonstrated low tumor uptake in tumor-bearing mice. ^{203}Pb-CA009 and ^{203}Pb-CA012 presented high tumor accumulation (**Figure 43)**. ^{203}Pb-CA012 was chose for clinical translation, once it had demonstrated a fast kidney clearance (**Figure 44**).

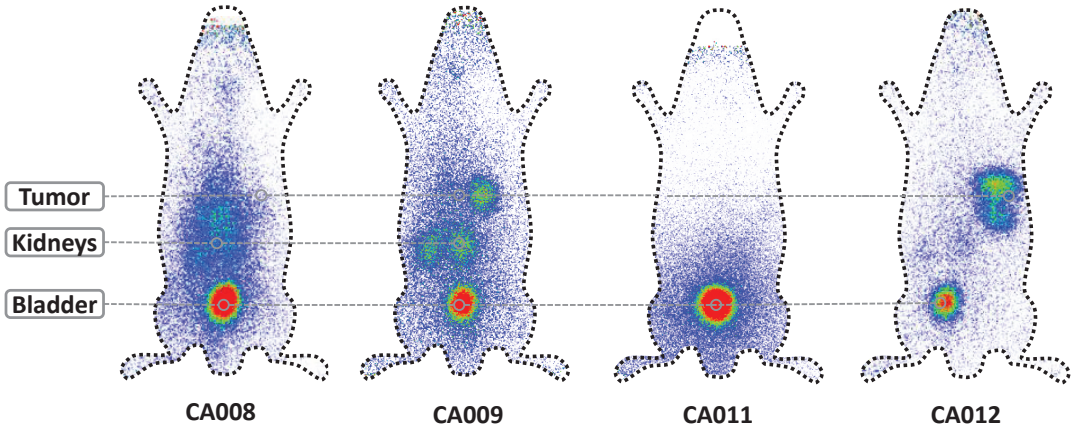

Figure 43: ^{203}Pb-labeled compounds in C4-2 tumor bearing mice at 1 h after tail vein injection displayed with planar scintigraphic imaging.

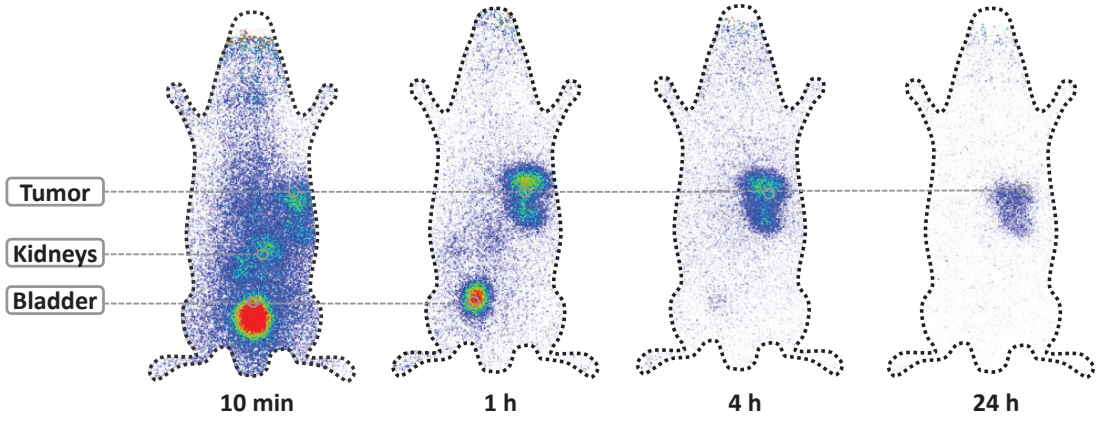

Figure 44: ^{203}Pb-CA012 in C4-2 tumor bearing mouse at different times displayed with planar scintigraphic imaging.

3.6.3. PET Imaging of the PSMA-617 derivatives compounds

The time-activity curves and the mean SUV body weight values generated from the dynamic PET imaging of ^{68}Ga-CA028 1 h *p.i.* demonstrated a tumor-to-kidney ratio of 2.08 **(Figure S1)**. At 2 h *p.i.*, this ratio was increased to 2.69 (**Figure 45**), while the ligands ^{68}Ga-CA029 and ^{68}Ga-CA030 showed lower tumor-to-kidneys ratios of 0.52 and 0.33 respectively (**Figure 45**). The time-activity curves revealed a fast clearance of the tracer. ^{68}Ga-CA028 showed a high tumor accumulation and high kidney values. In contrast, for ^{68}Ga-CA027, a faster clearance by the kidney at a tumor accumulation was found (**Figure 45**). Even though ^{68}Ga-CA030 demonstrated higher kidney uptake values

than ^{68}Ga-CA028, it showed the highest tumor uptake among all compounds (**Figure 46B**). Therefore, ^{68}Ga-CA028 and ^{68}Ga-CA030 were chosen for detailed investigation.

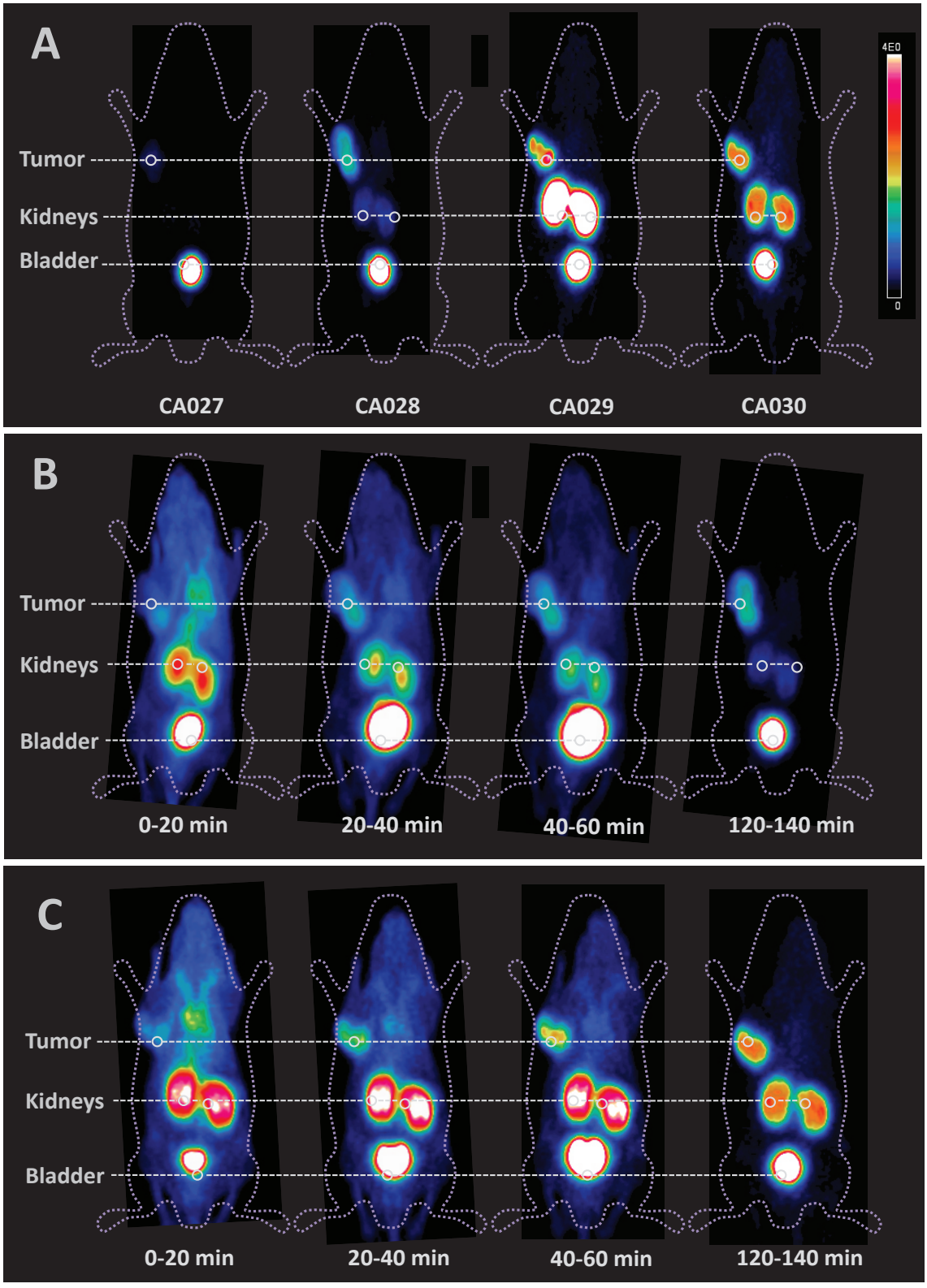

Figure 45: Comparison of whole body small animal PET scans as maximum-intensity projections of BALB/c nude mice bearing C4-2 tumor xenografts. PET imaging of the four new PSMA ligands radiolabeled with ^{68}Ga (20 MBq; 0.2 nmol) 2 h post injection (A) and the time courses of ^{68}Ga-CA028 (B) and ^{68}Ga-CA030 (C). The colour bar gives a link between the SUV and the colour scale of the PET image with 0 = minimum and 4E0 = maximum.

The small animal PET images in **Figure 45A** and **Figure 46** demonstrated a very fast kidney clearance and low tumor accumulation of ^{68}Ga-CA027. Distinctly, the radiotracers ^{68}Ga-CA028, ^{68}Ga-CA029 and ^{68}Ga-CA030 showed high tumor accumulation (**Figure 46B**). ^{68}Ga-CA029 showed the highest kidney uptake, followed by ^{68}Ga-CA030 (**Figure 46A**).

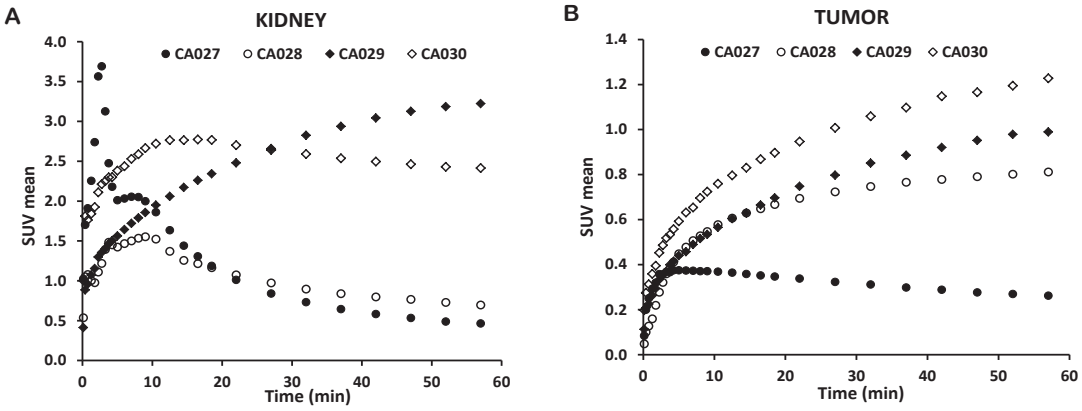

Figure 46: Time-activity curves of the novel PSMA ligands labeled with ^{68}Gafor kidney (A) and for the tumor (B) up to 1 h post injection. Data are mean standardized uptake values (SUV).

3.7. Biodistribution Studies

3.7.1. Biodistribution of ^{64}Cu-CA003

The results obtained for the biodistribution of the promising PSMA ligand ^{64}Cu-CA003 (n = 3) are shown **Figure 47** The graphs showed the organ distribution at the time points 10 min, 1 h, 4 h, 24 h and 72 h after injection. 10 min after injection 11.33 ± 4.11%ID/g tumor uptake was observed. After 4 h the amount of the tracer accumulation (32.34 ± 10.6% ID/g) in the tumor was much higher than in the kidneys (13.33 ± 3.36% ID/g). In addition to this, in order to prove the specificity to target PSMA the experiment with simultaneous administration of PSMA-617 to block PSMA binding at 1 h (n = 3) is represented **Figure 47B**. Co-injection of non labelled PSMA-617 [2 mg/kg] led to a strong decrease of the accumulation of 64Cu-CA003 in C4-2 tumors (30.83 ± 12.61% ID/g to 2.35 ± 0.38% ID/g) and in the kidneys (67.04 ± 20.89% ID/g to 3.47 ± 0.48% ID/g) at 1 h post injection.

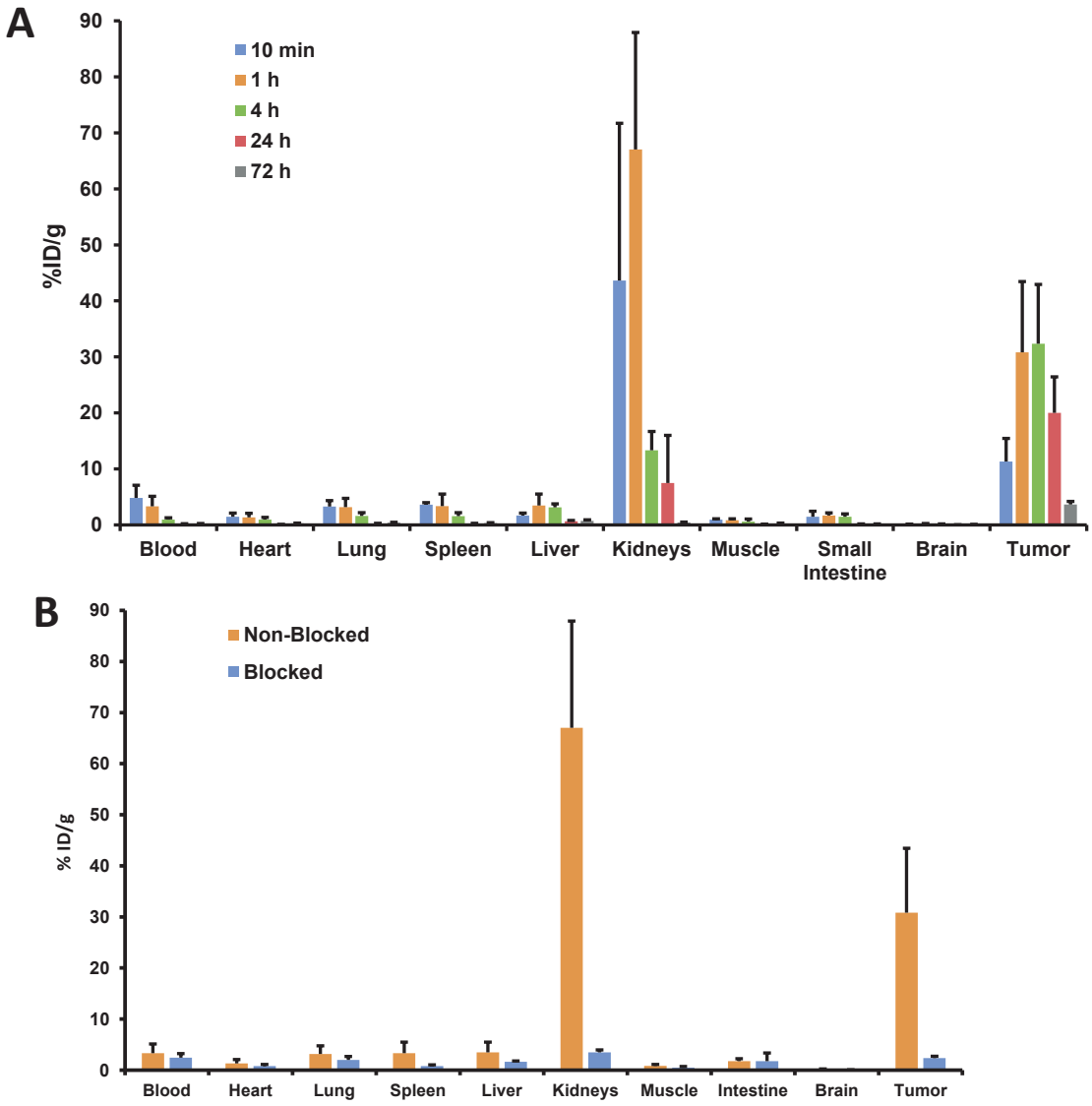

Figure 47: Organ distribution of 0.025 nmol of ^{64}Cu-CA003 at the time points: 10 min, 1 h, 4 h, 24 h and 72 h after injection (A). Values are expressed the range of % ID/g of tissue ± standard deviation; n = 3 for all tissues. In a blockade experiment (B), the radiotracer ^{64}Cu-CA003 (0.030 nmol) was injected at the same time as 2 mg of PSMA-617 per kilogram of body weight.

3.7.2. Biodistribution of ^{203}Pb-CA012

The results obtained for the biodistribution of the promising PSMA ligand ^{203}Pb-CA012 (n = 3) are shown in **Table 14**. The table showed the organ distribution at the time points 10 min, 1 h, 4 h and 24 h after injection. The ^{203}Pb-CA012 ligand demonstrated a faster kidney clearance and high tumoral uptake to background. This data elucidate the choosing of this compound for clinical translation (**Figure 51**).

Table 14: Organ distribution of ^{203}Pb-CA012 in tumor bearing mice

Tissue	10 min	1 h	4 h	24 h
Blood	5.37 ± 1.95	0.26 ± 0.10	0.05 ± 0.01	0.03 ± 0.00
Heart	1.78 ± 0.66	0.10 ± 0.03	0.04 ± 0.02	0.02 ± 0.00
Lung	4.31 ± 1.19	0.33 ± 0.13	0.10 ±0.03	0.05 ± 0.01
Spleen	1.97 ± 1.07	0.16 ± 0.08	0.07 ± 0.01	0.07 ± 0.02
Liver	1.25 ± 0.43	0.20 ± 0.10	0.09 ± 0.01	0.10 ± 0.02
Kidneys	26.97 ± 8.74	5.08 ± 2.45	1.61 ± 0.28	0.89 ± 0.14
Muscle	1.20 ± 0.43	0.05 ± 0.03	0.06 ± 0.03	0.02 ± 0.00
Small intestine	1.75 ± 0.48	0.10 ± 0.04	0.07 ± 0.05	0.02 ± 0.00
Brain	0.14 ± 0.04	0.02 ± 0.00	0.02 ± 0.01	0.01 ± 0.00
Tumor	12.33 ± 1.92	8.37 ± 3.67	7.81 ±0.86	3.30 ± 1.60

Organ distribution of 0.025 nmol of ^{203}Pb-CA012. Values are expressed in % ID/g of tissue ± standard deviation; *n* = 3 for all tissues.

3.7.3. Biodistribution of PSMA-617 derivatives ^{68}Ga-CA028 and ^{68}Ga-CA030

The results obtained for the biodistribution of the promising PSMA ligands ^{68}Ga-CA028 (**Figure 48**) and ^{68}Ga-CA030 (**Table 15)** are in line with the PET imaging. The graphics (**Figure 48** and **Table 15)** showed the organ distribution at the time points 20 min, 1 h, 2 h and 4 h *p.i.*. For ^{68}Ga-CA028 a tumor uptake of 12.53 ± 0.45 %ID/g 20 min after injection was observed. At 1 h *p.i.*, the amount of the tracer accumulation in the tumor was higher than in the kidneys.

For ^{68}Ga-CA030 a tumor uptake of 5.17 ± 1.48 %ID/g 20 min after injection was observed. At 1 h *p.i.*, in contrast with ^{68}Ga-CA028, the amount of the tracer accumulation in the kidney was higher.

The specificity of the binding to PSMA was proven with a blockade experiment: co-injection of non-labeled PSMA-617 [2 mg/kg] led to a strong decrease of accumulated ^{68}Ga-CA028 in C4-2 tumors (34.46 ± 9.76 %ID/g to 1.31 ± 0.34 %ID/g) and in the kidneys (15.58 ± 2.79 %ID/g to 2.37 ± 0.52 %ID/g) 1 h *p.i.* (**Figure 49**).

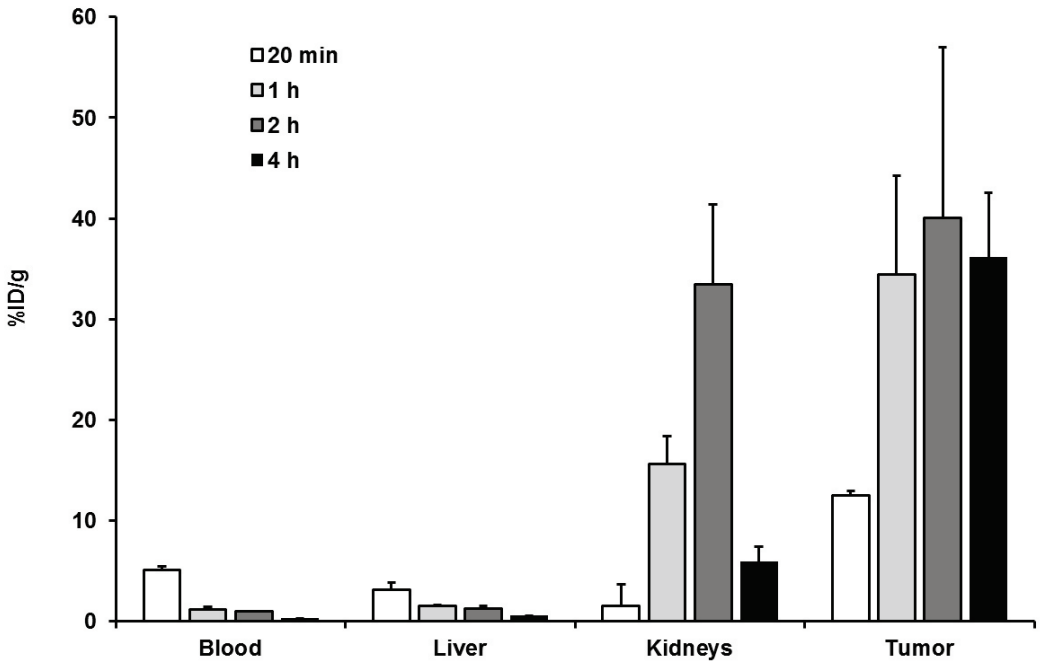

***Figure 48**: Organ distribution of ^{68}Ga-CA028 (0.05 nmol, 20 MBq) expressed as % ID/g of tissue ± SD (n = 3) at 20 min, 1 h, 2 h and 4 h post injection.*

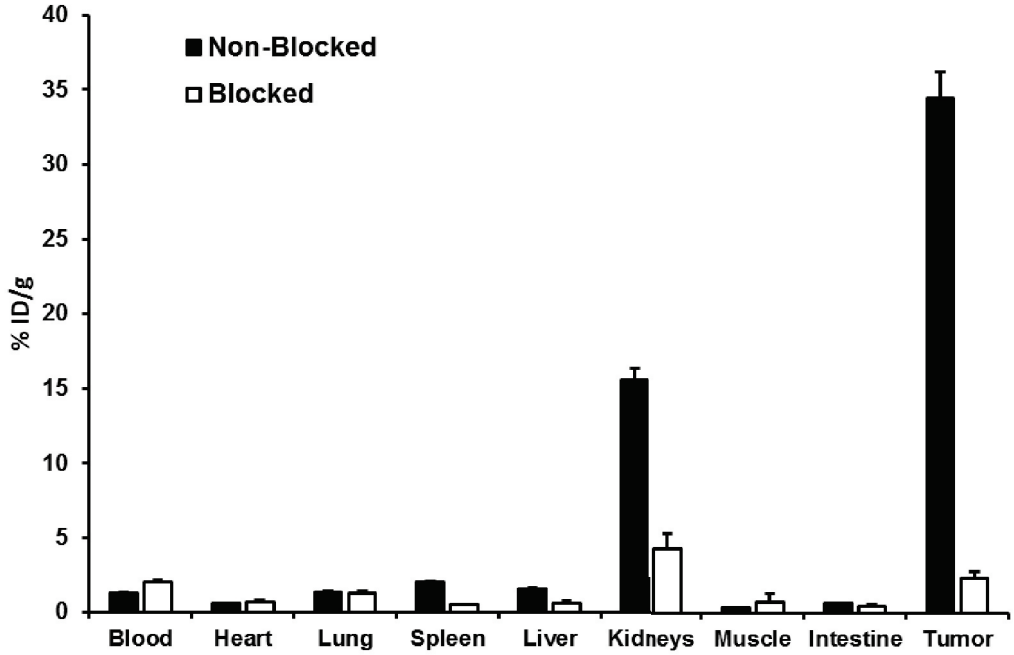

Figure 49: Blockade experiment with ^{68}Ga-CA028 (0.05 nmol, 20 MBq) 1 h post injection. 2 mg of PSMA-617 per kilogram of body weight was injected at the same time as ^{68}Ga-CA028. Data are mean expressed (n = 4)

Table 15: Organ distribution for ^{68}Ga-PSMA-CA030 in tumor bearing mice

Tissue	20 min	1 h	2 h	4 h
Blood	4.33 ± 0.51	3.59 ± 1.52	1.42 ± 0.61	0.39 ± 0.14
Heart	1.29 ± 0.30	1.03 ± 0.36	0.40 ± 0.09	0.16 ± 0.05
Lung	2.63 ± 0.89	2.74 ± 0.72	1.08 ± 0.42	0.34 ± 0.10
Spleen	8.37 ± 0.47	2.86 ± 1.86	1.39 ± 0.47	0.48 ± 0.09
Liver	1.04 ± 0.18	1.52 ± 0.61	0.81 ± 0.15	0.50 ± 0.14
Kidneys	63.89 ± 5.72	46.39 ± 23.44	20.19 ± 7.92	6.17 ± 0.82
Muscle	1.39 ± 1.30	0.63 ± 0.21	0.28 ± 0.03	0.17 ± 0.02
Small intestine	1.00 ± 0.38	0.92 ± 0.37	0.75 ± 0.06	0.21 ± 0.09
Brain	0.08 ± 0.01	0.08 ± 0.02	0.04 ± 0.02	0.01 ± 0.00
Tumor	5.17 ± 1.48	5.36 ± 2.21	4.31 ± 0.30	2.69 ± 0.88

Organ distribution [^{68}Ga]-PSMA CA030 at the time points: 10 min, 1 h, 4 h after injection. Values are expressed in % ID/g of tissue ± standard deviation; n = 3 for all tissues.

3.8. Biodistribution Studies in Human

3.8.1. PET Imaging of ^{64}Cu-CA003 in a Human

In order to show the clinical applicability of ^{64}Cu-CA003, a PET scan in the first patient with a high serum PSA value (185 ng/mL; normal range < 4 ng/mL) and LDH (861 U/l; normal range < 342) was performed. The resulting PET image is presented in **Figure 50**. It shows that the tumor uptake of the PSMA ligand is higher in the tumor than in several commonly used reference tissues such as liver and salivary glands.

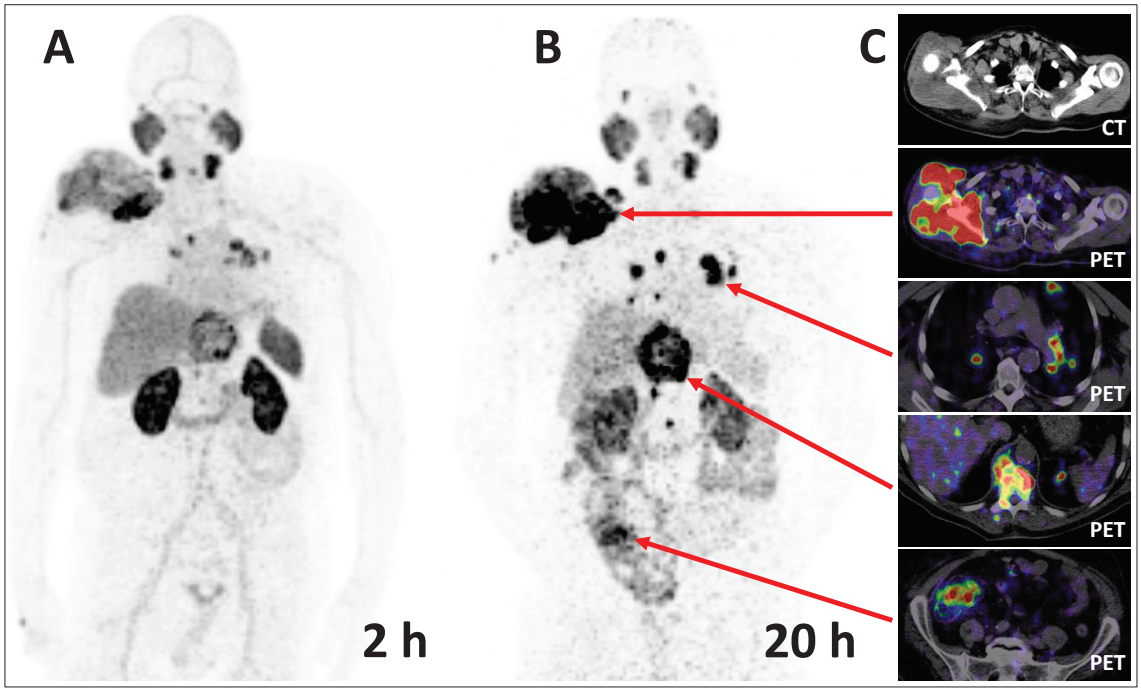

Figure 50: ^{64}Cu-CA003 (200 MBq, 0.5 nmol) PET/CT maximum intensity projections of a patient at 2 h (A) and 20 h post injection (B). Red arrows point to selected right shoulder soft-tissue infiltration from scapula origin, lung, bone and lymph-node metastases increased in contrast over time. The hepatobiliary clearance causes hot-spots inside the intestine in delayed imaging; cross-sectional slices (C) are mandatory to avoid false-positive readings.

The obtained SUV values were in comparison to literature values for PSMA-617 (272) , the current standard of reference for theranostic PSMA-ligands, and are presented in Table 16. Due to the acquisition with standard scanner settings calibrated for pure positron emitters such as ^{18}F, the additional gamma lines emitted by ^{64}Cu presumably increase the number of “random coincidences,” thus systematically and quantitatively over-estimating SUVs. However, in the early image time-point at 2 h p.i., the SUV-ratios between CA003 and PSMA-617 are almost equal for both tumor lesions and reference tissues, indicating that the diagnostic performance regarding tumor delineation may be very similar at day-1 examinations. As reflected by the values obtained with ^{64}Cu-CA003 at 2 h versus 20 h post-injection, unspecific uptake in normal organs is characterized by a strong washout. In contrast, tumor values reveal a relatively stable accumulation of the radiopharmaceutical and delayed images - that can be obtained with ^{64}Cu having a 12.7 h half-life but not with 1 h half-life of ^{68}Ga – and may further improve tumor-delineation. Rapid non-tumor clearance is also an excellent prerequisite for potential therapeutic application. However, hepatobiliary clearance can cause some activity hotspots inside the intestine in later imaging, requiring more thorough reading to distinguish these from peritoneal/mesenteric lymph nodes.

Table 16: Safety Dosimetry estimate of Diagnostic ^{64}Cu-CA003 (left column) and ^{68}Ga-PSMA-617 Afshar-Oromieh *et al*., 2015 *(93)* (Right Column) Based on a Male-Adult Phantom in OLINDA.

Organ	^{64}Cu-CA003		^{68}Ga-PSMA-617	
	SUV mean after 2 h	SUV mean after 20 h	SUV mean after 1 h	SUV mean after 3 h
Lacrimal gland	9.9	4.1	4.9	5.9
Nasal mucosa	4.5	2.3	2.9	3.4
Parotid gland	15.4	5.1	10.4	13.1
Submandibular gland	19.9	4.4	10	12.4
Sublingual gland	11.2	2.6	4.6	4.0
Blood pool, mediastinal	3.6	0.4	2.5	2.4
Liver	6.0	0.8	3.3	2.7
Spleen	10.6	0.7	4.3	3.5
Prox. Small intestine	12.3	2.4	4.7	5.5
Colon	4.6	2.9	3.5	4.0
Kidneys	19.0	4.9	15.6	17.0
Gluteal muscle	0.6	0.1	0.7	0.7
Bone metastases	24.2	15.7	9.4	6.27
Lymph node	16.8	11.3	7.1	13.54

3.8.2. Geometric mean Imaging of ^{64}Pb-CA012 in a Human

It is prove that an injected activity of 258-310 MBq, the 279 keV gamma rays emitted from ^{203}Pb with an 80% abundance is probability sufficient for planar scans (**Figure 51**). In comparison to a ^{177}Lu-PSMA-617 therapeutic approach with 7400 MBq and emission of 210 keV gamma rays with 11% abundance probability (**Figure 51B**), the count-rate was 3 times lower, and patients could not tolerate the usually necessary time for single-photon-emission-computed-tomography.

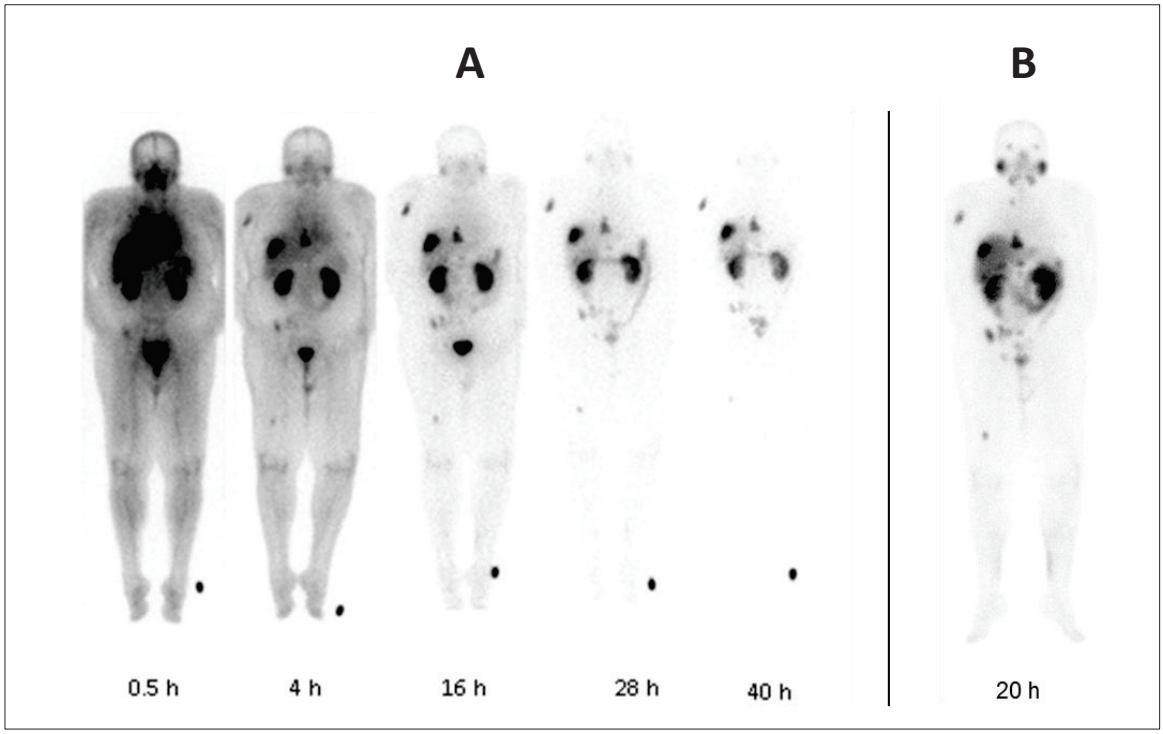

Figure 51: Geometric mean images of ^{203}Pb-CA012 planar scans over time (A) in comparison to a treatment scan with ^{177}Lu-PSMA-617 (B); both acquired with a Medium Energy collimator.

The dosimetry for diagnostic ^{203}Pb-CA012 was estimated and is presented in the left column of **Table 18.** All organ absorbed doses are dominated by photons (primary emission at 279 keV), low probability emissions in sum contribute <10% in all organs, respectively. A typical clinical examination with 250-300 MBq, e.g. for individual dosimetry prediction, translates into a radiation burden of 6.0-7.5 mSv.

In the decay from ^{212}Pb to stable ^{208}Pb, regardless whether by the Polonium or Thallium branch, two beta- and one alpha-particle are emitted per atom (**Figure 16**). The safety dosimetry estimate for therapeutic ^{212}Pb-CA012, taking into account the complete succeeding decay chain, is presented on the right column of **Table 18**.

Table 17: Safety Dosimetry estimate of diagnostic ^{203}Pb-CA012 (left column) and therapeutic ^{212}Pb-CA012 (right column) based on the male-adult phantom in OLINDA.

Organ	^{203}Pb-CA012		^{212}Pb-CA012	
	Equivalent Dose mSv / 100 MBq	Standard Deviation (mSv)	Equivalent Dose mSv / 100 Mbq	Standard Deviation (mSv)
Adrenals	2.84	0.06	193.12	6.34
Brain	1.16	0.13	189.97	6.50
Breasts	1.06	0.07	189.98	6.43
Gallbladder	2.79	0.22	192.92	5.98
LLI	1.95	0.20	191.34	6.57
Small intestine	2.09	0.13	191.79	6.53
Stomach	2.04	0.07	191.80	6.46
ULI	2.07	0.10	191.76	6.49
Heart	1.80	0.06	191.32	6.36
Kidneys	18.05	0.78	4906.57	194.54
Liver	4.30	1.32	703.27	300.41
Lungs	1.60	0.05	190.85	6.37
Muscle	1.50	0.11	190.70	6.53
Pancreas	2.78	0.03	192.93	6.27
Red marrow	1.82	0.13	615.11	115.64
Osteogenic cells	3.67	0.33	3796.37	573.43
Skin	0.99	0.08	189.81	6.46
Spleen	6.73	0.38	1606.73	206.76
Testes	1.40	0.16	190.43	6.59
Thymus	1.44	0.12	190.68	6.54
Thyroid	1.39	0.15	190.54	6.58
Urinary bladder	6.73	0.83	200.21	8.58
Total body	1.71	0.07	237.77	0.67
Eff.Dose Equi.	3.55	0.01	748.91	17.18
Eff.Dose	2.40	0.25	415.08	13.54

The ratio between tumor dose and dose-limiting organs determines the therapeutic range of a radiopharmaceutical. The salivary glands, red-marrow and kidneys were identified by using the spherical model as dose limiting. Table 18 shows the relevant dosimetry information in comparison with ^{213}Bi and ^{225}Ac-PSMA-617(140, 283).

Table 18: Dosimetry of ^{212}Pb-CA012 for salivary glands, randomly chosen tumor lesions (sphere model) and the presumably dose-limiting organs in comparison ^{213}Bi-PSMA-617 and ^{225}Ac-PSMA-617

Nuclide (treatment activity)	Bi-213 (1 GBq)	Pb-212 (100 MBq)	Ac-225 (6 MBq)
Ligand	^{213}Bi-PSMA 617 *	^{212}Pb-CA012	^{225}Ac-PSMA-617**
Nuclide half-life (h)	0.8	**10.4**	238
	Tissue equivalent dose (Sv_{RBE5})		
Salivary Gland	8.1	**7.5**	13.8
Kidneys	8.1	**4.9**	4.2
Red Marrow	0.5	**0.6**	0.3
Tumor (mean)	7.6	**14**	34
Tumor / Salivary	0.9	**1.9**	2.5
Tumor / Kidney	0.9	**2.9**	8.1
Tumor / Red Marrow	15.2	**23.3**	113.3

* Kratochwil *et al* ., 2017*(283)*, ** Kratochwil *et al*., 2017 *(140)*

3.8.3. PET/CT of ^{68}Ga-CA028 and ^{68}Ga-CA030 in Humans

In order to prove the clinical applicability of ^{68}Ga-CA028 and ^{68}Ga-CA030, PET/CT imaging in first patients was performed. The resulting images are illustrated in **Figure 52** and **Figure 53.** The imaging with ^{68}Ga-CA028 and ^{68}Ga-CA030 confirmed the results obtained *in vitro* and in the animal models.

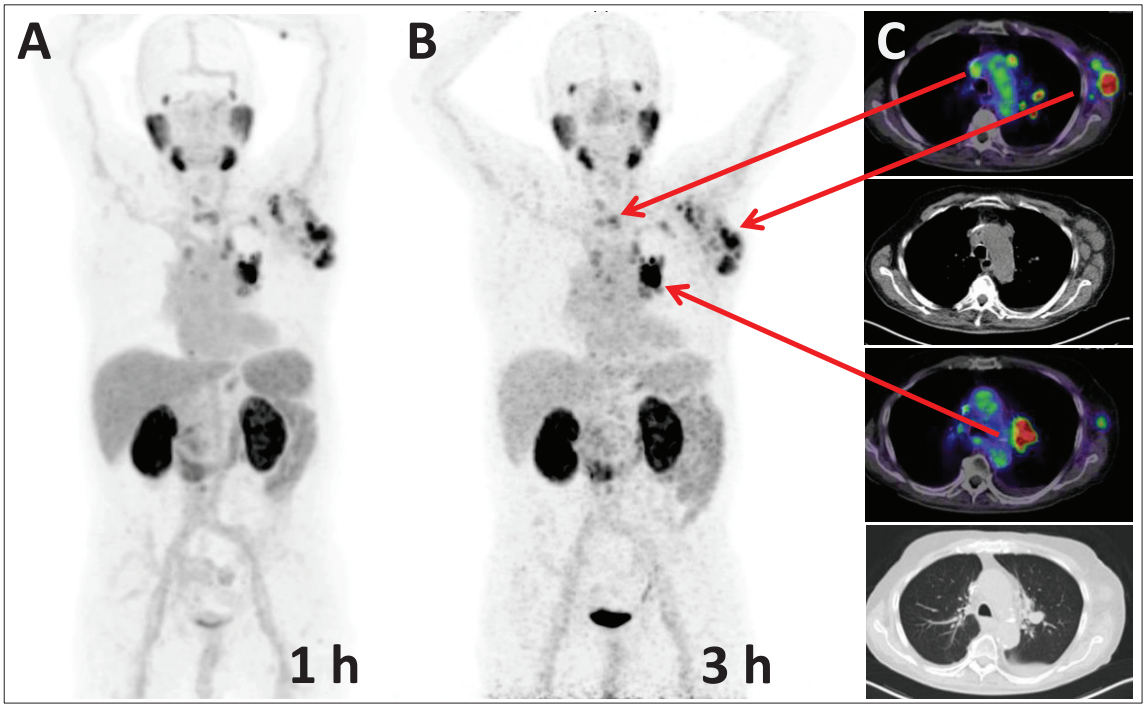

Figure 52: Maximum intensity projections of a PSMA-PET of a prostate cancer patient performed 1 h (A) and 3 h (B) post injection of 339 MBq / 20 nmol ^{68}Ga-CA028. (C) Cross-sectional slices demonstrate axillary and hilar lymph node metastases (red arrows); also delineable on the correlated CT which serves as a standard of reference.

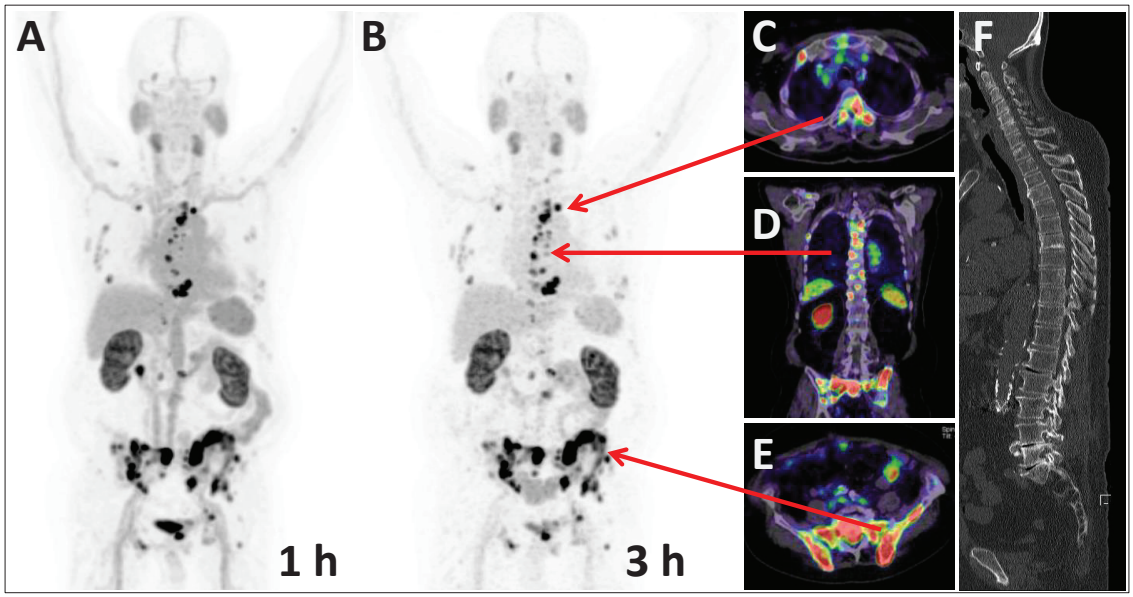

Figure 53: Maximum intensity projections of a PSMA-PET of a prostate cancer patient performed 1 h (A) and 3 h (B) post injection of 295 MBq / 20 nmol ^{68}Ga-CA030. Arrows point to the position of the cross-sectional slices demonstrating bone metastases in multiple regions of the axial skeleton (C-E). (F) In the CT, no typical osteoblastic reactions allowed tumor delineation by morphological information alone.

The PET scans and the SUVs were acquired with standard scanner settings, calibrated for pure positron emitters (23). The SUV-values obtained at 1 h versus 3 h *p.i.* are presented in **Table 19**. As reflected by these values, a high and stabile accumulation in the tumor is achieved.

Table 19: Safety dosimetry of diagnostic SUV_{mean} values of ^{68}Ga-CA028, ^{68}Ga-PSMA-617 (values from Afshar-Oromieh *et al*., 2015 *(93)*) and ^{68}Ga-CA030 and based on an adult male phantom in OLINDA.

Tissue	^{68}Ga-CA028		^{68}Ga-PSMA-617		^{68}Ga-CA030	
	1 h	3 h	1 h	3 h	1 h	3 h
Lacrimal gland	7.4	7.6	4.9	5.9	7.1	9.0
Nasal mucosa	2.9	3.5	2.9	3.4	3.3	3.8
Parotid gland	11.0	8.0	10.4	13.1	6.1	6.7
Submandibular gland	14.4	8.9	10	12.4	8.7	11.3
Sublingual gland	3.8	2.8	4.6	4.0	4.1	4.9
Blood pool, mediastinal	3.2	2.9	2.5	2.4	5.6	4.5
Liver	4.3	1.8	3.3	2.7	5.8	5.9
Spleen	5.1	2.5	4.3	3.5	7.2	6.1
Proximal small intestine	8.4	10.4	4.7	5.5	4.1	5.0
Colon	4.9	4.2	3.5	4.0	4.9	4.7
Kidneys	13.8	10.9	15.6	17.0	13.4	16.5
Gluteal muscle	0.7	0.4	0.7	0.7	0.8	0.7
Bone metastasis	4.5	4.1	9.4	6.3	27.2	37.7
Lymph node	13.5	10.7	7.1	13.5	-	-
Bone metastasis	6.9	5.7			30.9	32.6
Bone metastasis	4.6	4.4			31.0	33.1
Lymph node	17.0	25.4			-	-
Lymph node	5.0	4.1			-	-
Lung metastasis	5.7	4.7			-	-

4. DISCUSSION

4.1. Copper ligands

The main purpose of this study was to develop novel PSMA specific ligands that form stable complexes with copper radioisotopes. Among nine compounds investigated, CA003 was found to be the most promising compound. Here, we report the preclinical characterization of CA003 as well as a first application in a patient. The syntheses of the precursor molecules and their chelator derivatives were accomplished by solid phase synthesis methods. The ^{64}Cu-labeling of the PSMA ligands could be performed in quantitative yields. The urea-based binding motif Lys-NH-CO-NH-Glu has been shown to bind to PSMA with high affinity *(268, 269)* while lipophilic linkers further optimize its binding properties *(272, 284)*. In the first instance, the chelator moiety was chosen with respect to its influence on the pharmacokinetics. It has already been reported that small, non-polar substituents such as the aromatic moiety in MIP-1466 *(285)* lead to compounds with a PK that is substantially different from PSMA-617. Unmodified cyclam is a substituent that comes close to these prerequisites. Interestingly, CA003 fulfilled the expectations and was found to show extended retention in the circulation, showing characteristics of the albumin binding tracers recently described by Benešová *et al*. *(286)*. In the present study the high inhibition potency of the synthesized ligands, in particular CA003 (K_i = 1.60 ± 0.52 nM) and the high specific uptake in the PSMA positive C4-2 cells were demonstrated. Among all compounds ^{64}Cu-CA003 showed high specific internalization of 34.63 ± 2.77% IA/10^6 cells. In CA003, the chelator CTPA, which is linked via a benzyl group, leads to a hydrophilicity and net charge that provide ideal pharmacokinetic properties.

When compared to their non-cross-bridged counterparts, the *in vitro* and *in vivo* stability of the Cu (II) cross-bridged macrocycle complexes may be explained in part by differences in their coordination chemistry. The structures of the Cu (II) complexes of TETA and CB-TE2A possess differences despite their related frameworks *(229)*. Cu(II)-CB-TE2A complex has an octahedral complex with two axial nitrogens, two equatorial nitrogens, and carboxylate groups at the remaining two cis-equatorial positions as particular feature *(287)*. Cu(II)-TETA forms a distorted octahedron with two weakly coordinated axial carboxylates, while the four nitrogens of the tetraazamacrocycle are at equatorial positions *(288)*. The two complexes have different overall charges. Cu(II)-CB-TE2A forms a neutral complex, completely enveloping the Cu(II) cation, while Cu(II)-TETA has an overall -2 charge due to two free carboxylates *(229)*. The structure of the Cu(II)-DOTA complex is analogous to that of Cu(II)-TETA *(288, 289)*. However,

metabolism experiments confirmed that ^{64}Cu-DOTA underwent more transchelation to liver protein than ^{64}Cu-TETA *(229)*.

The results obtained from the serum stability experiment confirm that - besides the DOTA containing compounds e.g. PSMA-617 - all compounds show high serum stability within the observation period of 24 h. Although the compounds containing the cross bridged chelators showed slightly enhanced serum stability *(229)*, there is experimental proof that even unmodified CTPA shows high serum stability, which is in accordance to our stability examinations *(290)*. Furthermore, CTPA has previously been used for antibody labeling with copper-67 *(290)*. Considering the rapid targeting of small PSMA binding molecules, the CTPA conjugates deserved investigation.

The organ distribution results of ^{64}Cu-CA003 exhibited high tumor-to-normal tissue ratio, which increased over time thereby providing images with high contrast. Moreover, no bone uptake was observed for CA003, indicating that this agent could be applied for the detection of prostate cancer metastases which are found in bone tissue. In the pharmacokinetic investigation, both kidney and tumor uptake of ^{64}Cu-CA003 could be specifically blocked by an excess of PSMA-617. Imaging and biodistribution studies demonstrated higher *in vivo* stability for this compound even without using cross-bridge chelators. The high tumor accumulation and the kidney clearance for ^{64}Cu-CA003 were significantly improved in comparison with literature values for ^{68}Ga-PSMA-11, ^{68}Ga-PSMA-617 and ^{18}F-PSMA-1007 *(39, 43, 291)*.

PSMA is also expressed in the kidneys *(292)*. Nevertheless, we only noted high accumulation in kidney at the renal perfusion/filtration-phase soon after intravenous injection. A difference of the PSMA-specific binding in tumor lesions versus the kidneys has already been observed previously. It is discussed to result from reduced internalization of renal PSMA after binding to filamin A, glycosylation, splicing-variants and other isoforms *(293)*. As the PSMA expressed by the LNCaP xenografts represents the human form of GCP II, whereas the kidney PSMA represent the orthologue of mice it would be premature to conclude that the higher tumor-specificity of CA003 will be completely transferable to human.

In the blocking experiments high reduction in the kidney retention was observed. It has already been demonstrated that the kidney uptake of PSMA-ligands can be blocked with monosodium-glutamate *(294)*. Glutamate has no specific binding to PSMA. However, due to its structural similarity to the Glu-urea-motif of PSMA-ligands it was discussed that it could serve as a competitive blocking agent also to non-specific ion-transporters. Figures 3 and S1 show that ^{64}Cu-CA003 is excreted in urine. The bladder shows the

strongest signal after 60 min **(Figure 41A)** and in contrast to radioactivity in the kidneys which shows saturation after 20 min (**Figure 40**) radioactivity in urine increases up to 60 min. This means that ^{64}Cu-CA003 is filtered into urine in a non-PSMA specific manner and that cells in the kidney that express PSMA are not involved in the excretion. This is emphasized by the blocking experiment in **Figure 47** where loss of radioactivity by blocking PSMA leads to increased excretion of copper-labelled CA003.

Generally, high activity accumulation values in the liver are assumed to be indicative of instability of ^{64}Cu complexes *in vivo*. The high liver accumulation and retention of ^{64}Cu-PSMA-617 in comparison to ^{64}Cu-CA003, indicates significant loss of Cu from PSMA-617 as illustrated by the PET images presented in **Figure 41** and additionally by the time-activity curves of tumor and liver tissue in **Figure 40**. The assumption that free copper released from ^{64}Cu-PSMA-617 accounts for the high liver uptake is in accordance with the images published by Cai *et al. (295)*. As ^{64}Cu-chloride can also accumulate in PCa lesions, it is worth mentioning that $^{64}CuCl_2$ can be used as PET tracer to detected prostate cancer *(296)*. More recently, Piccardo *et al. (297)* reported that $^{64}CuCl_2$ is more suitable than ^{18}F-choline for exploring the pelvis and prostatic bed. However, in both studies the liver is the critical organ.

^{64}Cu-CA003 showed, compared to ^{64}Cu-CC34 which contains a NODAGA chelator, longer blood retention, significantly lower kidney uptake and a higher tumor to background ratio. Both compounds showed low liver uptake, however ^{64}Cu-CC34 demonstrates higher spleen uptake than ^{64}Cu-CA003 *(222)*. The ^{64}Cu labeled phosphoramidate based PSMA inhibitor, ABN-1 *(298)* accumulates mainly in the kidneys. In addition, a substantial amount of ^{64}Cu-ABN-1 amount found in the liver, leading to lower tumor to background ratios when compared to ^{64}Cu-CA003. It is important to underline that the high liver uptake can be associated to transchelation and enzymatic degradation by liver enzymes. Earlier PET studies showed ^{64}Cu NODAGA-PSMA to be a promising imaging tool to detect of residual disease in patients with recurrent or primary progressive prostate cancer *(299)*.

A general comparison of all chelators utilized in this study is relatively complex. The number and organization of pendant arms utilize both the macrocyclic and chelate effects to enhance the stability. Increase of the number of pendants does not necessarily cause higher stability. In addition, other factors such as the pendant arm length also contribute to the stability *(300)*. When comparing non-bridged and bridged cyclam complexes, in some cases non-bridged cyclam complexes (log K = 27.1) have values that are similar to those of bridged cyclam complexes (log K = 27.1) *(301)*. Moreover,

greater geometrical constraint incorporated into the macrocyclic ligand enhances the kinetic inertness and thermodynamic stability of copper complexes. Our results suggest that the high kinetic inertness of Cu(II) against decomplexation to (proton-assisted as well as transchelation or transmetallation) might be, thus, more significant than thermodynamic stability *in vivo*.

The instability of ^{64}Cu-PSMA-617 *in vivo* is indicated by the release of poorly coordinated ^{64}Cu into the blood *(302, 303)* or binding to ceruloplasmin *(304)*, or to metallothionein and/or superoxide dismutase (SOD) in the liver *(228, 274, 305)*.

The PET-scan of the first patient examined with ^{64}Cu-CA003 demonstrated high tumor accumulation at low background values, comparable to ^{68}Ga-PSMA-617. Thus, it could be explicitly demonstrated that the new ligands are promising agents to target PSMA positive prostate tumors.

The main goal of the first part of this thesis is the development of therapeutic tracers that permit the protection of the non-target organs – the internalization experiments and the binding affinities were considered as the main first decision criteria. The final decision to focus the studies on ^{64}Cu-CA003 was made on the basis of the interplay of properties of the whole broad series of experiments described, in particular the PET imaging and the distribution in the mouse models. As its relative long half-life provides relevant benefit for shipment and dosimetry studies, ^{64}Cu-labeled ligands might have a “theranostic” future in combination with the short-range beta-emitter ^{67}Cu. It is important to emphasize that one of most relevant characteristics of ^{64}Cu is its low positron energy (653 keV), comparable to that of ^{18}F (633 keV), leading to a similar degree of PET image blurring as ^{18}F, which is much less than that of most other PET radionuclides. The reason for the image blurring is the relatively high E_{max} of 580 keV and the high β^- and EC branching amount of 34% and 44%, which also cause increased radiation exposure *(306)*. However the accessibility of ^{64}Cu is still limited resulting in high costs (also caused by the fact that hospitalization of the patients is mandatory). However, despite these facts, ^{64}Cu represents a valuable alternative to ^{18}F whose long distance shipment is not feasible and offers an advantage for ligands with longer circulating times to achieve good tumor-to-background ratios. Furthermore, one of most plausible applications of ^{64}Cu labeled compounds is dosimetry studies before radio-therapeutic treatment with ^{67}Cu labeled compounds. In this respect, the following benefits of using ^{67}Cu have to be considered: a half-life of two and half days allows for optimized dosing, combined with only a few days of hospitalization and consequently reduced costs of waste management, lower exposure of radiation of non-target tissue and cost and energy equivalent to ^{177}Lu. ^{64}Cu

labeled cetuximab was proposed for integrated treatment and PET-guided surgery in human gastrointestinal cancer xenografts *(307)*. Similarly, ^{64}Cu-CA003 might serve as tracer for radio-guided surgery. This technique is currently being established with ^{99m}Tc-PSMA may benefit from high resolution PET scans prior surgery and also from its high tracer retention after 24 h *(308)*.

Among all synthesized compounds, we suggest CA003, preferentially in combination with ^{67}Cu as a novel radiotracer for targeting prostate cancer.

4.2. Lead ligands

In order to develop stable compound for labeling with the most relevant lead radioisotopes the chelators DO3AM or *p*-SCN-Bn-TCMC were used. The compounds are based on the lead structure PSMA-617*(39)* which contains the Lys-NH-CO-NH-Glu moiety bearing the 2-naphthylalanine and cyclohexanecarboxylic acid linker to target PSMA with high affinity *(269)*. The linker are favorably to bind PSMA with its lipophilic part pocket in the arene-binding site *(309) (284)*. The interaction between PSMA-617 and PSMA has been demonstrated recently through protein crystallization *(272, 310)*. The hydrophilicity of the chelator needs further examination.

In mice, ^{203}Pb-PSMA-CA012 showed a high tumor uptake of 8.37 ± 3.67 %ID/g at 1 h post injection which is comparable to the reported findings for ^{68}Ga-PSMA-617*(39)* and ^{18}F-PSMA-1007 *(282)*. Based on the preclinical data, exhibiting low nanomolar affinity to PSMA, high internalization ratio and fast kidney clearance, CA012 was identified as a promising shuttle to target PSMA while carrying various isotopes of lead.

In human beings, the dosimetry projected for diagnostic ^{203}Pb-CA012 was found in a dimension that is also found for other clinically established diagnostic examinations (i.e. 6-7 mSv) and could be used for individual treatment planning. An extrapolation from imaging to therapeutic ^{212}Pb-CA012 predicts possible treatment activities of approx. 75-150 MBq. Such a therapy was simulated to cause acceptable off-target radiation to dose-limiting organs, while average tumor absorbed doses (with inter-individual heterogeneity presenting a remarkable source of uncertainty) were projected to be around one half of ^{225}Ac-PSMA-617, the current reference for PSMA-TαT. However, the presumably lower absolute tumor dose might partially be compensated by a higher dose-rate.

In addition to obvious methodical limitations - such as low patient number and two-dimensional organ segmentation on planar scans - our results are based on some critical a priori assumptions that need more detailed discussion.

The physically exact unit for dosimetry would be the absorbed dose (Gy); For statistical radiation effects of single alpha-particles a weighting-factor of 20 is recommended for the transfer into the equivalent dose (Sv). However, PSMA-TαT has already arrived in the clinic and the primary interest of physicians is to predict anti-tumor activity and any side-effects, i.e. deterministic radiation effects. Thus, we decided to report all “doses” as Sv_{RBE5} because a relative biological efficacy (RBE) of 5 for alpha radiation reflects the average factor found in the literature *(136, 311)*. However, using an average RBE-factor is somehow arbitrary because the RBE can vary depending on the chosen biological end-point, different kinds of tissue and micro-dosimetry - i.e. whether a radiopharmaceutical is internalized (e.g. specific uptake in tumor) or just encircling a target cell (e.g. perfusion dependent red-marrow exposure). Therefore, dose-response relationships derived with one alpha-emitting radio-conjugate may not be valid for direct comparisons to other tumor-targeting shuttle molecules. Nevertheless, assuming that all Glu-urea-based PSMA-ligands share a similar cell-level biodistribution, the SUV_{RBE5} should be a sufficient basis to compare ^{212}Pb-CA012 with other alpha-emitter tagged PSMA-ligands that have already been evaluated using the same model assumptions *(140, 283)*.

In the dosimetry benchmark, the therapeutic range of ^{212}Pb-CA012 - defined as the ratio between tumor and possible dose limiting organs - performed second behind ^{225}Ac-PSMA-617 (***Table 18***). Indeed, high inter-individual variability in tumor-dosimetry can exceed factor 2 between two particular patients. However, evaluation of their ^{177}Lu-PSMA 617 scans which were acquired few days later (shown in **Figure 51**) - demonstrates that the two patients chosen for this evaluation were quite representative average patients and not statistical outliers. Also the dose-rate in which a particular total dose is administered does also matters. Mathematically, the first four effective half-lives (biological clearance and physical decay) of a radiopharmaceutical contribute 93% to the final absorbed dose in the target tissue. For ^{212}Pb this is dominated by the short physical half-life of 52 hours. In contrast, for ^{225}Ac-compounds this can be more than 2 weeks and is more dependent on individual tumor biology. As PSA-doubling times of less than 2 weeks are possible in advanced stage prostate cancer, referencing to the initial lesion size, while neglecting additional growth of tumor mass, might misleadingly favor ^{225}Ac-over ^{212}Pb-TαT. Due to the still preliminary knowledge about the biology of TαT, the predictive reliability of the physical dosimetry has limitations and especially in very fast

growing tumors the derived therapeutic ranges have to be interpreted cautiously. Thus, randomized comparison trials would be needed to draw a final conclusion about the clinical value of ^{212}Pb vs. ^{225}Ac PSMA-TαT, respectively.

The most relevant uncertainty of this dosimetry modeling is the assumption that the residence times of ^{212}Pb-CA012 can directly be forwarded to all daughter nuclides neglecting the possibility of interim translocation. As illustrated in **Figure 16** the initial beta-decay of ^{212}Pb-CA012 - only this one is perfectly traced with ^{203}Pb-CA012 - contributes less than 1% to the cumulative equivalent dose whereas the rest arises from the down-stream of the decay chain. Although “DOTA” forms stable complexes with both lead(II) and bismuth(III) isotopes and the recoil of a beta-emission is negligible in comparison to an alpha-emission, it was reported that during the decay from ^{212}Pb to ^{212}Bi 36% of the daughter is lost from the DOTA-chelator *(275, 312)*. The TCMC-chelator also forms stable complexes with both 2+ and 3+ charged heavy metals *(276, 313, 314)*, but its proven strength is the improved *in vivo* stability of its Pb(II) complexes, not a better control of the decay event *(264)*. However, animal experiments with either ^{212}Pb- or ^{212}Bi-labeled internalizing antibodies imply that most of the hematological toxicity is related to the release of free ^{212}Pb *(315-317)*, which has sufficient half-life for redistribution and physiologically accumulates in erythrocytes, kidney, liver and bone *(318)*; this leading source of toxicity should be solved by moving from a DOTA- to a TCMC-based PSMA-ligand *(264)*.

^{212}Pb decays in ^{212}Bi which has a half-life of 1 hour. This is sufficient for effective internalization of the radioisotope in the cells.

The situation is different for daughter nuclides produced extra-cellularly. For circulating ^{212}Pb-CA012 it was assumed that all daughter nuclides will also decay in the blood stream. However, ^{212}Bi has half-life of 1 h and presents a physiological renal accumulation *(320)*; this might further shift the dose limiting toxicity form red-marrow to kidneys. If ^{212}Pb-CA012, bound at the outside of the tumor cell-membrane, decays before its internalization, it must be assumed that 1/3 of the disintegrations from ^{212}Pb to ^{212}Bi will result in a loss from the chelator *(312)*; Once again, some of it might consecutively accumulate in the kidneys. Also the fate of the daughter nuclides arising from the fraction of ^{212}Bi-CA012, still kept in the chelator bound to the membrane surface of the tumor cell should be discussed. ^{212}Bi decays with a 36% probability directly through alpha-emission and thus completely “on target”; the other alpha-particles are generated through ^{212}Po with an additional delay of 0.3µs half-life (**Figure 16**). In an experimental study with a ^{211}At-labeled non-internalizing antibody it was found that the

0.52 s half-life of its first daughter nuclide ^{217}Po, which was assumed to “travel away” freely, decreases the probability of hitting the cell core by factor 2 *(321)*. On the other hand, ^{223}Ra-therapy targets the extra-cellular bone-matrix and the first decay product, ^{219}Rn, is a freely diffusible inert gas with 4.0 s half-life. However, due to incorporation to the extra-cellular bone tissue, 4.0 s are short enough that only 2% of the daughters migrate back to systemic circulation*(321)*. In comparison, the 0.3 µs half-life of ^{212}Po in the ^{212}Pb/^{212}Bi/^{212}Po-decay branch is remarkable close to the assumed instant decay. In contrast, presumably the majority of extra-cellular produced ^{208}Tl ($t_{1/2}$ 3.1 min) will be washed-out from the tumor; however this beta-emitter has a negligible contribution (1-2%) to the total equivalent dose. It should also be mentioned, that even 1.11 MBq of free ^{212}Pb could be injected into mice with a body weight ranging 19-28g, without relevant toxicity at days 7 and 90 *(318)*. Thus there are sufficient safety-margins regarding the premature release of daughter radionuclides.

In sum, with CA012 we designed a PSMA-ligand based on the beneficial characteristics of PSMA-617 *(39)*, exploiting the higher *in-vivo* stability of the Pb[TCMC]$^{2+}$ complex in comparison to Pb[DOTA]$^{2-}$ and in preclinical studies focused on its internalization-inducing effect *(264)*. Thus, from the very beginning this ligand was optimized to match with the specific demands in prospect of ^{212}Pb-PSMA-TαT. However, according to the discussed methodical limitations some empirical dose escalation will still be necessary during clinical translation.

^{212}Pb-TCMC-Trastuzumab, so far the only ^{212}Pb-labeld radiopharmaceutical evaluated in the clinical setting, is administered intraperitoneally *(265, 322)* and there was neither a strong demand for imaging based dosimetry, nor can the dose-escalation of this local therapy guide the development of a systemically administered radiopharmaceutical. However, other small molecules, e.g. for therapy of melanoma *(323, 324)* and neuroendocrine tumors *(325)*, are currently on the way to clinical translation and due to their encouraging fast pharmacokinetics they are considered suitable candidates for ^{212}Pb labeling. Thus, the concept applied to CA012 might serve as a blue print for future development but also as a standard of comparisons to rate the prospects of new radiopharmaceuticals, utilizing the ^{203}Pb/^{212}Pb-tandem approach.

4.3. PSMA-617 derivatives

The main purpose of this study was the synthesis, the preclinical development and a first clinical proof of novel ^{68}Ga/^{177}Lu-labeled PSMA ligands. The rationale for the design was

the improvement of the linker of PSMA-617. The novel compounds comprise the Lys-NH-CO-NH-Glu binding motif *(268, 269)* as their basic structure. The linker moiety was based on the linker used in PSMA-617 *(272, 284)*. This linker and the DOTA moiety were fine tuned to improve the internalization efficiency and the tumor to background ratio. Four representative PSMA binding molecules CA027, CA028, CA029 and CA030 are described here. In CA027 omission of the linker consisting of 2-naphthylalanine and cyclohexanecarboxylic acid substantially decreased the affinity, internalization and consecutive tumor-uptake. CA029 was found to strongly accumulate in the tumor, however due to a high kidney accumulation it was considered inferior to PSMA-617. CA028 and CA030, showed high tumor uptake and lower kidney retention and were consequently studied in greater detail.

As ^{68}Ga-CA028 showed a rapid clearance from the kidneys, this compound reached a high tumor to kidney ratio and its characteristics might be ideally for diagnostic application **Figure 52.** However, after recent introduction of ^{18}F-labeled diagnostic compounds such as ^{18}F-PSMA-1007 the clinical demand for improved ^{68}Ga-labeled diagnostics is shrinking *(326, 327)*. Since ^{177}Lu-CA028 showed signs of degradation in human serum its stability *in vivo* was analyzed by radio-HPLC of tissue extracts; which showed exclusively the intact tracer. However, in contrast to DOTA-conjugates, the chelator moiety of CA028 lacks one amide bridge and thus slightly decreased complex stability with larger metals such as ^{177}Lu and also ^{225}Ac (not presented here) in comparison to ^{68}Ga. Nevertheless, considering the rapid tumor targeting and internalization of these small molecules, the ligand might still have potential because some intra-cellular nuclide loss might be tolerated and the mean standard uptake values (mSUV) derived from the PET demonstrated a higher tumor-to-kidney ratio for CA028 in comparison with the other compounds tested. However, as shown in **Table 13** and **Figure 46**, due to its higher internalization ^{68}Ga-CA030 reached a more persistent tumor uptake which might be preferable for therapeutic application especially when used in combination with radionuclides that decay trough unstable daughter nuclides (e.g. ^{225}Ac).

The linker moieties 2-naphthyl-L-alanine and 4-(aminomethyl)cyclohexanecarboxylic acid used in PSMA-617 had already been proven to provide beneficial pharmacokinetics *(39, 272)*. The linker modification with the respective benzyl moiety connected to the DOTA chelator was found to further improve the tumor targeting characteristics and in CA027, CA029 and CA030 further fine tuning was accomplished by using DOTA variants which contained reduced numbers of polar side chains. More lipophilic chelators were found promising to improve pharmacokinetics when they were introduced to realize copper (*34*)

or lead (*35*) complexed PSMA-ligands *(328, 329)*. However it is relevant to emphasize that the presence of the benzyl group connected directly or via a linker to the chelator, can be assumed to interact with the rigid part of the PSMA binding pocket. It has been demonstrated that the active binding site of PSMA is composed of two structural motifs, one representing a lipophilic pocket and the other interacting with urea-based inhibitors *(277)*. Choosing optimal chelators enables an optimal size, flexibility and polarity of the compounds *(284, 330, 331)*. In total the affinity of ^{68}Ga-CA028 and ^{68}Ga-CA030 to PSMA are comparable to ^{68}Ga-PSMA-617 and ^{68}Ga-PSMA-11 but present improved internalization as demonstrated in our head-to-head-comparison **Table 13** or compared to literature *(39, 291)*. In first clinical application **Figure 52** and Figure 53 the quantitative evaluation ^{68}Ga-CA028 and ^{68}Ga-CA030 demonstrated a slightly prolonged circulation in the blood-pool when compared to ^{68}Ga-PSMA-617 **Table 19**; similar but less pronounced to that of dedicated albumin binding PSMA tracers recently described *(286)*. The available human data for ^{68}Ga-labeled CA028/CA030 and are limited to the initial distribution phase up to 3 h *p.i.*. During this phase the kidney uptake is dominated by an unspecific clearance. However, PSMA is also specifically expressed in kidneys and salivary glands (*3*), and it is possible that due to increased PSMA-specific internalization the novel compounds could also be retained in the kidneys and the salivary glands at later time-points. Thus, dosimetry of ^{177}Lu-CA028/30 up to several days *p.i.* would be required to draw a final decision whether the therapeutic range (ratio of absorbed dose to tumor vs dose limiting normal organs) is really improved with the new compounds. As CA028 is hampered by its lower complex stability with larger radiometals and CA030 presents even more rapid internalization, which is considered favorable for labeling with ^{225}Ac (currently considered one of the academically most interesting therapeutic radio-metals) – we propose CA030 as the most promising ligand for further clinical evaluation.

5. CONCLUSION

This dissertation describes the development and preclinical studies of new inhibitors of the PSMA, which are based on the Glu-ureido-Lys binding motif for imaging and endoradiotherapy purposes. The use of these inhibitors extends the limited use for prostate cancer. It can be used for tumor imaging or treatment of all tumors expressing PSMA.

In order to elucidate the synthesized compounds, a determination of their structure-activity relationship was performed. All synthesized compounds show high inhibition potency in the nanomolar range. The use of both linker moieties 2-naphthyl-L-alanine and 4-(aminomethyl)cyclohexanecarboxylic acid contributed to high internalization ratios. The *in vivo* characterization confirmed the high stability of the promising compounds. Small-animal PET imaging revealed high tumor uptake of the selected compounds. These compounds were used for further biodistribution studies.

Among all developed compounds for radio-labelling with copper, CA003 showed the best pre-clinical properties which ensured the translation into clinics. The high potential of ^{64}Cu-CA003 was underlined by first human application which resulted in a clear visualization of prostate tumor lesions with high contrast.

Among all synthesized compounds for labelling with lead-radioisotopes, ^{212}Pb-CA012 showed to be the most promising compound for PSMA-targeted α-therapy. Even with limitations in the methodology an approach to dosimetry was made possible.

Furthermore, PSMA-617 was optimized by developing novel PSMA ligands comprising a benzyl group in the chelator moiety. A high tumor uptake and low kidney enrichment in comparison with PSMA-617 resulted. The compounds ^{68}Ga-CA028 and ^{68}Ga-CA030 proved to be the best performing compounds and thus were selected for first human application which also showed a clear visualization of prostate cancer lesions with high contrast in patients with metastatic prostate cancer.

6. REFERENCES

1. World Health Organization (WHO). *Retrieved June 2019 from https://www.who.int/news-room/fact-sheets/detail/cancer.*

2. Bray F, Ferlay J, Soerjomataram I, Siegel RL, Torre LA, Jemal A. Global cancer statistics 2018: GLOBOCAN estimates of incidence and mortality worldwide for 36 cancers in 185 countries. *CA: A Cancer Journal for Clinicians.* 2018;68:394-424.

3. National Cancer Institute. *Retrieved Juni 2019 from https://www.cancer.gov/about-cancer/understanding/what-is-cancer.*

4. The History of Cancer. American Cancer Society. *Retrived June 2019 from https://www.cancer.org/cancer/cancer-basics/history-of-cancer.html.*

5. Siegel RL, Miller KD, Jemal A. Cancer statistics, 2018. *CA Cancer J Clin.* 2018;68:7-30.

6. Ferlay J, Colombet M, Soerjomataram I, et al. Cancer incidence and mortality patterns in Europe: Estimates for 40 countries and 25 major cancers in 2018. *Eur J Cancer.* 2018;

7. Raychaudhuri B, Cahill D. Pelvic fasciae in urology. *Ann R Coll Surg Engl.* 2008;90:633-637.

8. Gray´s Anatomy. The Prostate. *Retrieved September 2018 from https://www.bartleby.com/107/263.html.*

9. Reis LO, Billis A, Ferreira FT, Ikari LY, Stellini RF, Ferreira U. Female urethral carcinoma: evidences to origin from Skene's glands. *Urol Oncol.* 2011;29:218-223.

10. Flamini MA, Barbeito CG, Gimeno EJ, Portiansky EL. Morphological characterization of the female prostate (Skene's gland or paraurethral gland) of Lagostomus maximus maximus. *Ann Anat.* 2002;184:341-345.

11. Zaviacic M, Danihel L, Ruzickova M, et al. Immunohistochemical localization of human protein 1 in the female prostate (Skene's gland) and the male prostate. *Histochem J.* 1997;29:219-227.

12. Santos FC, Leite RP, Custodio AM, et al. Testosterone stimulates growth and secretory activity of the female prostate in the adult gerbil (Meriones unguiculatus). *Biol Reprod.* 2006;75:370-379.

13. Fochi RA, Perez AP, Bianchi CV, et al. Hormonal oscillations during the estrous cycle influence the morphophysiology of the gerbil (Meriones unguiculatus) female prostate (skene paraurethral glands). *Biol Reprod.* 2008;79:1084-1091.

14. Bosland MC. The role of steroid hormones in prostate carcinogenesis. *J Natl Cancer Inst Monogr.* 2000;39-66.

15. Taioli E, Sears V, Watson A, et al. Polymorphisms in CYP17 and CYP3A4 and prostate cancer in men of African descent. *Prostate.* 2013;73:668-676.

16. Bostwick DG, Burke HB, Djakiew D, et al. Human prostate cancer risk factors. *Cancer.* 2004;101:2371-2490.

17. Vance TM, Su J, Fontham ET, Koo SI, Chun OK. Dietary antioxidants and prostate cancer: a review. *Nutr Cancer.* 2013;65:793-801.

18. National Institute of Diabetes and Digestive and Kidney Diseases (NIH). *Retrieved September 2018 from https://www.niddk.nih.gov/health-information/urologic-diseases/prostate-problems/prostate-enlargement-benign-prostatic-hyperplasia.*

19. Kim EH, Larson JA, Andriole GL. Management of Benign Prostatic Hyperplasia. *Annu Rev Med.* 2016;67:137-151.

20. Ruddon RW. Cancer biology, 4thedition. *Oxford University Press, Oxford.* 2007;

21. Harvard Medical School. Retrieved September 2018 from. *https://www.harvardprostateknowledge.org/what-is-transrectal-ultrasonography-trus.*

22. Nadji M, Tabei SZ, Castro A, et al. Prostatic-specific antigen: an immunohistologic marker for prostatic neoplasms. *Cancer.* 1981;48:1229-1232.

23. Catalona WJ, Smith DS, Ratliff TL, et al. Measurement of prostate-specific antigen in serum as a screening test for prostate cancer. *N Engl J Med.* 1991;324:1156-1161.

24. Stamey TA, Yang N, Hay AR, McNeal JE, Freiha FS, Redwine E. Prostate-specific antigen as a serum marker for adenocarcinoma of the prostate. *N Engl J Med.* 1987;317:909-916.

25. Hudson MA, Bahnson RR, Catalona WJ. Clinical use of prostate specific antigen in patients with prostate cancer. *J Urol.* 1989;142:1011-1017.

26. Liu W, Hao G, Long MA, Anthony T, Hsieh JT, Sun X. Imparting multivalency to a bifunctional chelator: a scaffold design for targeted PET imaging probes. *Angew Chem Int Ed Engl.* 2009;48:7346-7349.

27. Killian CS, Emrich LJ, Vargas FP, et al. Relative reliability of five serially measured markers for prognosis of progression in prostate cancer. *J Natl Cancer Inst.* 1986;76:179-185.

28. National Cancer Institute (NIH). Prostate-Specific Antigen (PSA) Test *Retrieved September 2018 from https://www.cancer.gov/types/prostate/psa-fact-sheet.*

29. Thompson IM, Pauler DK, Goodman PJ, et al. Prevalence of prostate cancer among men with a prostate-specific antigen level < or =4.0 ng per milliliter. *N Engl J Med.* 2004;350:2239-2246.

30. Turkbey B, Brown AM, Sankineni S, Wood BJ, Pinto PA, Choyke PL. Multiparametric prostate magnetic resonance imaging in the evaluation of prostate cancer. *CA Cancer J Clin.* 2016;66:326-336.

31. Filson CP, Natarajan S, Margolis DJ, et al. Prostate cancer detection with magnetic resonance-ultrasound fusion biopsy: The role of systematic and targeted biopsies. *Cancer.* 2016;122:884-892.

32. Afshar-Oromieh A, Avtzi E, Giesel FL, et al. The diagnostic value of PET/CT imaging with the (68)Ga-labelled PSMA ligand HBED-CC in the diagnosis of recurrent prostate cancer. *Eur J Nucl Med Mol Imaging.* 2015;42:197-209.

33. Anderson CJ, Dehdashti F, Cutler PD, et al. 64Cu-TETA-octreotide as a PET imaging agent for patients with neuroendocrine tumors. *J Nucl Med.* 2001;42:213-221.

34. Bernhard G, P. BR, Enza C, et al. 64Cu-PSMA-617 PET/CT Imaging of Prostate Adenocarcinoma: First In-Human Studies. *Cancer Biother Radiopharm.* 2016;31:277-286.

35. Schoder H, Herrmann K, Gonen M, et al. 2-[18F]fluoro-2-deoxyglucose positron emission tomography for the detection of disease in patients with prostate-specific antigen relapse after radical prostatectomy. *Clin Cancer Res.* 2005;11:4761-4769.

36. Jadvar H. Imaging evaluation of prostate cancer with 18F-fluorodeoxyglucose PET/CT: utility and limitations. *Eur J Nucl Med Mol Imaging.* 2013;40 Suppl 1:S5-10.

37. Souvatzoglou M, Weirich G, Schwarzenboeck S, et al. The sensitivity of [11C]choline PET/CT to localize prostate cancer depends on the tumor configuration. *Clin Cancer Res.* 2011;17:3751-3759.

38. Eder M, Schafer M, Bauder-Wust U, et al. 68Ga-complex lipophilicity and the targeting property of a urea-based PSMA inhibitor for PET imaging. *Bioconjug Chem.* 2012;23:688-697.

39. Benesova M, Schafer M, Bauder-Wust U, et al. Preclinical Evaluation of a Tailor-Made DOTA-Conjugated PSMA Inhibitor with Optimized Linker Moiety for Imaging and Endoradiotherapy of Prostate Cancer. *J Nucl Med.* 2015;56:914-920.

40. Weineisen M, Schottelius M, Simecek J, et al. 68Ga- and 177Lu-Labeled PSMA I&T: Optimization of a PSMA-Targeted Theranostic Concept and First Proof-of-Concept Human Studies. *J Nucl Med.* 2015;56:1169-1176.

41. Rowe SP, Macura KJ, Ciarallo A, et al. Comparison of Prostate-Specific Membrane Antigen-Based 18F-DCFBC PET/CT to Conventional Imaging Modalities for Detection of

Hormone-Naive and Castration-Resistant Metastatic Prostate Cancer. *J Nucl Med.* 2016;57:46-53.

42. Rowe SP, Macura KJ, Mena E, et al. PSMA-Based [(18)F]DCFPyL PET/CT Is Superior to Conventional Imaging for Lesion Detection in Patients with Metastatic Prostate Cancer. *Mol Imaging Biol.* 2016;18:411-419.

43. Cardinale J, Schafer M, Benesova M, et al. Preclinical Evaluation of (18)F-PSMA-1007, a New Prostate-Specific Membrane Antigen Ligand for Prostate Cancer Imaging. *J Nucl Med.* 2017;58:425-431.

44. American Cancer Society. Retrieved September 2018 from. *https://www.cancer.org/cancer/prostate-cancer/detection-diagnosis-staging/staging.html.*

45. Gregorakis AK, Holmes EH, Murphy GP. Prostate-specific membrane antigen: current and future utility. *Semin Urol Oncol.* 1998;16:2-12.

46. Horoszewicz JS, Leong SS, Kawinski E, et al. LNCaP model of human prostatic carcinoma. *Cancer Res.* 1983;43:1809-1818.

47. Davis MI, Bennett MJ, Thomas LM, Bjorkman PJ. Crystal structure of prostate-specific membrane antigen, a tumor marker and peptidase. *Proc Natl Acad Sci U S A.* 2005;102:5981-5986.

48. Elgamal A-AA, Holmes EH, Su SL, et al. Prostate-specific membrane antigen (PSMA): Current benefits and future value. *Seminars in Surgical Oncology.* 2000;18:10-16.

49. Barinka C, Sacha P, Sklenar J, et al. Identification of the N-glycosylation sites on glutamate carboxypeptidase II necessary for proteolytic activity. *Protein Sci.* 2004;13:1627-1635.

50. Schülke N, Varlamova OA, Donovan GP, et al. The homodimer of prostate-specific membrane antigen is a functional target for cancer therapy. *Proceedings of the National Academy of Sciences.* 2003;100:12590.

51. Liu H, Rajasekaran AK, Moy P, et al. Constitutive and Antibody-induced Internalization of Prostate-specific Membrane Antigen. *Cancer Research.* 1998;58:4055.

52. Rajasekaran SA, Anilkumar G, Oshima E, et al. A novel cytoplasmic tail MXXXL motif mediates the internalization of prostate-specific membrane antigen. *Molecular biology of the cell.* 2003;14:4835-4845.

53. Goodman OB, Jr., Barwe SP, Ritter B, et al. Interaction of prostate specific membrane antigen with clathrin and the adaptor protein complex-2. *Int J Oncol.* 2007;31:1199-1203.

54. Anilkumar G, Rajasekaran SA, Wang S, Hankinson O, Bander NH, Rajasekaran AK. Prostate-specific membrane antigen association with filamin A modulates its internalization and NAALADase activity. *Cancer Res.* 2003;63:2645-2648.

55. Anilkumar G, Barwe SP, Christiansen JJ, Rajasekaran SA, Kohn DB, Rajasekaran AK. Association of prostate-specific membrane antigen with caveolin-1 and its caveolae-dependent internalization in microvascular endothelial cells: implications for targeting to tumor vasculature. *Microvasc Res.* 2006;72:54-61.

56. Kawabata H, Yang R, Hirama T, et al. Molecular cloning of transferrin receptor 2. A new member of the transferrin receptor-like family. *J Biol Chem.* 1999;274:20826-20832.

57. Lawrence CM, Ray S, Babyonyshev M, Galluser R, Borhani DW, Harrison SC. Crystal structure of the ectodomain of human transferrin receptor. *Science.* 1999;286:779-782.

58. Mesters JR, Barinka C, Li W, et al. Structure of glutamate carboxypeptidase II, a drug target in neuronal damage and prostate cancer. *EMBO J.* 2006;25:1375-1384.

59. O'Keefe DS, Su SL, Bacich DJ, et al. Mapping, genomic organization and promoter analysis of the human prostate-specific membrane antigen gene. *Biochim Biophys Acta.* 1998;1443:113-127.

60. Silver DA, Pellicer I, Fair WR, Heston WD, Cordon-Cardo C. Prostate-specific membrane antigen expression in normal and malignant human tissues. *Clin Cancer Res.* 1997;3:81-85.

61. O'Keefe DS, Bacich DJ, Heston WD. Comparative analysis of prostate-specific membrane antigen (PSMA) versus a prostate-specific membrane antigen-like gene. *Prostate.* 2004;58:200-210.

62. Troyer JK, Beckett ML, Wright GL, Jr. Detection and characterization of the prostate-specific membrane antigen (PSMA) in tissue extracts and body fluids. *Int J Cancer.* 1995;62:552-558.

63. Wernicke AG, Kim S, Liu H, Bander NH, Pirog EC. Prostate-specific Membrane Antigen (PSMA) Expression in the Neovasculature of Gynecologic Malignancies: Implications for PSMA-targeted Therapy. *Appl Immunohistochem Mol Morphol.* 2017;25:271-276.

64. Luthi-Carter R, Barczak AK, Speno H, Coyle JT. Molecular characterization of human brain N-acetylated alpha-linked acidic dipeptidase (NAALADase). *J Pharmacol Exp Ther.* 1998;286:1020-1025.

65. Yao V, Parwani A, Maier C, Heston WD, Bacich DJ. Moderate expression of prostate-specific membrane antigen, a tissue differentiation antigen and folate hydrolase, facilitates prostate carcinogenesis. *Cancer Res.* 2008;68:9070-9077.

66. Smith-Jones PM, Vallabahajosula S, Goldsmith SJ, et al. In vitro characterization of radiolabeled monoclonal antibodies specific for the extracellular domain of prostate-specific membrane antigen. *Cancer Res.* 2000;60:5237-5243.

67. Pinto JT, Suffoletto BP, Berzin TM, et al. Prostate-specific membrane antigen: a novel folate hydrolase in human prostatic carcinoma cells. *Clin Cancer Res.* 1996;2:1445-1451.

68. Ghosh A, Heston WD. Effect of carbohydrate moieties on the folate hydrolysis activity of the prostate specific membrane antigen. *Prostate.* 2003;57:140-151.

69. Navratil M, Ptacek J, Sacha P, et al. Structural and biochemical characterization of the folyl-poly-gamma-l-glutamate hydrolyzing activity of human glutamate carboxypeptidase II. *Febs j.* 2014;281:3228-3242.

70. Zhao R, Matherly LH, Goldman ID. Membrane transporters and folate homeostasis: intestinal absorption and transport into systemic compartments and tissues. *Expert Rev Mol Med.* 2009;11:e4.

71. Barinka C, Rojas C, Slusher B, Pomper M. Glutamate carboxypeptidase II in diagnosis and treatment of neurologic disorders and prostate cancer. *Curr Med Chem.* 2012;19:856-870.

72. Robinson MB, Blakely RD, Couto R, Coyle JT. Hydrolysis of the brain dipeptide N-acetyl-L-aspartyl-L-glutamate. Identification and characterization of a novel N-acetylated alpha-linked acidic dipeptidase activity from rat brain. *J Biol Chem.* 1987;262:14498-14506.

73. Rajasekaran AK, Anilkumar G, Christiansen JJ. Is prostate-specific membrane antigen a multifunctional protein? *Am J Physiol Cell Physiol.* 2005;288:C975-981.

74. Spatz S, Tolkach Y, Jung K, et al. Comprehensive Evaluation of Prostate Specific Membrane Antigen Expression in the Vasculature of Renal Tumors: Implications for Imaging Studies and Prognostic Role. *J Urol.* 2018;199:370-377.

75. Tolkach Y, Gevensleben H, Bundschuh R, et al. Prostate-specific membrane antigen in breast cancer: a comprehensive evaluation of expression and a case report of radionuclide therapy. *Breast Cancer Res Treat.* 2018;169:447-455.

76. Haffner MC, Laimer J, Chaux A, et al. High expression of prostate-specific membrane antigen in the tumor-associated neo-vasculature is associated with worse prognosis in squamous cell carcinoma of the oral cavity. *Mod Pathol.* 2012;25:1079-1085.

77. Haffner MC, Kronberger IE, Ross JS, et al. Prostate-specific membrane antigen expression in the neovasculature of gastric and colorectal cancers. *Hum Pathol.* 2009;40:1754-1761.

78. Chang SS, O'Keefe DS, Bacich DJ, Reuter VE, Heston WD, Gaudin PB. Prostate-specific membrane antigen is produced in tumor-associated neovasculature. *Clin Cancer Res.* 1999;5:2674-2681.

79. Horoszewicz JS, Kawinski E, Murphy GP. Monoclonal antibodies to a new antigenic marker in epithelial prostatic cells and serum of prostatic cancer patients. *Anticancer Res.* 1987;7:927-935.

80. Haseman MK, Rosenthal SA, Polascik TJ. Capromab Pendetide imaging of prostate cancer. *Cancer Biother Radiopharm.* 2000;15:131-140.

81. Manyak MJ, Hinkle GH, Olsen JO, et al. Immunoscintigraphy with indium-111-capromab pendetide: evaluation before definitive therapy in patients with prostate cancer. *Urology.* 1999;54:1058-1063.

82. Kahn D, Williams RD, Manyak MJ, et al. 111Indium-capromab pendetide in the evaluation of patients with residual or recurrent prostate cancer after radical prostatectomy. The ProstaScint Study Group. *J Urol.* 1998;159:2041-2046; discussion 2046-2047.

83. Lopes AD, Davis WL, Rosenstraus MJ, Uveges AJ, Gilman SC. Immunohistochemical and pharmacokinetic characterization of the site-specific immunoconjugate CYT-356 derived from antiprostate monoclonal antibody 7E11-C5. *Cancer Res.* 1990;50:6423-6429.

84. Troyer JK, Feng Q, Beckett ML, Wright GL, Jr. Biochemical characterization and mapping of the 7E11-C5.3 epitope of the prostate-specific membrane antigen. *Urol Oncol.* 1995;1:29-37.

85. Han M, Partin AW. Current Clinical Applications of the In-capromab Pendetide Scan (ProstaScint(R) Scan, Cyt-356). *Reviews in urology.* 2001;3:165-171.

86. Manyak MJ. Clinical Applications of Radioimmunoscintigraphy with Prostate-Specific Antibodies for Prostate Cancer: Radiolabeled monoclonal antibodies may provide more precise localization of prostate cancer. *Cancer Control.* 1998;5:493-499.

87. Sartor O, McLeod D. Indium-111-capromab pendetide scans: an important test relevant to clinical decision making. *Urology.* 2001;57:399-401.

88. Vallabhajosula S, Kuji I, Hamacher KA, et al. Pharmacokinetics and biodistribution of 111In- and 177Lu-labeled J591 antibody specific for prostate-specific membrane antigen: prediction of 90Y-J591 radiation dosimetry based on 111In or 177Lu? *J Nucl Med.* 2005;46:634-641.

89. Tagawa ST, Milowsky MI, Morris M, et al. Phase II study of Lutetium-177-labeled anti-prostate-specific membrane antigen monoclonal antibody J591 for metastatic castration-resistant prostate cancer. *Clin Cancer Res.* 2013;19:5182-5191.

90. P. Maresca K, Hillier S, Lu G, et al. *Small molecule inhibitors of PSMA incorporating technetium-99m for imaging prostate cancer: Effects of chelate design on pharmacokinetics.* Vol 3892012.

91. Lesche R, Kettschau G, Gromov AV, et al. Preclinical evaluation of BAY 1075553, a novel (18)F-labelled inhibitor of prostate-specific membrane antigen for PET imaging of prostate cancer. *Eur J Nucl Med Mol Imaging.* 2014;41:89-101.

92. Foss CA, Mease RC, Fan H, et al. Radiolabeled small-molecule ligands for prostate-specific membrane antigen: in vivo imaging in experimental models of prostate cancer. *Clin Cancer Res.* 2005;11:4022-4028.

93. Afshar-Oromieh A, Hetzheim H, Kratochwil C, et al. The Theranostic PSMA Ligand PSMA-617 in the Diagnosis of Prostate Cancer by PET/CT: Biodistribution in Humans, Radiation Dosimetry, and First Evaluation of Tumor Lesions. *J Nucl Med.* 2015;56:1697-1705.

94. Kularatne SA, Venkatesh C, Santhapuram H-KR, et al. Synthesis and Biological Analysis of Prostate-Specific Membrane Antigen-Targeted Anticancer Prodrugs. *Journal of Medicinal Chemistry.* 2010;53:7767-7777.

95. Mukherjee A, Darlington T, Baldwin R, et al. Development and screening of a series of antibody-conjugated and silica-coated iron oxide nanoparticles for targeting the prostate-specific membrane antigen. *ChemMedChem.* 2014;9:1356-1360.

96. Hrkach J, Von Hoff D, Mukkaram Ali M, et al. Preclinical development and clinical translation of a PSMA-targeted docetaxel nanoparticle with a differentiated pharmacological profile. *Sci Transl Med.* 2012;4:128ra139.

97. Tykvart J, Navrátil V, Sedlák F, et al. Comparative analysis of monoclonal antibodies against prostate-specific membrane antigen (PSMA). *The Prostate.* 2014;74:1674-1690.

98. Pandit-Taskar N, O'Donoghue JA, Beylergil V, et al. ^{89}Zr-huJ591 immuno-PET imaging in patients with advanced metastatic prostate cancer. *European journal of nuclear medicine and molecular imaging.* 2014;41:2093-2105.

99. Behe M, Alt K, Deininger F, et al. In vivo testing of 177Lu-labelled anti-PSMA antibody as a new radioimmunotherapeutic agent against prostate cancer. *In Vivo.* 2011;25:55-59.

100. Olafsen T, Bartlett D, Ho D, et al. Minibody imaging of prostate-specific membrane antigen (PSMA): From concept to clinic. *Journal of Clinical Oncology.* 2014;32:e16057-e16057.

101. Wu X, Ding B, Gao J, et al. Second-generation aptamer-conjugated PSMA-targeted delivery system for prostate cancer therapy. *Int J Nanomedicine.* 2011;6:1747-1756.

102. Wang J, Maurer L. Positron Emission Tomography: applications in drug discovery and drug development. *Curr Top Med Chem.* 2005;5:1053-1075.

103. Gambhir SS. Molecular imaging of cancer with positron emission tomography. *Nat Rev Cancer.* 2002;2:683-693.

104. Melcher CL. Scintillation crystals for PET. *J Nucl Med.* 2000;41:1051-1055.

105. Zyromska A, Malkowski B, Wisniewski T, Majewska K, Reszke J, Makarewicz R. (15)O-H2O PET/CT as a tool for the quantitative assessment of early post-radiotherapy changes of heart perfusion in breast carcinoma patients. *Br J Radiol.* 2018;91:20170653.

106. Albano D, Giubbini R, Bertagna F. (13)N-NH3 PET/CT in oncological disease. *Jpn J Radiol.* 2019;

107. Li M, Jiang D, Barnhart TE, et al. Immuno-PET imaging of VEGFR-2 expression in prostate cancer with (89)Zr-labeled ramucirumab. *Am J Cancer Res.* 2019;9:2037-2046.

108. Strijckmans K. The isochronous cyclotron: principles and recent developments. *Computerized Medical Imaging and Graphics.* 2001;25:69-78.

109. Newhouse KE. The Metabolism of the Human Brain Studied with Positron Emission Tomography. *The Yale Journal of Biology and Medicine.* 1985;58:412-412.

110. Di Chiro G. Positron emission tomography using [18F] fluorodeoxyglucose in brain tumors. A powerful diagnostic and prognostic tool. *Invest Radiol.* 1987;22:360-371.

111. Prekeges J. Nuclear Medicine Instrumentation. *Jones Bartlett & Learning, Burlington.* 2013;

112. Sharp PF, Gemmell H. G., Murray A. D. . Practical Nuclear Medicine. *Springer Verlag London Limited.* 2005;

113. Biersack HJ, Freeman LM. Clinical Nuclear Medicine. *Springer Verlag Berlin, Heidelberg.* 2007;

114. Peterson TE, Furenlid LR. SPECT detectors: the Anger Camera and beyond. *Physics in medicine and biology.* 2011;56:R145-R182.

115. Moore SC, Kouris K, Cullum I. Collimator design for single photon emission tomography. *European Journal of Nuclear Medicine.* 1992;19:138-150.

116. Kimiaei S, Larsson SA, Jacobsson H. Collimator design for improved spatial resolution in SPECT and planar scintigraphy. *J Nucl Med.* 1996;37:1417-1421.

117. Guerin B, Tremblay S, Rodrigue S, et al. Cyclotron production of 99mTc: an approach to the medical isotope crisis. *J Nucl Med.* 2010;51:13n-16n.

118. Madsen MT. Recent advances in SPECT imaging. *J Nucl Med.* 2007;48:661-673.

119. Cuocolo A, Pappata S, Zampella E, Assante R. Advances in SPECT Methodology. *Int Rev Neurobiol.* 2018;141:77-96.

120. Al-Oweidi AS, Albabtain H, Kharabsheh SM, et al. Prevalence and predictors of myocardial ischemia by preoperative myocardial perfusion single photon emission computed tomography in patients undergoing noncardiac surgery. *Ann Saudi Med.* 2017;37:461-468.

121. Verschueren J, Huyghe I, Van den Wyngaert T. Ovarian cancer unmasked by technetium-99m bone scintigraphy and single-photon emission computed tomography-computed tomography. *World journal of nuclear medicine.* 2019;18:58-60.

122. Sahebari M, Rezaieyazdi Z, Khodashahi M, Abbasi B, Ayatollahi F. Brain Single Photon Emission Computed Tomography Scan (SPECT) and functional MRI in Systemic Lupus Erythematosus Patients with Cognitive Dysfunction: A Systematic Review. *Asia Ocean J Nucl Med Biol.* 2018;6:97-107.

123. Dos Santos JC, Schafer M, Bauder-Wust U, et al. Development and dosimetry of (203)Pb/(212)Pb-labelled PSMA ligands: bringing "the lead" into PSMA-targeted alpha therapy? *Eur J Nucl Med Mol Imaging.* 2019;46:1081-1091.

124. Sadeghi M, Enferadi M, Shirazi A. External and internal radiation therapy: past and future directions. *J Cancer Res Ther.* 2010;6:239-248.

125. Milad E, Mahdi S, Alireza S. Radiation Therapy in the Early 21st Century: Technological Advances. *Current Cancer Therapy Reviews.* 2011;7:303-318.

126. Velic D, Couturier AM, Ferreira MT, et al. DNA Damage Signalling and Repair Inhibitors: The Long-Sought-After Achilles' Heel of Cancer. *Biomolecules.* 2015;5:3204-3259.

127. Lewanski CR, Gullick WJ. Radiotherapy and cellular signalling. *Lancet Oncol.* 2001;2:366-370.

128. Wang J-s, Wang H-j, Qian H-l. Biological effects of radiation on cancer cells. *Military Medical Research.* 2018;5:20.

129. Wangler C, Buchmann I, Eisenhut M, Haberkorn U, Mier W. Radiolabeled peptides and proteins in cancer therapy. *Protein Pept Lett.* 2007;14:273-279.

130. Seymour CB, Mothersill C. Radiation-induced bystander effects — implications for cancer. *Nature Reviews Cancer.* 2004;4:158-164.

131. Najafi M, Fardid R, Hadadi G, Fardid M. The mechanisms of radiation-induced bystander effect. *Journal of biomedical physics & engineering.* 2014;4:163-172.

132. Vértes A, Nagy S, Klencsár Z, G. Lovas R, Roesch F. *Handbook of Nuclear Chemistry.* Vol 42011.

133. Dash A, Knapp FF, Pillai MR. Targeted radionuclide therapy--an overview. *Curr Radiopharm.* 2013;6:152-180.

134. *Therapeutic Applications of Radiopharmaceuticals*. Vienna: INTERNATIONAL ATOMIC ENERGY AGENCY; 2001.

135. Yong KJ, Milenic DE, Baidoo KE, Brechbiel MW. (212)Pb-radioimmunotherapy induces G(2) cell-cycle arrest and delays DNA damage repair in tumor xenografts in a model for disseminated intraperitoneal disease. *Mol Cancer Ther.* 2012;11:639-648.

136. Sgouros G, Roeske JC, McDevitt MR, et al. MIRD Pamphlet No. 22 (abridged): radiobiology and dosimetry of alpha-particle emitters for targeted radionuclide therapy. *J Nucl Med.* 2010;51:311-328.

137. Gorin J-B, Gouard S, Ménager J, et al. Alpha Particles Induce Autophagy in Multiple Myeloma Cells. *Frontiers in medicine.* 2015;2:74-74.

138. Kratochwil C, Giesel FL, Bruchertseifer F, et al. (2)(1)(3)Bi-DOTATOC receptor-targeted alpha-radionuclide therapy induces remission in neuroendocrine tumours refractory to beta radiation: a first-in-human experience. *Eur J Nucl Med Mol Imaging.* 2014;41:2106-2119.

139. Gorin JB, Guilloux Y, Morgenstern A, Cherel M, Davodeau F, Gaschet J. Using alpha radiation to boost cancer immunity? *Oncoimmunology.* 2014;3:e954925.

140. Kratochwil C, Bruchertseifer F, Rathke H, et al. Targeted alpha-Therapy of Metastatic Castration-Resistant Prostate Cancer with (225)Ac-PSMA-617: Dosimetry Estimate and Empiric Dose Finding. *J Nucl Med.* 2017;58:1624-1631.

141. Kratochwil C, Bruchertseifer F, Rathke H, et al. Targeted alpha-Therapy of Metastatic Castration-Resistant Prostate Cancer with (225)Ac-PSMA-617: Swimmer-Plot Analysis Suggests Efficacy Regarding Duration of Tumor Control. *J Nucl Med.* 2018;59:795-802.

142. Verburg FA, Heinzel A, Hänscheid H, Mottaghy FM, Luster M, Giovanella L. Nothing new under the nuclear sun: towards 80 years of theranostics in nuclear medicine. *European Journal of Nuclear Medicine and Molecular Imaging.* 2014;41:199-201.

143. Bentzen SM. Theragnostic imaging for radiation oncology: dose-painting by numbers. *The Lancet Oncology.* 2005;6:112-117.

144. Fani M, Maecke HR. Radiopharmaceutical development of radiolabelled peptides. *Eur J Nucl Med Mol Imaging.* 2012;39 Suppl 1:S11-30.

145. Reubi JC. Peptide receptors as molecular targets for cancer diagnosis and therapy. *Endocr Rev.* 2003;24:389-427.

146. Hertz S, Roberts A, Evans RD. Radioactive Iodine as an Indicator in the Study of Thyroid Physiology. *Proceedings of the Society for Experimental Biology and Medicine.* 1938;38:510-513.

147. Hertz S, Roberts A. Application of radioactive iodine in therapy of Graves' disease. *Journal of Clinical Investigation.* 1942;21:624.

148. SEIDLIN SM, MARINELLI LD, OSHRY E. RADIOACTIVE IODINE THERAPY: Effect on Functioning Metastases of Adenocarcinoma of the Thyroid. *JAMA.* 1946;132:838-847.

149. Lassmann M, Hänscheid H, Chiesa C, Hindorf C, Flux G, Luster M. EANM Dosimetry Committee series on standard operational procedures for pre-therapeutic dosimetry I: blood and bone marrow dosimetry in differentiated thyroid cancer therapy. *European Journal of Nuclear Medicine and Molecular Imaging.* 2008;35:1405.

150. Sisson JC, Yanik GA. Theranostics: Evolution of the Radiopharmaceutical Meta-Iodobenzylguanidine in Endocrine Tumors. *Seminars in Nuclear Medicine.* 2012;42:171-184.

151. Oberg K. Molecular Imaging Radiotherapy: Theranostics for Personalized Patient Management of Neuroendocrine Tumors (NETs). *Theranostics.* 2012;2:448-458.

152. Krenning EP, Kooij PP, Bakker WH, et al. Radiotherapy with a radiolabeled somatostatin analogue, [111In-DTPA-D-Phe1]-octreotide. A case history. *Ann N Y Acad Sci.* 1994;733:496-506.

153. Hennrich U, Kopka K. Lutathera((R)): The First FDA- and EMA-Approved Radiopharmaceutical for Peptide Receptor Radionuclide Therapy. *Pharmaceuticals (Basel).* 2019;12:

154. Revy A, Hallouard F, Joyeux-Klamber S, Skanjeti A, Rioufol C, Fraysse M. Feasibility and Evaluation of Automated Methods for Radiolabeling of Radiopharmaceutical Kits with Gallium-68. *Curr Radiopharm.* 2019;12:229-237.

155. Wild D, Bomanji JB, Benkert P, et al. Comparison of 68Ga-DOTANOC and 68Ga-DOTATATE PET/CT within patients with gastroenteropancreatic neuroendocrine tumors. *J Nucl Med.* 2013;54:364-372.

156. Gabriel M, Decristoforo C, Kendler D, et al. 68Ga-DOTA-Tyr3-octreotide PET in neuroendocrine tumors: comparison with somatostatin receptor scintigraphy and CT. *J Nucl Med.* 2007;48:508-518.

157. de Jong M, Breeman WA, Bernard BF, et al. [177Lu-DOTA(0),Tyr3] octreotate for somatostatin receptor-targeted radionuclide therapy. *Int J Cancer.* 2001;92:628-633.

158. de Jong M, Bakker WH, Krenning EP, et al. Yttrium-90 and indium-111 labelling, receptor binding and biodistribution of [DOTA0,d-Phe1,Tyr3]octreotide, a promising somatostatin analogue for radionuclide therapy. *Eur J Nucl Med.* 1997;24:368-371.

159. Helisch A, Forster GJ, Reber H, et al. Pre-therapeutic dosimetry and biodistribution of 86Y-DOTA-Phe1-Tyr3-octreotide versus 111In-pentetreotide in patients with advanced neuroendocrine tumours. *Eur J Nucl Med Mol Imaging.* 2004;31:1386-1392.

160. Vegt E, de Jong M, Wetzels JF, et al. Renal toxicity of radiolabeled peptides and antibody fragments: mechanisms, impact on radionuclide therapy, and strategies for prevention. *J Nucl Med.* 2010;51:1049-1058.

161. Rathke H, Flechsig P, Mier W, et al. Dosimetry Estimate and Initial Clinical Experience with (90)Y-PSMA-617. *J Nucl Med.* 2019;60:806-811.

162. Violet J, Jackson P, Ferdinandus J, et al. Dosimetry of (177)Lu-PSMA-617 in Metastatic Castration-Resistant Prostate Cancer: Correlations Between Pretherapeutic Imaging and Whole-Body Tumor Dosimetry with Treatment Outcomes. *J Nucl Med.* 2019;60:517-523.

163. Sathekge M, Bruchertseifer F, Knoesen O, et al. (225)Ac-PSMA-617 in chemotherapy-naive patients with advanced prostate cancer: a pilot study. *Eur J Nucl Med Mol Imaging.* 2019;46:129-138.

164. Sathekge M, Knoesen O, Meckel M, Modiselle M, Vorster M, Marx S. 213Bi-PSMA-617 targeted alpha-radionuclide therapy in metastatic castration-resistant prostate cancer. *Eur J Nucl Med Mol Imaging.* 2017;44:1099-1100.

165. Umbricht CA, Benesova M, Schmid RM, et al. (44)Sc-PSMA-617 for radiotheragnostics in tandem with (177)Lu-PSMA-617-preclinical investigations in comparison with (68)Ga-PSMA-11 and (68)Ga-PSMA-617. *EJNMMI Res.* 2017;7:9.

166. Hayes RL. The medical use of gallium radionuclides: a brief history with some comments. *Semin Nucl Med.* 1978;8:183-191.

167. Lide DR. *CRC Handbook of Chemistry and Physics, 85th Edition*: Taylor & Francis; 2004.

168. Holden NE, Coplen TB, Böhlke JK, et al. IUPAC Periodic Table of the Elements and Isotopes (IPTEI) for the Education Community (IUPAC Technical Report). *Pure and Applied Chemistry.* 2018;90:1833-2092.

169. Lewis MR, Reichert DE, Laforest R, et al. Production and purification of gallium-66 for preparation of tumor-targeting radiopharmaceuticals. *Nucl Med Biol.* 2002;29:701-706.

170. Staab EV, McCartney WH. Role of gallium 67 in inflammatory disease. *Semin Nucl Med.* 1978;8:219-234.

171. Zeng D, Anderson C. Production and Purification of Metal Radionuclides for PET Imaging of Disease. *Solvent Extraction and Ion Exchange.* 2013;31:

172. Browne E, Firestone RB, Shirley VS. *Table of radioactive isotopes*. United States: John Wiley and Sons Inc; 1986.

173. Szelecsényi F, Boothe TE, Tavano E, Plitnikas ME, Tárkányi F. Compilation of cross sections/thick target yields for 66Ga, 67Ga and 68Ga production using Zn targets up to 30 MeV proton energy. *Applied Radiation and Isotopes.* 1994;45:473-500.

174. Naidoo C, van der Walt TN. Cyclotron production of 67Ga(III) with a tandem natGe-natZn target. *Appl Radiat Isot.* 2001;54:915-919.

175. Little FE, Lagunas-Solar MC. Cyclotron production of 67Ga. Cross sections and thick-target yields for the 67Zn (p,n) and 68Zn (p,2n) reactions. *The International Journal of Applied Radiation and Isotopes.* 1983;34:631-637.

176. O'Connell JB, Robinson JA, Henkin RE, Gunnar RM. Gallium-67 citrate scanning for noninvasive detection of inflammation in pericardial diseases. *Am J Cardiol.* 1980;46:879-884.

177. Delcambre C, Reman O, Henry-Amar M, et al. Clinical relevance of gallium-67 scintigraphy in lymphoma before and after therapy. *Eur J Nucl Med.* 2000;27:176-184.

178. Breeman WA, Verbruggen AM. The 68Ge/ 68Ga generator has high potential, but when can we use 68Ga-labelled tracers in clinical routine? *Eur J Nucl Med Mol Imaging.* 2007;34:978-981.

179. McElvany KD, Hopkins KT, Welch MJ. Comparison of 68Ge/68Ga generator systems for radiopharmaceutical production. *The International Journal of Applied Radiation and Isotopes.* 1984;35:521-524.

180. Pandey MK, Byrne JF, Jiang H, Packard AB, DeGrado TR. Cyclotron production of (68)Ga via the (68)Zn(p,n)(68)Ga reaction in aqueous solution. *American journal of nuclear medicine and molecular imaging.* 2014;4:303-310.

181. Naidoo C, van der Walt T, Raubenheimer H. Cyclotron production of 68Ge with a Ga2O target. *Journal of Radioanalytical and Nuclear Chemistry.* 2002;253:

182. Kambali I, A Wibowo F. Comparison of gallium-68 production yields from (p,2n), (α ,2n) and (p,n) nuclear reactions applicable for cancer diagnosis. *Journal of Physics: Conference Series.* 2019;1198:022003.

183. Faßbender M, Nortier FM, Phillips DR, et al. Some nuclear chemical aspects of medical generator nuclide production at the Los Alamos hot cell facility. *Radiochimica Acta.* Vol 92. 2004:237.

184. Al-Nahhas A, Win Z, Szyszko T, Singh A, Khan S, Rubello D. What can gallium-68 PET add to receptor and molecular imaging? *Eur J Nucl Med Mol Imaging.* 2007;34:1897-1901.

185. Dijkgraaf I, Boerman OC, Oyen WJ, Corstens FH, Gotthardt M. Development and application of peptide-based radiopharmaceuticals. *Anticancer Agents Med Chem.* 2007;7:543-551.

186. Maecke HR, André JP. 68Ga-PET Radiopharmacy: A Generator-Based Alternative to 18F-Radiopharmacy2007; Berlin, Heidelberg.

187. Sanchez-Crespo A, Andreo P, Larsson SA. Positron flight in human tissues and its influence on PET image spatial resolution. *Eur J Nucl Med Mol Imaging.* 2004;31:44-51.

188. Velikyan I. Positron emitting [68Ga]Ga-based imaging agents: chemistry and diversity. *Med Chem.* 2011;7:345-379.

189. Smith D, Breeman W, Sims-Mourtada J. The untapped potential of Gallium 68-PET: The next wave of 68Ga-agents. *Applied radiation and isotopes : including data, instrumentation and methods for use in agriculture, industry and medicine.* 2012;76:

190. Waldmann CM, Stuparu AD, van Dam RM, Slavik R. The Search for an Alternative to [(68)Ga]Ga-DOTA-TATE in Neuroendocrine Tumor Theranostics: Current State of (18)F-labeled Somatostatin Analog Development. *Theranostics.* 2019;9:1336-1347.

191. Antunes P, Ginj M, Zhang H, et al. Are radiogallium-labelled DOTA-conjugated somatostatin analogues superior to those labelled with other radiometals? *Eur J Nucl Med Mol Imaging.* 2007;34:982-993.

192. Lucignani G. Labeling peptides with PET radiometals: Vulcan's forge. *Eur J Nucl Med Mol Imaging.* 2008;35:209-215.

193. Roesch F. Scandium-44: Benefits of a Long-Lived PET Radionuclide Available from the 44Ti/44Sc Generator System. *Current radiopharmaceuticals.* 2012;5:187-201.

194. Pruszyński M, Loktionova NS, Filosofov DV, Rösch F. Post-elution processing of 44Ti/44Sc generator-derived 44Sc for clinical application. *Applied Radiation and Isotopes.* 2010;68:1636-1641.

195. Pruszynski M, Majkowska-Pilip A, Loktionova NS, Eppard E, Roesch F. Radiolabeling of DOTATOC with the long-lived positron emitter 44Sc. *Appl Radiat Isot.* 2012;70:974-979.

196. Mausner LF, Kolsky KL, Joshi V, Srivastava SC. Radionuclide development at BNL for nuclear medicine therapy. *Appl Radiat Isot.* 1998;49:285-294.

197. Filosofov DV, Loktionova NS, Rösch F. A 44Ti/44Sc radionuclide generator for potential application of 44Sc-based PET-radiopharmaceuticals. *Radiochimica Acta International journal for chemical aspects of nuclear science and technology.* Vol 98. 2010:149.

198. Pietrelli L, Mausner LF, Kolsky KL. Separation of carrier-free47Sc from titanium targets. *Journal of Radioanalytical and Nuclear Chemistry.* 1992;157:335-345.

199. Bokhari TH, Mushtaq A, Khan IU. Separation of no-carrier-added radioactive scandium from neutron irradiated titanium. *Journal of Radioanalytical and Nuclear Chemistry.* 2010;283:389-393.

200. Huclier S, Sabatie A, Ribet S, et al. Chemical and biological evaluation of scandium(III)-polyaminopolycarboxylate complexes as potential PET agents and radiopharmaceuticals. *Radiochimica Acta.* 2011;99:653–662.

201. Alliot C, Kerdjoudj R, Michel N, Haddad F, Huclier-Markai S. Cyclotron production of high purity 44m,44Sc with deuterons from 44CaCO3 targets. *Nuclear Medicine and Biology.* 2015;42:524-529.

202. Koumarianou E, Pawlak D, Korsak A, Mikolajczak R. Comparison of receptor affinity of natSc-DOTA-TATE versus natGa-DOTA-TATE. *Nucl Med Rev Cent East Eur.* 2011;14:85-89.

203. Bartoś B, Majkowska A, Krajewski S, Bilewicz A. New separation method of no-carrier-added 47Sc from titanium targets. *Radiochimica Acta International journal for chemical aspects of nuclear science and technology.* Vol 100. 2012:457.

204. Połosak M, Piotrowska A, Krajewski S, Bilewicz A. Stability of (47)Sc-complexes with acyclic polyamino-polycarboxylate ligands. *Journal of radioanalytical and nuclear chemistry.* 2013;295:1867-1872.

205. Muller C, Bunka M, Haller S, et al. Promising prospects for 44Sc-/47Sc-based theragnostics: application of 47Sc for radionuclide tumor therapy in mice. *J Nucl Med.* 2014;55:1658-1664.

206. Cydzik I, Krajewski S, Abbas K, Simonell F, Bulgheroni A, Kasperek A. Labelling of DOTATATE with cyclotron produced 44Sc and 43Sc. *Q J Nucl Med Mol Imaging.* 2012;56:33-34.

207. Rotsch DA, Brown MA, Nolen JA, et al. Electron linear accelerator production and purification of scandium-47 from titanium dioxide targets. *Appl Radiat Isot.* 2018;131:77-82.

208. Majkowska-Pilip A, Bilewicz A. Macrocyclic complexes of scandium radionuclides as precursors for diagnostic and therapeutic radiopharmaceuticals. *J Inorg Biochem.* 2011;105:313-320.

209. Daraban L, Adam Rebeles R, Hermanne A, Tarkanyi F, Takacs S. Study of the excitation functions for 43K, 43,44,44mSc and 44Ti by proton irradiation on 45Sc up to 37MeV. *Nuclear Instruments and Methods in Physics Research Section B: Beam Interactions with Materials and Atoms.* 2009;267:755-759.

210. Domnanich KA, Eichler R, Müller C, et al. Production and separation of 43Sc for radiopharmaceutical purposes. *EJNMMI Radiopharmacy and Chemistry.* 2017;2:14.

211. Mamtimin M, Harmon F, Starovoitova VN. Sc-47 production from titanium targets using electron linacs. *Applied Radiation and Isotopes.* 2015;102:1-4.

212. Das T, Banerjee S. Theranostic Applications of Lutetium-177 in Radionuclide Therapy. *Current radiopharmaceuticals.* 2015;9:

213. Das T, Chakraborty S, Unni PR, et al. 177Lu-labeled cyclic polyaminophosphonates as potential agents for bone pain palliation. *Appl Radiat Isot.* 2002;57:177-184.

214. Liu Z, Ma T, Liu H, et al. 177Lu-labeled antibodies for EGFR-targeted SPECT/CT imaging and radioimmunotherapy in a preclinical head and neck carcinoma model. *Mol Pharm.* 2014;11:800-807.

215. Rudisile S, Gosewisch A, Wenter V, et al. Salvage PRRT with (177)Lu-DOTA-octreotate in extensively pretreated patients with metastatic neuroendocrine tumor (NET): dosimetry, toxicity, efficacy, and survival. *BMC Cancer.* 2019;19:788.

216. Pandey U, Kameswaran M, Gamre N, Dash A. Preparation of (177) Lu-labeled Nimotuzumab for radioimmunotherapy of EGFR-positive cancers: Comparison of DOTA

and CHX-A''-DTPA as bifunctional chelators. *J Labelled Comp Radiopharm.* 2019;62:158-165.

217. Escudero-Castellanos A, Ocampo-Garcia B, Ferro-Flores G, et al. Synthesis and preclinical evaluation of the 177Lu-DOTA-PSMA(inhibitor)-Lys3-bombesin heterodimer designed as a radiotheranostic probe for prostate cancer. *Nucl Med Commun.* 2019;40:278-286.

218. Vértes A, Nagy S, Klencsár Z, Lovas RG, Rösch F. *Handbook of Nuclear Chemistry: Vol. 1: Basics of Nuclear Science; Vol. 2: Elements and Isotopes: Formation, Transformation, Distribution; Vol. 3: Chemical Applications of Nuclear Reactions and Radiation; Vol. 4: Radiochemistry and Radiopharmaceutical Chemistry in Life Sciences; Vol. 5: Instrumentation, Separation Techniques, Environmental Issues; Vol. 6: Nuclear Energy Production and Safety Issues*: Springer US; 2010.

219. A. Lebedev N, F. Novgorodov A, Misiak R, Brockmann J, Roesch F. Radiochemical separation of no-carrier-added 177 Lu as produced via the 176 Yb n,γ 177 Yb→ 177 Lu process. *Applied Radiation and Isotopes - APPL RADIAT ISOTOPES.* 2000;53:421-425.

220. Puig S, Thiele DJ. Molecular mechanisms of copper uptake and distribution. *Current Opinion in Chemical Biology.* 2002;6:171-180.

221. Banerjee SR, Pullambhatla M, Foss CA, et al. (6)(4)Cu-labeled inhibitors of prostate-specific membrane antigen for PET imaging of prostate cancer. *J Med Chem.* 2014;57:2657-2669.

222. Gourni E, Canovas C, Goncalves V, Denat F, Meyer PT, Maecke HR. (R)-NODAGA-PSMA: A Versatile Precursor for Radiometal Labeling and Nuclear Imaging of PSMA-Positive Tumors. *PLOS ONE.* 2015;10:e0145755.

223. Novak-Hofer I, Schubiger PA. Copper-67 as a therapeutic nuclide for radioimmunotherapy. *Eur J Nucl Med Mol Imaging.* 2002;29:821-830.

224. Gutfilen B, Souza SA, Valentini G. Copper-64: a real theranostic agent. *Drug design, development and therapy.* 2018;12:3235-3245.

225. Ponnala S, Amor-Coarasa A, Kelly J, et al. A Next Generation Theranostic PSMA Ligand for 64Cu and67Cu-Based Prostate Cancer Imaging and Therapy. *Journal of Nuclear Medicine.* 2019;60:1005-1005.

226. Anderson CJ, Wadas TJ, Wong EH, Weisman GR. Cross-bridged macrocyclic chelators for stable complexation of copper radionuclides for PET imaging. *Q J Nucl Med Mol Imaging.* 2008;52:185-192.

227. Vallabhajosula S. *Molecular imaging: radiopharmaceuticals for PET and SPECT*: Springer Science & Business Media; 2009.

228. Blower PJ, Lewis JS, Zweit J. Copper radionuclides and radiopharmaceuticals in nuclear medicine. *Nucl Med Biol.* 1996;23:957-980.

229. Boswell CA, Sun X, Niu W, et al. Comparative in vivo stability of copper-64-labeled cross-bridged and conventional tetraazamacrocyclic complexes. *J Med Chem.* 2004;47:1465-1474.

230. Wadas TJ, Wong EH, Weisman GR, Anderson CJ. Copper chelation chemistry and its role in copper radiopharmaceuticals. *Curr Pharm Des.* 2007;13:3-16.

231. Cutler P, Schwarz S, Eichling J. Whole-body dosimetry from PET images of mono-colonal antibodies labeled with CU-64. *Journal of Nuclear Medicine.* 1994;35:

232. Cutler PD, Schwarz SW, Anderson CJ, et al. Dosimetry of copper-64-labeled monoclonal antibody 1A3 as determined by PET imaging of the torso. *Journal of Nuclear Medicine.* 1995;36:2363-2371.

233. McCarthy DW, Shefer RE, Klinkowstein RE, et al. Efficient production of high specific activity 64Cu using a biomedical cyclotron. *Nucl Med Biol.* 1997;24:35-43.

234. Makkonen-Craig S. 64Cu production, ligands and biomedical applications. 2006;

235. Junde H, Xialong H, Tuli J. Nucl Data Sheets. 106, 159 (2005). *Data extracted from the ENSDF database,(April 1, 2005) National Nuclear Data Base. Brookhaven National Laboratory, USA.* 2005;

236. Anderson CJ. Metabolism of radiometal-labeled proteins and peptides: what are the real radiopharmaceuticals in vivo? *Cancer Biother Radiopharm.* 2001;16:451-455.

237. Mushtaq A, Karim HMA, Khan MA. Production of no-carrier-added64Cu and67Cu in a reactor. *Journal of Radioanalytical and Nuclear Chemistry.* 1990;141:261-269.

238. Skakun Y, Qaim S. Excitation function of the 64Ni(α,p) 67Cu reaction for production of 67Cu. *Applied Radiation and Isotopes - APPL RADIAT ISOTOPES.* 2004;60:33-39.

239. New FDA approvals. *Retrieved September 2019 from http://www.fda.gov/Drugs/InformationOnDrugs/ApprovedDrugs/ucm352317.htm.*

240. Munro TR. The relative radiosensitivity of the nucleus and cytoplasm of Chinese hamster fibroblasts. *Radiat Res.* 1970;42:451-470.

241. Nikula TK, McDevitt MR, Finn RD, et al. Alpha-emitting bismuth cyclohexylbenzyl DTPA constructs of recombinant humanized anti-CD33 antibodies: pharmacokinetics, bioactivity, toxicity and chemistry. *J Nucl Med.* 1999;40:166-176.

242. Barendsen GW. MODIFICATION OF RADIATION DAMAGE BY FRACTIONATION OF THE DOSE, ANOXIA, AND CHEMICAL PROTECTORS IN RELATION TO LET. *Ann N Y Acad Sci.* 1964;114:96-114.

243. Formenti SC, Demaria S. Combining radiotherapy and cancer immunotherapy: a paradigm shift. *J Natl Cancer Inst.* 2013;105:256-265.

244. Kroemer G, Galluzzi L, Kepp O, Zitvogel L. Immunogenic cell death in cancer therapy. *Annu Rev Immunol.* 2013;31:51-72.

245. Subcommittee NI. Compelling Research Opportunities Using Isotopes. *One of Two NSAC Charges on the National Isotopes Production and Application Program.* 2009;42.

246. Qaim SM, Tarkanyi F. *Nuclear data for the production of therapeutic radionuclides*. International Atomic Energy Agency (IAEA): IAEA; 2011.

247. Boll RA, Malkemus D, Mirzadeh S. Production of actinium-225 for alpha particle mediated radioimmunotherapy. *Applied Radiation and Isotopes.* 2005;62:667-679.

248. McDevitt MR, Sgouros G, Finn RD, et al. Radioimmunotherapy with alpha-emitting nuclides. *European Journal of Nuclear Medicine.* 1998;25:1341-1351.

249. Koch L, Apostolidis C, Molinet R. Production of Bi-213 and Ac-225, α-Immuno' 97 Symposium Proceedings. Joint Research Centre. *Institute for Transuranium Elements (ITU). Karlsruhe, Germany.* 1998;20-25.

250. McDevitt MR, Ma D, Lai LT, et al. Tumor therapy with targeted atomic nanogenerators. *Science.* 2001;294:1537-1540.

251. Deal KA, Davis IA, Mirzadeh S, Kennel SJ, Brechbiel MW. Improved in Vivo Stability of Actinium-225 Macrocyclic Complexes. *Journal of Medicinal Chemistry.* 1999;42:2988-2992.

252. Kennel SJ, Chappell LL, Dadachova K, et al. Evaluation of 225Ac for Vascular Targeted Radioimmunotherapy of Lung Tumors. *Cancer Biotherapy and Radiopharmaceuticals.* 2000;15:235-244.

253. Atallah E, Berger M, Jurcic J, et al. A Phase 2 Study of Actinium-225 (225Ac)-lintuzumab in Older Patients with Untreated Acute Myeloid Leukemia (AML). *Journal of Medical Imaging and Radiation Sciences.* 2019;50:S37.

254. Yadav M, Bal C, Ballal S, Sahoo R. *Clinical Experience on 225Ac-PSMA-617 Targeted Alpha Therapy in Metastatic Castration Resistant Prostate Cancer Patients: Safety and Efficacy Results*2019.

255. McDevitt MR, Finn RD, Sgouros G, Ma D, Scheinberg DA. An 225Ac/213Bi generator system for therapeutic clinical applications: construction and operation. *Applied Radiation and Isotopes.* 1999;50:895-904.

256. Pippin C, Gansow O, Brechbiel M, et al. Chemists View of Imaging Centers. 1995;

257. Krolicki L, Bruchertseifer F, Kunikowska J, et al. Safety and efficacy of targeted alpha therapy with (213)Bi-DOTA-substance P in recurrent glioblastoma. *Eur J Nucl Med Mol Imaging.* 2019;46:614-622.

258. Chan HS, de Blois E, Konijnenberg MW, et al. Optimizing labelling conditions of (213)Bi-DOTATATE for preclinical applications of peptide receptor targeted alpha therapy. *EJNMMI Radiopharm Chem.* 2017;1:9.

259. Friesen C, Glatting G, Koop B, et al. Breaking chemoresistance and radioresistance with [213Bi]anti-CD45 antibodies in leukemia cells. *Cancer Res.* 2007;67:1950-1958.

260. Norenberg JP, Krenning BJ, Konings IR, et al. 213Bi-[DOTA0, Tyr3]octreotide peptide receptor radionuclide therapy of pancreatic tumors in a preclinical animal model. *Clin Cancer Res.* 2006;12:897-903.

261. Kim YS, Brechbiel MW. An overview of targeted alpha therapy. *Tumour Biol.* 2012;33:573-590.

262. Leichner P. Radiation dosimetry of monoclonal antibodies: practical considerations. *Nuclear Medicine. St. Louis: Mosby.* 1996;558-562.

263. Bartoś B, Lyczko K, Kasperek A, Krajewski S, Bilewicz A. Search of ligands suitable for 212Pb/212Bi in vivo generators. *Journal of Radioanalytical and Nuclear Chemistry.* 2013;295:205-209.

264. Chappell LL, Dadachova E, Milenic DE, Garmestani K, Wu C, Brechbiel MW. Synthesis, characterization, and evaluation of a novel bifunctional chelating agent for the lead isotopes 203Pb and 212Pb. *Nucl Med Biol.* 2000;27:93-100.

265. Meredith RF, Torgue J, Azure MT, et al. Pharmacokinetics and Imaging of 212Pb-TCMC-Trastuzumab After Intraperitoneal Administration in Ovarian Cancer Patients. *Cancer Biotherapy and Radiopharmaceuticals.* 2013;29:12-17.

266. Meredith RF, Torgue JJ, Rozgaja TA, et al. Safety and outcome measures of first-in-human intraperitoneal α radioimmunotherapy with 212Pb-TCMC-trastuzumab. *American journal of clinical oncology.* 2018;41:716.

267. Meredith R, Torgue J, Shen S, et al. Dose escalation and dosimetry of first-in-human α radioimmunotherapy with 212Pb-TCMC-trastuzumab. *Journal of Nuclear Medicine.* 2014;55:1636-1642.

268. Hillier SM, Maresca KP, Femia FJ, et al. Preclinical evaluation of novel glutamate-urea-lysine analogues that target prostate-specific membrane antigen as molecular imaging pharmaceuticals for prostate cancer. *Cancer Res.* 2009;69:6932-6940.

269. Chen Y, Foss CA, Byun Y, et al. Radiohalogenated prostate-specific membrane antigen (PSMA)-based ureas as imaging agents for prostate cancer. *J Med Chem.* 2008;51:7933-7943.

270. Afshar-Oromieh A, Zechmann CM, Malcher A, et al. Comparison of PET imaging with a (68)Ga-labelled PSMA ligand and (18)F-choline-based PET/CT for the diagnosis of recurrent prostate cancer. *Eur J Nucl Med Mol Imaging.* 2014;41:11-20.

271. Price EW, Orvig C. Matching chelators to radiometals for radiopharmaceuticals. *Chem Soc Rev.* 2014;43:260-290.

272. Benesova M, Bauder-Wust U, Schafer M, et al. Linker Modification Strategies To Control the Prostate-Specific Membrane Antigen (PSMA)-Targeting and Pharmacokinetic Properties of DOTA-Conjugated PSMA Inhibitors. *J Med Chem.* 2016;59:1761-1775.

273. Grubmuller B, Baum RP, Capasso E, et al. (64)Cu-PSMA-617 PET/CT Imaging of Prostate Adenocarcinoma: First In-Human Studies. *Cancer Biother Radiopharm.* 2016;

274. Cui C, Hanyu M, Hatori A, et al. Synthesis and evaluation of [(64)Cu]PSMA-617 targeted for prostate-specific membrane antigen in prostate cancer. *Am J Nucl Med Mol Imaging.* 2017;7:40-52.

275. Kumar K, Magerstädt M, Gansow OA. Lead (II) and bismuth (III) complexes of the polyazacycloalkane-N-acetic acids nota, dota, and teta. *Journal of the Chemical Society, Chemical Communications.* 1989;145-146.

276. Maumela H, Hancock RD, Carlton L, Reibenspies JH, Wainwright KP. The amide oxygen as a donor group. Metal ion complexing properties of tetra-N-acetamide substituted cyclen: a crystallographic, NMR, molecular mechanics, and thermodynamic study. *Journal of the American Chemical Society.* 1995;117:6698-6707.

277. Kularatne SA, Zhou Z, Yang J, Post CB, Low PS. Design, synthesis, and preclinical evaluation of prostate-specific membrane antigen targeted (99m)Tc-radioimaging agents. *Mol Pharm.* 2009;6:790-800.

278. Liu T, Toriyabe Y, Kazak M, Berkman CE. Pseudoirreversible inhibition of prostate-specific membrane antigen by phosphoramidate peptidomimetics. *Biochemistry.* 2008;47:12658-12660.

279. Studer M, and Kadan, T.A. One-step synthesis of mono-N-substituted azamacrocycles with a carboxylic group in the side-chain and their complexes with Cu2+ and Ni2+. *Helvetica.* 1986; 69:2081–2086.

280. Boswell CA, Regino CA, Baidoo KE, et al. Synthesis of a cross-bridged cyclam derivative for peptide conjugation and 64Cu radiolabeling. *Bioconjug Chem.* 2008;19:1476-1484.

281. Kielar F, Cassino C, Leone L, Tei L, Botta M. Macrocyclic trinuclear gadolinium(iii) complexes: the influence of the linker flexibility on the relaxometric properties. *New Journal of Chemistry.* 2018;42:7984-7992.

282. Schäfer M, Bauder-Wüst U, Leotta K, et al. A dimerized urea-based inhibitor of the prostate-specific membrane antigen for 68Ga-PET imaging of prostate cancer. *EJNMMI research.* 2012;2:23-23.

283. Kratochwil C, Schmidt K, Afshar-Oromieh A, et al. Targeted alpha therapy of mCRPC: Dosimetry estimate of (213)Bismuth-PSMA-617. *Eur J Nucl Med Mol Imaging.* 2018;45:31-37.

284. Zhang AX, Murelli RP, Barinka C, et al. A remote arene-binding site on prostate specific membrane antigen revealed by antibody-recruiting small molecules. *J Am Chem Soc.* 2010;132:12711-12716.

285. Hillier S, Rubino K, Maresca K, et al. [131I] MIP-1466, a small molecule prostate-specific membrane antigen (PSMA) inhibitor for targeted radiotherapy of prostate cancer (PCa). *J Nucl Med.* 2012;53:170-170.

286. Benesova M, Umbricht CA, Schibli R, Muller C. Albumin-Binding PSMA Ligands: Optimization of the Tissue Distribution Profile. *Mol Pharm.* 2018;15:934-946.

287. Wong EH, Weisman GR, Hill DC, et al. Synthesis and Characterization of Cross-Bridged Cyclams and Pendant-Armed Derivatives and Structural Studies of Their Copper(II) Complexes. *Journal of the American Chemical Society.* 2000;122:10561-10572.

288. Riesen A, Zehnder M, Kaden TA. Structure of the barium salt of a Cu2+ complex with a tetraaza macrocyclic tetraacetate. *Acta Crystallographica Section C.* 1988;44:1740-1742.

289. Riesen A, Zehnder M, Kaden TA. Metal complexes of macrocyclic ligands. Part XXIII. Synthesis, properties, and structures of mononuclear complexes with 12- and 14-membered tetraazamacrocycle-N,N′,N″,N‴-tetraacetic Acids. *Helvetica Chimica Acta.* 1986;69:2067-2073.

290. Smith-Jones PM, Fridrich R, Kaden TA, et al. Antibody labeling with copper-67 using the bifunctional macrocycle 4-[(1,4,8,11-tetraazacyclotetradec-1-yl)methyl]benzoic acid. *Bioconjug Chem.* 1991;2:415-421.

291. Eder M, Neels O, Muller M, et al. Novel Preclinical and Radiopharmaceutical Aspects of [68Ga]Ga-PSMA-HBED-CC: A New PET Tracer for Imaging of Prostate Cancer. *Pharmaceuticals (Basel).* 2014;7:779-796.

292. Bacich DJ, Pinto JT, Tong WP, Heston WD. Cloning, expression, genomic localization, and enzymatic activities of the mouse homolog of prostate-specific membrane antigen/NAALADase/folate hydrolase. *Mamm Genome.* 2001;12:117-123.

293. Kratochwil C, Giesel FL, Leotta K, et al. PMPA for nephroprotection in PSMA-targeted radionuclide therapy of prostate cancer. *J Nucl Med.* 2015;56:293-298.

294. Rousseau E, Lau J, Kuo HT, et al. Monosodium Glutamate Reduces (68)Ga-PSMA-11 Uptake in Salivary Glands and Kidneys in a Preclinical Prostate Cancer Model. *J Nucl Med.* 2018;59:1865-1868.

295. Cai H, Wu J-s, Muzik O, Hsieh J-T, Lee RJ, Peng F. Reduced 64Cu uptake and tumor growth inhibition by knockdown of human copper transporter 1 in xenograft mouse model of prostate cancer. *J Nucl Med.* 2014;55:622-628.

296. Peng F, Lu X, Janisse J, Muzik O, Shields AF. PET of human prostate cancer xenografts in mice with increased uptake of 64CuCl2. *J Nucl Med.* 2006;47:1649-1652.

297. Piccardo A, Paparo F, Puntoni M, et al. (64)CuCl2 PET/CT in Prostate Cancer Relapse. *J Nucl Med.* 2018;59:444-451.

298. Nedrow JR, Latoche JD, Day KE, et al. Targeting PSMA with a Cu-64 Labeled Phosphoramidate Inhibitor for PET/CT Imaging of Variant PSMA-Expressing Xenografts in Mouse Models of Prostate Cancer. *Mol Imaging Biol.* 2016;18:402-410.

299. Sevcenco S, Klingler HC, Eredics K, et al. Application of Cu-64 NODAGA-PSMA PET in Prostate Cancer. *Adv Ther.* 2018;35:779-784.

300. Heroux KJ, Woodin KS, Tranchemontagne DJ, et al. The long and short of it: the influence of N-carboxyethyl versusN-carboxymethyl pendant arms on in vitro and in vivo behavior of copper complexes of cross-bridged tetraamine macrocycles. *Dalton Trans.* 2007;2150-2162.

301. Sun X, Wuest M, Weisman GR, et al. Radiolabeling and in vivo behavior of copper-64-labeled cross-bridged cyclam ligands. *J Med Chem.* 2002;45:469-477.

302. Cole WC, DeNardo SJ, Meares CF, et al. Serum stability of 67Cu chelates: comparison with 111In and 57Co. *Int J Rad Appl Instrum B.* 1986;13:363-368.

303. Meares CF, Moi MK, Diril H, et al. Macrocyclic chelates of radiometals for diagnosis and therapy. *Br J Cancer Suppl.* 1990;10:21-26.

304. Mirick GR, O'Donnell RT, DeNardo SJ, Shen S, Meares CF, DeNardo GL. Transfer of copper from a chelated 67Cu-antibody conjugate to ceruloplasmin in lymphoma patients. *Nucl Med Biol.* 1999;26:841-845.

305. Bass LA, Wang M, Welch MJ, Anderson CJ. In vivo transchelation of copper-64 from TETA-octreotide to superoxide dismutase in rat liver. *Bioconjug Chem.* 2000;11:527-532.

306. Notni J, Wester H-J. Re-thinking the role of radiometal isotopes: Towards a future concept for theranostic radiopharmaceuticals. *Journal of Labelled Compounds and Radiopharmaceuticals.* 2018;61:141-153.

307. Yoshii Y, Yoshimoto M, Matsumoto H, et al. Integrated treatment using intraperitoneal radioimmunotherapy and positron emission tomography-guided surgery with (64)Cu-labeled cetuximab to treat early- and late-phase peritoneal dissemination in human gastrointestinal cancer xenografts. *Oncotarget.* 2018;9:28935-28950.

308. Su H-c, Zhu Y, Hu S-l, et al. The Value of 99mTc-PSMA SPECT/CT-Guided Surgery for Identifying and Locating Lymph Node Metastasis in Prostate Cancer Patients. *Annals of Surgical Oncology.* 2019;26:653-659.

309. Barinka C, Byun Y, Dusich CL, et al. Interactions between human glutamate carboxypeptidase II and urea-based inhibitors: structural characterization. *J Med Chem.* 2008;51:7737-7743.

310. Kopka K, Benesova M, Barinka C, Haberkorn U, Babich J. Glu-Ureido-Based Inhibitors of Prostate-Specific Membrane Antigen: Lessons Learned During the Development of a

329. Guiyang Hao TM, Gedaa Hassan, William Silvers, Orhan Oz, and Xiankai Sun. Reintroduction of copper-67 to radioimmunotherapy and evaluation of its imaging potential. *J Nucl Med* 2017;58:940:

330. Antunes P, Ginj M, Walter MA, Chen J, Reubi JC, Maecke HR. Influence of different spacers on the biological profile of a DOTA-somatostatin analogue. *Bioconjug Chem.* 2007;18:84-92.

331. Kane RS. Thermodynamics of multivalent interactions: influence of the linker. *Langmuir.* 2010;26:8636-8640.

7. ACKNOWLEDGEMENTS

In the first place I would like to deeply thank my supervisor **Professor Walter Mier** for entrusting me on his favorite field of research. I know that he cares a lot about PSMA and does not let everybody meddle with his baby. He supported me in many ways, evaluated data, never ceased to motivate me and encouraged me never to give up.

Second, I would like to express my gratitude to **Professor Uwe Haberkorn**, Medical Director of the Department of Nuclear Medicine at the University of Heidelberg and Head of the Clinical Cooperation Unit Nuclear Medicine at the DKFZ for the opportunity to work in this group and also for the translation of ^{64}Cu-CA003/ $^{203/212}$Pb -CA012, ^{68}Ga-CA028 and ^{68}Ga-CA030 into the clinic.

Furthermore, I wish to thank **Dr. Clemens Kratochwil** for his brilliant ideas for the lead project, for his commitment to analyze the data and to translate the best compound into clinic as well as for sharing and discussing the patients results with us.

My thanks also go to my good old colleagues for the great time we spent together: **Sebastian Brings**, **Thomas Lindner**, **Philipp Uhl**, **Max Sauter**, **Artjom Wischnjow**, **Anastasia Loktev, Martin Müller, Mazen Jamous, Cornelius Domhan, Matthias Schwarz** and to our new generation of highly motivated PhD students, always being friendly with me: **Andreas Krause**, **Florian Umstetter**, **Sabrina Wohfahrt**, **Philip Storck** as well as the bachelor students who I had the pleasure to work with: Julia Noll, Fabian Ebner, **Julia Rühle**, **Eric Mühlberg** (the computer expert) and **Leah Zerlin** (english expertise).

Barbro Beijer, the world's best chemist was always with me on the journey of this project. I would like to thank her for the chemical synthesis and her great engagement with my project.

I would like to thank **Dr. Susanne Krämer** for her expert assistance in radiolabeling of the compounds for clinical use. I could always ask her everything and she was constantly there for me.

Another big thank you goes to **Dr. Christian Kleist** for his incredible help at the lab. He always was friendly and extremely committed with my project.

Karin Leotta not only was helping me with the PET/ SPECT imaging studies but was anytime available to teach and to discuss the results.

I am much obliged to **Sabrina Wohlfahrt** and **Andreas Krause** for their help at any time. They are the best picture advisor I ever had.

My project was made possible because of the excellent cooperation with DKFZ.

Professor Klaus Kopka Head of department /Radiopharmaceutical Chemistry at DKFZ was always very friendly and offered interest and help in many ways. I wish to thank him for the great opportunity to work in his group. Also, my gratitude to **Dr. Oliver Niels** for his support in any circumstances.

Two outstanding colleagues were **Ulrike Bauder-Wüst** and **Martin Schäfer**. **Uli** is extremely competent and supported me during all the years I worked with her. We had a wonderful time together not only with the cell culture experiments. During the time we worked together we went on imagined journeys and I have a very high regard for her. **Martin** showed me everything about peptide synthesis and all the related issues. He is a fabulous teacher and a great person. Thank you for the collaboration!

I wish to express my special thanks to **Professor Matthias Eder**, for his help and encouragement for my project. He always was available for discussions and gave me a lot of input for my work.

Dr. Martina Benesová, thank you for the excellent work and the support of my achievement, for all the hints, suggestions, great proof-reading of all the papers and this thesis and for your support in moments when it was needed.

Allan Bastos, **Tobias Timmermann**, (grande amigo), **Stephan Hinkes** and **Alexander Jacob**, thank you very much for performing the NMR with me.

Ann-Christin Eder, **Mareike Roscher** and **Anja Wacker** initially my fellow students at DKFZ and now great friends.

I extend my gratitude to my friendly colleagues: **Markus Reber**, **Yvonne Remde**, **Jana Schmidt, Jonas Scheuber, Sarah Schwarz, Heike Marx, Sandra Casula and Rebekka Hoffner**. We spent an amazing time together.

Lukas Beumer is a promising young scientist who supported me with IT and technical issues – thank you very much.

My research stay at Memorial Sloan Kettering in New York City was unforgettable. I would like to thank **Jason Lewis** for welcoming me in his group. Furthermore, a big

thank you goes to **Jan-Philip Meyer** to make this stay possible and the excellent supervision.

I apologise for writing in Portuguese: Aqui venho expressar a minha gratidão a **minha família brasileira** pelo apoio sempre. A minha gratidão e meu carinho para com minha família alemã (**Fabian Haunss, Ingrid Haunss, Verena Chase e Sebastian Haunss**). Amo vocês!

Extendo ainda o meu carinho os meus agradecimentos a tantos grandes amigos que tornam minha vida especial (**Tiago Chaves, Fernanda Gonzales e família, Ramiro e Luccia e família, Sílvia Bittencourt e família Mariazinha Paula Quitana, Adriana Jou, Sílvia Barbosa e Natalia**)

O meu muito obrigado para esta grandes mulheres por estarem sempre presente na minha vida **Senhora Usadel e Henrike Schön**.

A special thanks goes to my **Thesis Advisory Committee**: **Prof. Gert Fricker**, **Prof. Owen**, **Dr. Eva Frei.** They all not only gave me feedback, support and evaluation during my project but also manifold advice and contribution – for sure the best advisory committee I could imagine.

A special thanks goes **to Eva Frei.** She is a very special person to me, like my scientific mother and great friend. My doctorate would not have been possible without her.

8. LIST OF PUBLICATIONS

Dos Santos JC, Schäfer M., Bauder-Wüst U., Wencke Lehnert W., Leotta K., Morgenstern A., Kopka K., Haberkorn Uwe, Mier W., Kratochwil C. Development and dosimetry of ^{203}Pb/^{212}Pb-labelled PSMA ligands: bringing “the lead” into PSMA-targeted alpha therapy? European Journal of Nuclear Medicine and Molecular Imaging, 2018.

Dos Santos JC, Barbro B., Bauder-Wüst U., Schäfer M., Leotta K., Eder M, Benešová M., Kleist C., Giesel F., Kratochwil C., Kopka K., Haberkorn W., Walter Mier. "Development of Novel PSMA Ligands for Imaging and Therapy with Copper Isotopes". The Journal of Nuclear Medicine, 2019.

Dos Santos JC, Schäfer M., Bauder-Wüst U., Beijer B., Eder M., Benešová M., Kleist C., Leotta L., Meyer JP., Dilling T., Lewis J., Kratochwil C., Kopka K., Haberkorn U., Mier M., Refined Chelator Spacer Moieties Ameliorate the Pharmacokinetics of PSMA-617. The Journal of Nuclear Medicine, 2019. **(Manuscript)**

9. PATENT APPLICATION

Haberkorn U., Dos Santos JC, Mier W., Kratochwil C., Bauder-Wüst U., Schäfer M., Klaus Kopka. “Labeled inhibitors of prostate specific membrane antigen (PSMA), their use as imaging agents and pharmaceutical agents for the treatment of PSMA-expressing cancers”. European patent application number/Patent number: 18197704.2/1109, date: 21. November 2018. Applicant/Proprietor: Universitätsklinikum Heidelberg.

10. CONFERENCES

POSTER

Enhancing the drug load of PSMA-specific targeted drugs. XV KICancer Retreat, Karolinska Institutet, Djurönäset, September 2016.

Novel ^{64}Cu-ligands for diagnosis and therapy of prostate cancer- 21th Annual DKFZ PhD Retreat, July 2016.

Enhancing the drug load of PSMA-specific targeted drugs-Helmholtz International Graduate School for Cancer Research DKFZ, 2017

TALK

Enhancing the drug load of PSMA-specific targeted drugs. NextGen@Helmholtz 2016 Conference, Braunschweig, **2016**.

Fundamentals of nuclear medicine and progress in cancer research. Instituto Federal Ceará-Campus Quixadá, February **2017**.

PSMA as specific target. Bad Herrenalber Barrierer and Transporter, Bad Herrenalb **2018**.

Enhancing the drug load of PSMA-specific targeted drugs. 2nd International Conference on Oncology and Radiology, September, Rome, Italy **2018**.

Development and dosimetry of ^{203}Pb/^{212}Pb-labelled PSMA ligands: bringing “the lead” into PSMA-targeted alpha therapy. AGRR 2019. 27. Jahrestagung der Arbeitsgemeinschaft Radiochemie/Radiopharmazie. 12-14.September 2019. Pamhagen, Österreich.

Current value of PSMA-Targeting Ligands in Diagnostic and Therapeutic Nuclear Medicine. Annual Congress of the European Association of Nuclear Medicine. 12-16 October **2019**. Barcelona, Spain.

11. SUPPLEMENTARY INFORMATION

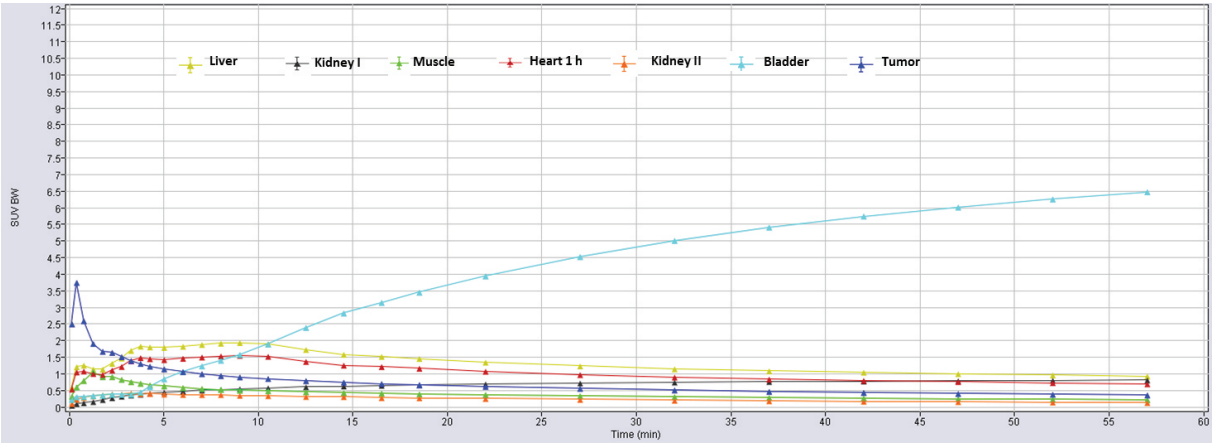

Figure S1. Time-activity curves for tumor and relevant organs up to 1 h post injection of 0.2 nmol (100 µL -as injected volume of 0.9% saline) of ^{68}Ga-CA028 in a BALB/c *nu/nu* mouse bearing a C4-2 tumor xenograft. Data are mean standardized uptake value based on body weight-values (SUV_{BW}).

TABLE S1

Mean standardized uptake values (mSUV) derived from the time-activity curves from small-animal PET of ^{68}Ga-PSMA-CA028 in a BALB/c nu/nu mouse bearing a C4-2 tumor xenograft.

mSUV	Heart	Liver	Kidneys	Bladder	Tumor	Muscle
T_1 = 1 h	0.36	0.22	0.39	6.50	0.81	0.13
T_2 = 2 h	0.13	0.09	0.29	2.5	0.78	0.05